Robust Control

of

Multi-Stage Web Systems

Xijiang Dou

A thesis presented to Lakehead University

In partial fulfillment of the requirement for the degree of

Master of Science in Control Engineering

Thunder Bay, Ontario, Canada, 2007

Your file Votre référence
ISBN: 978-0-494-31825-6
Our file Notre référence
ISBN: 978-0-494-31825-6

Abstract

Web handling systems are widely used in industries such as pulp and paper, printing press, and steel milling. Tension variations in web materials are very common in operation and tension control is critical to the quality control of the related manufacturing facilities. Speed variations or changes will cause fluctuations in web tension; as a result, speed control is another important issue in web handling systems to prevent machinery performance degradation and to maintain desired productivity.

The web system control problem is investigated comprehensively in this research on both intermediate zone and unwinding-winding process. First, active tension control strategies are studied. Two MIMO control strategies, H_∞ and LQR, are developed and compared with a PI–based decentralized control strategy in terms of control performance and robustness properties of the resultant closed-loop system. A gain scheduling scheme is suggested to deal with the time varying parameters in a winding process. Robust stability analysis is proposed to quantitatively determine the necessity of gain scheduling. Comprehensive test results show that the proposed H_∞ control is superior to other strategies in the investigated web system application.

The second contribution of this work is the development of an inactive tension control strategy to effectively eliminate the 'tension transfer' phenomenon among web spans in a multi-stage web handling system. This strategy is implemented by a looper-like actuator which is controlled by a PID controller. It is the first inactive looper tension control technique in literature for thin web system applications. The developed active and inactive web control strategies are verified by both simulation and experimental tests.

Acknowledgements

I wish to express my sincere appreciation to Dr. Wilson Wang. His guidance and support were essential to the completion of this thesis. I would like to thank my co-supervisor Dr. Sultan Siddiqui for his help and suggestions. I would also like to acknowledge Dr. Xiaoping Liu and Dr. Yu Shen for their efforts as examiners of this thesis. Special thanks go to Dr. Xiaoping Liu. His inspiring teaching and helpful suggestions opened me the door to robust control theory. I would like to thank James Gray for his work in fabricating the inactive tension actuator.

I thank all my friends at Lakehead University for their friendship, moral support and technical discussion during the past two years.

Most importantly, however, I want to thank my wife, Sally Cao, for her patience, understanding and encouragement on my graduate studies.

Contents

List of Figures

List of Tables

Chapter 1 Introduction

1.1 Background Knowledge

The term *web* refers to any material in a continuous flexible strip form which is either endless or very long compared to its width, and very wide compared to its thickness. In some situations, however, it is named other terms, e.g. film, belt, foil, strip, thread fabric, etc. Many types of industrial products are manufactured or processed in the form of a web, e.g. paper in paper mills or printing presses, plastic film, textiles, tape, thin metals, etc. [1].

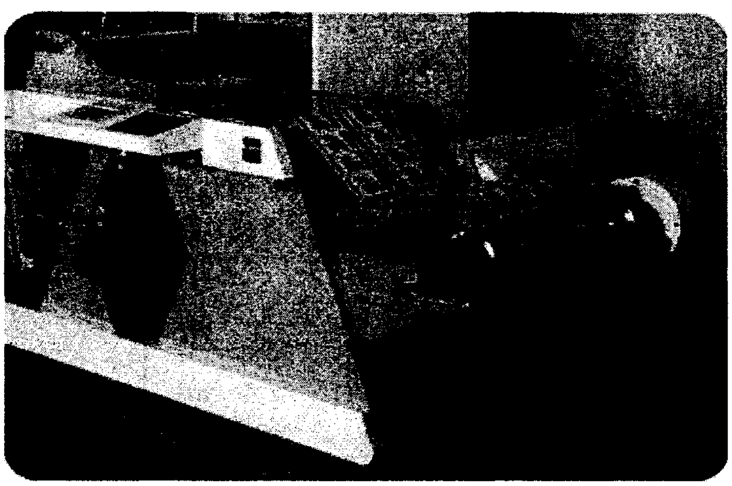

Figure 1.1 A web handling system

A multi-stage (or multi-span) web handling system consists of several types of mechanical components (e.g. rollers, rolls, measuring devices, driving motors, etc.) and web spans. The dynamic characteristics of the mechanical components and the physical properties of the web material affect the steady-state and dynamic behaviour of the web in the longitudinal direction. Tension variations in the web are common in operation and critical to the quality of products. For example, the main concern in printing quality control is called *doubling*, which is a register error among different printing stages. Doubling occurs whenever the non-crossover error of images among different printing stages exceeds a threshold (e.g. 0.076 mm for general pictures). It is mainly caused by rotation non-synchronization errors among printing stages, resulting from vibration and machinery imperfections such as misalignment, wear, and component damage [2]. A rotation non-synchronization error, in fact, results in web tension fluctuations between two rotating driven rollers and can be measured and quantified by a tension measuring device. It implies that non-synchronization errors can be compensated by accurate web tension control. However, variations in the physical characteristics of the web material, the high sensitivity of the web material characteristics to environmental changes (e.g. temperature and moisture), and the interactions among adjacent spans, make accurate tension control in a moving web more difficult. This tends to be more apparent when thinner webs and higher speeds are involved in a web system.

The web material may have to pass through several consecutive processing sections (e.g. cleaning, coating and drying, etc.) in the manufacture of a product. Different web tension levels and accuracies can even be required by different processing sections. According to the section locations, a web system can be roughly partitioned into three zones: Unwinding zone, intermediate zone and winding (or rewinding) zone, as illustrated in **Figure 1.2**. The web is transported through driven nip rolls in the intermediate zone. Simpler machines, e.g. winding machines, may only have one integrated unwinding/winding zone, which corresponds to a winding process. Web system control is correspondingly divided into two main categories in literature: winding process control and intermediate web span control.

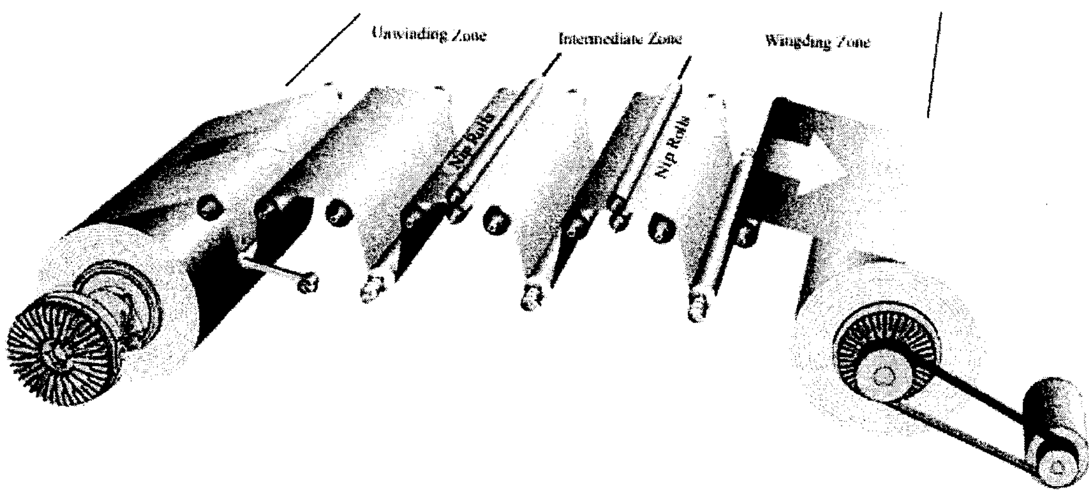

Figure 1.2 Main functional zones in a multi-stage web system

The speed of a moving web contributes significantly to the productivity of a manufacturing process. Speed variations or changes cause fluctuations in web tension, so speed control is the other important aspect of web system control. Usually in a multi-span web system, one of the driving motors is controlled to provide a master speed, which is referred by other motors and the overall process line.

The objectives of a multi-span web system control can then be summarized as following:

- To stabilize the overall web handling system;
- To maintain the precise longitudinal tension level required in each processing section;
- To provide an adjustable master speed to the overall web handling system.

1.2 Multi-Stage Web system Control

1.2.1 Decentralized Control and Centralized Control

According to the centralization characteristic of controllers, there are two categories of web tension/speed control systems: centralized MIMO control and decentralized (or distributed) SISO control. When taking two intermediate web spans for illustration, these two control systems are shown in **Figure 1.3** and **Figure 1.4**, respectively. The first driven roller is controlled to provide a master speed to the overall web system.

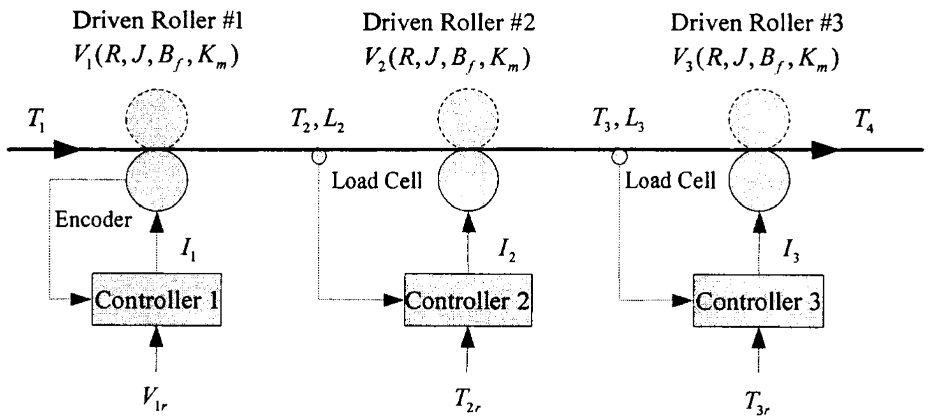

Figure 1.3 A decentralized control system.

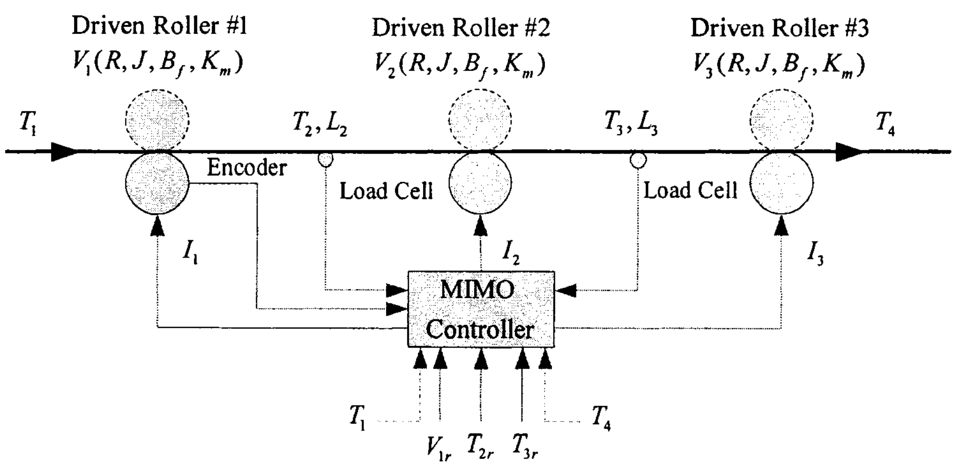

Figure 1.4 A centralized MIMO control system.

Decentralized control strategy has been explored for decades and is currently prevalent in industrial applications due to its advantage in implementation. A decentralized (distributed) web control system usually integrates multiple Proportional-Integral-Differential (PID) controllers to control multiple driven rollers. In order to properly determine the gains of PID controllers, decoupling techniques are usually applied to decompose a web span model into a tension control loop and a speed control loop. However, there is a high interaction between the web tension and web speed. As a result, the transient performance when either of tension and speed fluctuates is always a concern for such an SISO-control-based design. To achieve better transient and steady-state performance, Shin [3] suggested a distributed tension control by using auxiliary dynamic models, in which speed difference between adjacent driven rollers are adopted as new state variables. Song etc. [4] proposed a feedforward control with a tension observer to compensate tension fluctuations due to speed changes. A neural-network-based control and a fuzzy logic control are also developed in papers [5] and [6], respectively, to improve the robustness of web tension to speed variations.

Disturbances on tension control due to speed variations are difficult to be compensated completely by a feedforward loop, or model modification, etc. especially when the plant model has uncertain parameters and measurement noises. In addition, there exist other perturbation sources on web tension, among which the most important are tension variations from adjacent web spans. Moreover, on the other hand, the speed robustness to tension variation is also desired in web system control, but the compensation is even more difficult to be achieved. Therefore, if control requirements become higher, more efficient and sophisticated strategies are needed. Compared to the distributed SISO control system, a centralized MIMO control is able to compensate the interactions effectively by including both tension and speed as model states. As shown in **Figure 1.4**, the upstream tension variation T_1 and the downstream tension variation T_4 are considered as system disturbances, which can be integrated into the synthesis of an MIMO controller (e.g. H_∞ controller) to achieve desired disturbance rejection.

However, a centralized MIMO control system becomes unsuitable when the plant is a large-scale system with many web spans, because the order of the controller could be very high [7]. A semi-centralized MIMO system can then be configured by distributing a number of MIMO controllers. An example is illustrated in **Figure 1.5**.

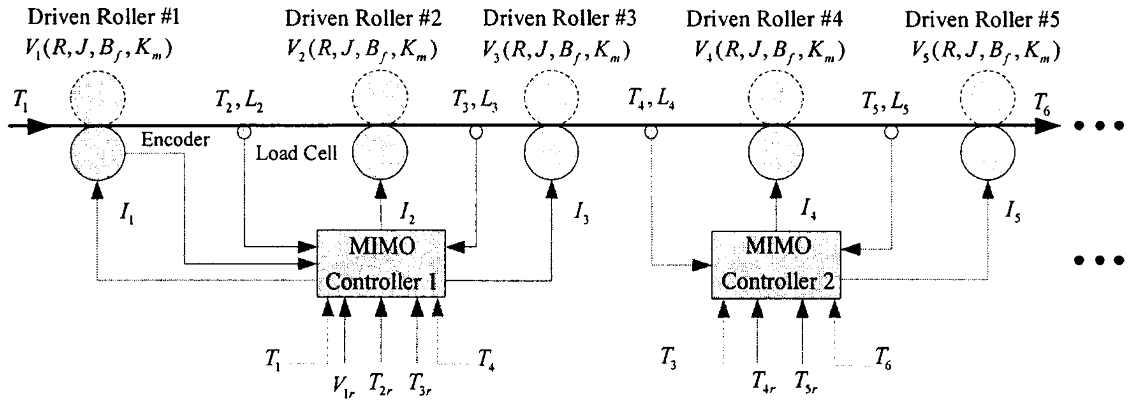

Figure 1.5 A semi-centralized MIMO control system.

1.2.2 Intermediate Zone Control and Winding Process Control

Usually intermediate web spans are involved in the major manufacturing or process procedure. The control of intermediate web spans is characterized by the complexity in dealing with two types of interactions. One of them is the interaction between tension variation and speed variation, and the other one is the interactions with the upstream web span and the downstream span. These interactions in a multi-stage web system cause a particular phenomenon, which is informally named as *tension transfer*. It means a tension fluctuation in a single web span will affect the tension in the following spans.

The challenge in winding process control is to deal with time varying radius and inertia of winding/unwinding rolls. In literature, Koc etc. [8] suggested a gain scheduling based on dc gain analysis of tension output. Park etc. [9] proposed to switch gains within a predefined lookup table upon different operating conditions. In this work, a comprehensive investigation is conducted on the necessity of gain scheduling based on robust stability analysis. In addition, a gain scheduling technique is implemented and verified by simulation and experimental tests.

1.2.3 Active Tension Control and Inactive Tension Control

Active control and inactive control are categorized according to the actuating mode of web tension control. All the configurations illustrated in **Figure 1.3** to **Figure 1.5** fall into active tension control. In active tension control, both desired tension and line speed are achieved by actively controlling driving motors. Most techniques in literature focus on active tension control strategy, since AC/DC motor drive units, which are popular nowadays, have greatly facilitated real-world implementations. Another advantage of active control is its quick response to commands and to disturbances.

However, *tension transfer* can not be eliminated by an active control strategy. Inactive control, which uses some particular structure as a tension control actuator, can prevent tension variations from being propagated to the following web spans. A typical strategy using an active dancer roll is shown in **Figure 1.6**. Tension is adjusted by the translational motion of the dancer roll. An alternative actuator is a looper-like structure, which is discussed in details in **Chapter 4**. Looper structure is usually adopted in steel strip mills as a tension measurement and mass flow control device. This work will investigate its first application as an inactive actuator in the tension control of thin web handling systems.

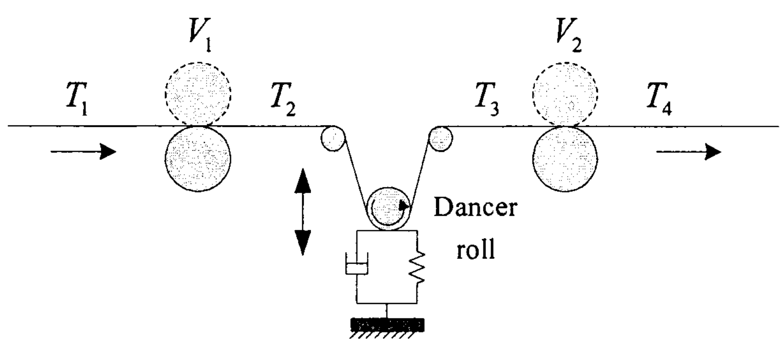

Figure 1.6 Inactive tension control using a dancer roll.

1.3 Robust Control of Web Systems

Tension control and speed control are two integral components of web system control. In addition to achieving good control performance, another objective in web system control is to acquire an analyzable robustness to disturbance and model uncertainty. Disturbance arises from several sources in a multi-stage web system. For example, disturbance on web tension could be an upstream tension fluctuation, or a web speed variation. In some industries, e.g. a printing press, different web materials may go through the same processing system, which means that the operating condition changes. When such perturbations exist, to what extent a control strategy remains effective and efficient is a concern in real-world applications.

H_2 and H_∞ syntheses are two classical robust control techniques, and have been explored in industrial control applications. In web system application, Choi etc. [10] proposed a robust approach for motor drive control in milling mills; Baumgart etc. [11] developed a robust strategy based on decoupled tension/speed loops of the nonlinear web system model. In [8] and [12], an H_∞ and a 2-DOF H_∞ controller are proposed to regulate a web transportation system; the above papers, however, do not provide systematic and quantitative analysis on robustness properties of the closed-loop system.

To ensure that a model-based controller works well in real-world applications, it is necessary to analyze the closed-loop robustness properties with model perturbations, such as disturbance, noise, unstructured and structured uncertainties. In general, the sources of parameterized plant perturbations include component tolerance, component drift or aging, external influence and model parameter uncertainty [13]. In web system applications, Laroche etc. [14] conducted robustness analysis based on an H_∞ control design, in which only μ-analysis was explored. The paper also lacks a systematic discussion on robust stability and performance.

1.4 Research Outline

Both intermediate zone control and winding process control, both active control and inactive control are investigated in this work. H_∞, LQR and PI control strategies are developed for active intermediate zone and winding process control, while a PID controller is designed for the proposed inactive tension control by using a looper-like actuator. The research outline is shown in the following chart.

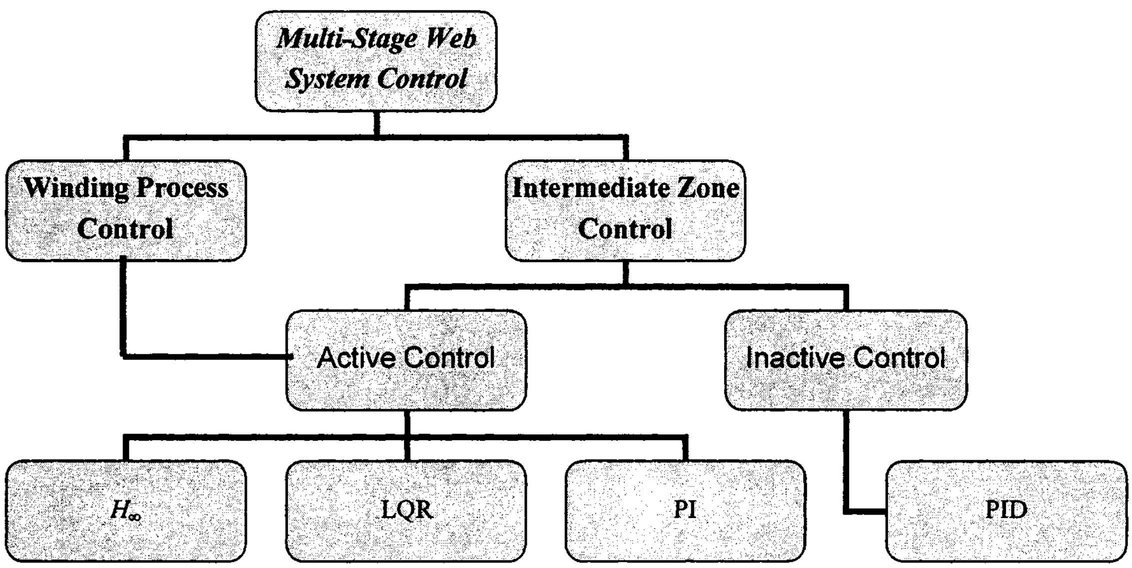

1.5 The Organization of This Thesis

In **Chapter 2** and **Chapter 3**, active control strategies for intermediate web span control and winding process control are developed, respectively.

The first objective in these two chapters is to develop a robust H_∞ control strategy to attenuate web tension fluctuations; and the second objective is to systematically investigate robustness properties of the closed-loop system. Considering the characteristics of web systems, real parametric uncertainty is considered as a model perturbation, and the main sources of disturbance are tension fluctuations from adjacent spans and roller velocity variations. Robustness properties are analyzed by using singular value (H_∞ norm) test and structured singular value (μ) test. The viability of the developed H_∞ controller is verified by both simulation and experimental tests. Control performance and robustness property are compared among the proposed H_∞ control, an LQR and a PI-based decentralized control.

In **Chapter 3**, winding process control, time varying parameters are considered as significantly changeable parametric uncertainties, such that the impact can be quantitatively investigated by robustness analysis. A gain scheduling technique is suggested to improve the system stability and control performance within the overall process.

An inactive tension control is studied in **Chapter 4**. A mathematical model of the proposed looper-like actuator is discussed. Simulation and experimental results are presented to demonstrate the viability of the control strategy.

Chapter 2 **Intermediate Zone Control**

2.1 System Modeling

2.1.1 Nominal Plant Modeling

Figure 2.1 shows a single intermediate web span, the most fundamental primitive element in web processing systems.

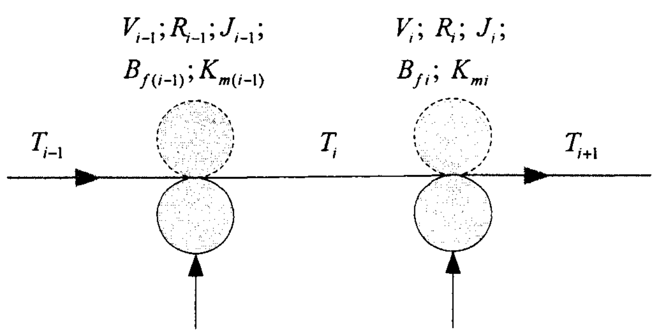

Figure 2.1 A single web span.

The following assumptions are made in the derivation of a mathematical model for this *i*th span:

1. The length of contact region between the web material and a roller is negligible compared to the length of the web span;
2. The thickness of the web is very small compared with the radius of rollers over which the web is wrapped;
3. There is no slippage between the web material and the rollers;
4. There is no mass transfer between the web material and the environment;
5. The strain in the web is small (much less than unity);
6. The strain is uniform within the web span;
7. The web cross-section in the unstretched state does not vary along the web;

8. The density and the elastic modulus of the web in the unstretched state are constant over the cross-section;
9. The web is perfectly elastic;
10. The web material is isotropic, so that machine direction (MD) stress prevails, i.e. $\sigma_x \neq 0,\ \sigma_y = \sigma_z = 0$;
11. The web properties do not change with temperature or humidity.

The dynamics of load cell and idle rollers are also neglected. Applying the mass conservation principle, Newton's second law, and Hooke's law, with the above assumptions, a linearized dynamic model of the *i*th web span can be derived as (see [3] for detailed procedure)

$$\dot{T}_i = -\frac{v_{i0}}{L_i}T_i - \frac{aE}{L_i}V_{i-1} + \frac{aE}{L_i}V_i + \frac{v_{(i-1)0}}{L_i}T_{i-1}, \tag{2.1}$$

$$\dot{V}_i = -\frac{R_i^2}{J_i}T_i - \frac{B_{fi}}{J_i}V_i + \frac{R_i^2}{J_i}T_{i+1} + \frac{R_i}{J_i}K_{mi}I_i. \tag{2.2}$$

where the related notations are:

T_i:	Change to the tension of the *i*th web span (*N*);
V_i:	Change to the tangential velocity at the periphery of the *i*th driven roller (*m/s*);
U_i:	Change to current input of the *i*th driving motor (*A*);
v_{i0}:	Steady-state operating tangential velocity of the *i*th driven roller (*m/s*);
L_i:	Length of the *i*th web span between two driven rollers (*m*);
a:	Cross-sectional area of the web material (m^2);
E:	Young's modulus of the web material (*GPa*);
B_{fi}:	Viscous friction Coefficient of the *i*th roller bearing (*N·m·s/rad*);
K_{mi}:	Toque constant of the *i*th driving motor (*N·m/A*);
R_i:	Radius of the *i*th driven roller (*m*);
J_i:	Moment of inertia of the *i*th driven roller ($kg \cdot m^2$).

The steady-state operating web tension is omitted from the linearized model. This approximation is made based on the little effect of the initial operating value would have on web tension dynamics. The detailed demonstration can be found in the reference.

Without loss of generality, the first processing span in **Figure 1.3** is taken out to illustrate control system design. The two driven rollers as well as their driving motors are assumed to be identical. A control system is designed to provide a master speed control for the driven roller #1 and to attenuate tension variations T_2. The upstream tension fluctuation T_1 and the downstream tension fluctuation T_3 are regarded as disturbances on the 2nd web span. They will be considered in the synthesis of an MIMO H_∞ controller such that the closed-loop system acquires desired rejection capability to these two disturbances.

The state-space representation (SSR) of the nominal plant is

$$\begin{cases} \dot{x}_p = A_n x_p + B_{n1} d + B_{n2} u \\ y = C_n x_p \end{cases}, \tag{2.3}$$

where the subscript p represents plant, and n stands for nominal. The state-space vectors and matrices are

$$x_p = [x_1 \quad x_2 \quad x_3]^T = [T_2 \quad V_1 \quad V_2]^T;$$

$$u = [u_1 \quad u_2]^T = [I_1 \quad I_2]^T;$$

$$y = [y_1 \quad y_2]^T = [T_2 \quad V_1]^T;$$

$$d = [d_1 \quad d_2]^T = [T_1 \quad T_3]^T.$$

$$A_n = \begin{bmatrix} -\frac{v_{20}}{L_2} & -\frac{aE}{L_2} & \frac{aE}{L_2} \\ \frac{R^2}{J} & -\frac{B_f}{J} & 0 \\ -\frac{R^2}{J} & 0 & -\frac{B_f}{J} \end{bmatrix}; \; B_{n1} = \begin{bmatrix} \frac{v_{10}}{L_2} & 0 \\ -\frac{R^2}{J} & 0 \\ 0 & \frac{R^2}{J} \end{bmatrix}; \; B_{n2} = \begin{bmatrix} 0 & 0 \\ \frac{RK_m}{J} & 0 \\ 0 & \frac{RK_m}{J} \end{bmatrix}; \; C_n = \begin{bmatrix} 1 & 0 & 0 \\ 0 & 1 & 0 \end{bmatrix}.$$

Model-based MIMO control design and robustness analysis will be demonstrated in the following sections based on the above single intermediate web span model which is described by the state-space representation (2.3).

2.1.2 Plant Modeling with Uncertainty Description

Uncertainties in the system of interest arise from measurements (e.g. velocity and tension feedback signals), environment (e.g. temperature and moisture effects on web length and web elasticity), and operating conditions (e.g. web types and machinery condition variations). Considering the real experimental configuration in this work, the following parametric model uncertainties are considered:

- Young's modulus E: ±1% from the operating value;
- Operating velocity v_{i0}: ±10% from the operating value;
- Roller radius R: ±10% from the operating value;
- Roller inertia J: ±5% from the operating value (related to radius change).

A state-space representation method is adopted in this work to describe the aforementioned parametric uncertainties. Let P_i be a nominal parameter value and $\tilde{P}_i$ be the uncertain counterpart, the corresponding parametric uncertainty can be described by

$$\tilde{P}_i = P_i(1+\delta_i\Delta_i). \tag{2.4}$$

where δ_i defines the parameter varying bound, and $\Delta_i \in [-1,\ 1]$ is a perturbation variable which is used to describe any possible parameter variation, within the bound specified by δ_i. For example, roller radius varying ±10% from the operating value corresponds to $\delta_R = 0.1$. If the maximum and minimum values of P_i can be determined, then

$$P_i = \frac{P_{i\max} + P_{i\min}}{2}, \text{ and } \delta_i = \frac{P_{i\max} - P_{i\min}}{2P_i}.$$

The model parametric uncertainties of the web span are then defined as:

$$\tilde{E} = E(1+\delta_E\Delta_E), \qquad \tilde{v}_{10} = v_{10}(1+\delta_v\Delta_v), \qquad \tilde{v}_{20} = v_{20}(1+\delta_v\Delta_v),$$

$$\tilde{R} = R(1+\delta_R\Delta_R), \qquad \tilde{J} = J(1+\delta_J\Delta_J).$$

The differential equations for (2.3) can be rewritten separately as (2.5) to (2.7):

$$\dot{x}_1 = -\frac{v_{20}(1+\delta_v\Delta_v)}{L_2}x_1 - \frac{aE(1+\delta_E\Delta_E)}{L_2}x_2 + \frac{aE(1+\delta_E\Delta_E)}{L_2}x_3 + \frac{v_{10}(1+\delta_v\Delta_v)}{L_2}d_1, \tag{2.5}$$

$$\dot{x}_2 = \frac{R^2(1+\delta_R\Delta_R)^2}{J(1+\delta_J\Delta_J)}x_1 - \frac{B_f}{J(1+\delta_J\Delta_J)}x_2 - \frac{R^2(1+\delta_R\Delta_R)^2}{J(1+\delta_J\Delta_J)}d_1 + \frac{R(1+\delta_R\Delta_R)}{J(1+\delta_J\Delta_J)}K_m u_1, \tag{2.6}$$

$$\dot{x}_3 = -\frac{R^2(1+\delta_R\Delta_R)^2}{J(1+\delta_J\Delta_J)}x_1 - \frac{B_f}{J(1+\delta_J\Delta_J)}x_3 + \frac{R^2(1+\delta_R\Delta_R)^2}{J(1+\delta_J\Delta_J)}d_2 + \frac{R(1+\delta_R\Delta_R)}{J(1+\delta_J\Delta_J)}K_m u_2. \tag{2.7}$$

To facilitate robustness analysis, uncertain components are separated from the nominal part in the above equations. Take (2.5) as an example,

$$\begin{aligned}\dot{x}_1 &= \underbrace{-\frac{v_{20}(1+\delta_v\Delta_v)}{L_2}x_1}_{I_1}\underbrace{-\frac{aE(1+\delta_E\Delta_E)}{L_2}x_2}_{I_2} + \underbrace{\frac{aE(1+\delta_E\Delta_E)}{L_2}x_3}_{I_3} + \underbrace{\frac{v_{10}(1+\delta_v\Delta_v)}{L_2}d_1}_{I_4} \\ &= I_1 + I_2 + I_3 + I_4 \end{aligned}\tag{2.8}$$

Each of the items I_1, I_2, I_3 and I_4 can be decomposed into nominal part and uncertain part. The latter is characterized by the term Δ_i, for example,

$$I_1 = -\frac{v_{20}(1+\delta_v\Delta_v)}{L_2}x_1 = -\frac{v_{20}}{L_2}x_1 \underbrace{-\frac{v_{20}\delta_v}{L_2}x_1\Delta_v}_{u_\Delta^1} = -\frac{v_{20}}{L_2}x_1 + u_\Delta^1 \tag{2.9}$$

An uncertainty pair, u_Δ^1 and y_Δ^1, can then be derived as

$$u_\Delta^1 = -\frac{v_{20}\delta_v}{L_2}x_1\Delta_v = y_\Delta^1\Delta_v. \tag{2.10}$$

As a result, 14 uncertainty pairs can be generated by similar decompositions. Those can be denoted as an input vector y_Δ and an output vector u_Δ, and

$y_\Delta = \left[y_\Delta^1,\ y_\Delta^2,\ \ldots,\ y_\Delta^{14}\right]^T$;

$u_\Delta = \left[u_\Delta^1,\ u_\Delta^2,\ \ldots,\ u_\Delta^{14}\right]^T$.

The uncertain components of the plant model can be represented by these input-output ($y_\Delta^i - u_\Delta^i$) pairs. The transfer matrix from y_Δ to u_Δ is a real diagonal matrix Δ, which is H_∞-norm-bounded (i.e. $\|\Delta\|_\infty \leq 1$) due to its components $\Delta_i \in [-1,\ 1]$. The relation is represented by

$$u_\Delta = \Delta y_\Delta, \tag{2.11}$$

with $\Delta = diag\{\Delta_v, \Delta_E, \Delta_E, \Delta_v, \Delta_R, \Delta_R^2, \Delta_R, \Delta_R^2, \Delta_R, \Delta_J, \Delta_R, \Delta_R^2, \Delta_R, \Delta_J\}$.

Any uncertainty input y_Δ^i, $i = 1, 2\ldots, 14$, is a function of exogenous system inputs (d in this case), control signals (u) and/or plant states (x_p). **Figure 2.2** shows a block diagram describing the pair in (2.10). A model block diagram of the plant with all uncertain pairs can also be derived in a similar pattern.

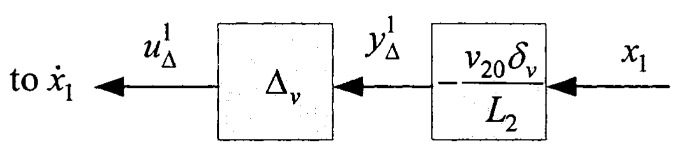

Figure 2.2 Block diagram of an uncertainty pair.

The state-space model in (2.3) can be reconstructed with above parametric uncertainty description considered. It yields

$$\begin{cases} \dot{x}_p = A_u x_p + B_{u0} u_\Delta + B_{u1} d + B_{u2} u \\ y_\Delta = C_{u0} x_p + D_{u00} u_\Delta + D_{u01} d + D_{u02} u, \\ y = C_{u1} x_p \end{cases} \tag{2.12}$$

where the subscript u denotes *uncertain* and the related matrices are

$A_u = A_n$;

$$B_{u0} = \begin{bmatrix} [1]_{1\times4} & [0]_{1\times10} & & \\ [0]_{1\times4} & [1]_{1\times6} & & [0]_{1\times4} \\ [0]_{1\times4} & [-1]_{1\times2} & [0]_{1\times4} & [1]_{1\times4} \end{bmatrix};$$

$B_{u1} = B_{n1}$, $B_{u2} = B_{n2}$;

$$C_{u0} = \begin{bmatrix} -\frac{v_{20}\delta_v}{L_2} & 0 & 0 & 0 & \frac{2R^2\delta_R}{J} & \frac{R^2\delta_R^2}{J} & & -\frac{R^2\delta_J}{J} & & \frac{R^2\delta_J}{J} \\ 0 & -\frac{aE}{L_2}\delta_E & 0 & 0 & 0 & 0 & 0_{3\times3} & \frac{B_f\delta_J}{J} & 0_{3\times3} & 0 \\ 0 & 0 & \frac{aE}{L_2}\delta_E & 0 & 0 & 0 & & 0 & & \frac{B_f\delta_J}{J} \end{bmatrix}^T;$$

$C_{u1} = C_n$;

$$D_{u00} = \begin{bmatrix} 0_{9\times14} & & & \\ 0_{1\times4} & [-\delta_J]_{1\times6} & & 0_{1\times4} \\ 0_{3\times14} & & & \\ 0_{1\times4} & [\delta_J]_{1\times2} & 0_{1\times4} & [-\delta_J]_{1\times4} \end{bmatrix}_{14\times14};$$

$$D_{u01} = \begin{bmatrix} 0_{2\times3} & \frac{v_{10}\delta_v}{L_2} & 0_{2\times2} & -\frac{2R^2\delta_R}{J} & -\frac{R^2\delta_R^2}{J} & 0 & \frac{R^2\delta_J}{J} & 0 & 0 & 0 & 0 \\ & 0 & & 0 & 0 & 0 & 0 & \frac{2R^2\delta_R}{J} & \frac{R^2\delta_R^2}{J} & 0 & -\frac{R^2\delta_J}{J} \end{bmatrix}^T;$$

$$D_{u02} = \begin{bmatrix} 0_{2\times8} & \frac{RK\delta_R}{J} & -\frac{RK}{J}\delta_J & 0 & 0 & 0 & 0 \\ & 0 & 0 & 0 & 0 & \frac{RK\delta_R}{J} & -\frac{RK}{J}\delta_J \end{bmatrix}^T$$

Based on the above uncertainty description, an upper LFT framework can be developed to represent the state-space model in (2.12), as shown in **Figure 2.3**. LFTs will be introduced in next section.

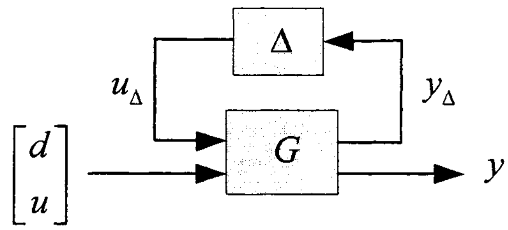

Figure 2.3 The standard upper LFT framework.

2.2 H_∞ Control Design

2.2.1 Linear Fractional Transformation (LFT)

Suppose that $G(s)$ is a complex matrix partitioned as

$$G = \begin{bmatrix} G_{11} & G_{12} \\ G_{21} & G_{22} \end{bmatrix} \in \mathbb{C}^{(p_1+p_2)\times(q_1+q_2)}. \tag{2.13}$$

Let $K \in \mathbb{C}^{q_2 \times p_2}$ and $\Delta \in \mathbb{C}^{q_1 \times p_1}$ be two complex matrices. Lower LFT and upper LFT with respect to K and Δ, respectively, are defined as the maps [15]

$$F_l(G,\,K):\ \mathbb{C}^{q_2\times p_2} \mapsto \mathbb{C}^{q_1\times p_1};\quad F_u(G,\,\Delta):\ \mathbb{C}^{q_1\times p_1} \mapsto \mathbb{C}^{p_2\times q_2};$$

The block diagrams of lower LFT and upper LFT are illustrated in **Figure 2.4** (a) and **Figure 2.4** (b), respectively.

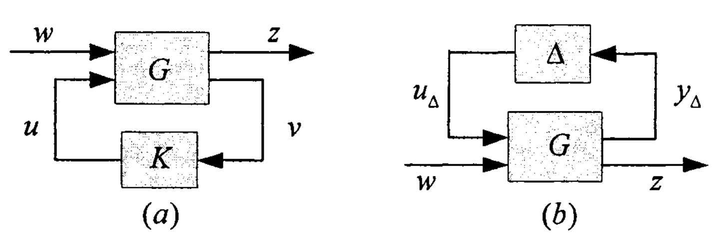

Figure 2.4 (a) Lower LFT, (b) upper LFT.

Lower LFT and upper LFT can be firstly realized by transfer matrix operations:

$$F_l(G,\,K) := T_{zw} = G_{11} + G_{12}K(I - G_{22}K)G_{21}, \tag{2.14}$$

$$F_u(G,\ \Delta) := T_{zw} = G_{22} + G_{21}\Delta(I - G_{11}\Delta)G_{12}. \tag{2.15}$$

where T_{zw} represents the resultant transfer matrix from w to z, i.e. a map from the exogenous input to the exogenous output.

To facilitate the calculation of LFTs, a state-space realization is more desired for the above transfer matrix representations. First, denote the state-space realization of a nominal plant model $G(s)$ [refers to SSR (2.3)] and the controller $K(s)$ as

$$G = \begin{bmatrix} G_{11} & G_{12} \\ G_{21} & G_{22} \end{bmatrix} = \left[\begin{array}{c|cc} A & B_1 & B_2 \\ \hline C_1 & D_{11} & D_{12} \\ C_2 & D_{21} & D_{22} \end{array}\right],$$

$$K = \left[\begin{array}{c|c} A_k & B_k \\ \hline C_k & D_k \end{array}\right].$$

1) Let $\Phi_l = (I - D_{22}D_k)^{-1}$ and $\Phi_r = (I - D_kD_{22})^{-1}$. A state-space realization of lower LFT $F_l(G,\ K)$ can be derived based on (2.14) as

$$F_l(G,\ K) = \left[\begin{array}{cc|c} A + B_2\Phi_rD_kC_2 & B_2\Phi_rC_k & B_1 + B_2\Phi_rD_kD_{21} \\ B_k\Phi_lC_2 & A_k + B_k\Phi_lD_{22}C_k & B_k\Phi_lD_{21} \\ \hline C_1 + D_{12}\Phi_rD_kC_2 & D_{12}\Phi_rC_k & D_{11} + D_{12}\Phi_rD_kD_{21} \end{array}\right] = \left[\begin{array}{c|c} A_{Fl} & B_{Fl} \\ \hline C_{Fl} & D_{Fl} \end{array}\right]. \tag{2.16}$$

2) A state-space realization of upper LFT $F_u(G,\ \Delta)$ can be derived by a transformation of the above lower LFT state-space representation. The following transfer representation holds for upper LFT shown in **Figure 2.4 (b)**:

$$\begin{bmatrix} y_\Delta \\ z \end{bmatrix} = \begin{bmatrix} G_{11} & G_{12} \\ G_{21} & G_{22} \end{bmatrix}\begin{bmatrix} u_\Delta \\ w \end{bmatrix} = \left[\begin{array}{c|cc} A & B_1 & B_2 \\ \hline C_1 & D_{11} & D_{12} \\ C_2 & D_{21} & D_{22} \end{array}\right]\begin{bmatrix} u_\Delta \\ w \end{bmatrix}.$$

The above expression can be transformed into its counterpart for lower LFT while keeping the transfer relation from (u_Δ, w) to (y_Δ, z). That is

$$\begin{bmatrix} z \\ y_\Delta \end{bmatrix} = \begin{bmatrix} G_{22} & G_{21} \\ G_{12} & G_{11} \end{bmatrix} \begin{bmatrix} w \\ u_\Delta \end{bmatrix} = \left[\begin{array}{c|cc} A & B_2 & B_1 \\ \hline C_2 & D_{22} & D_{21} \\ C_1 & D_{12} & D_{11} \end{array}\right] \begin{bmatrix} w \\ u_\Delta \end{bmatrix}.$$

The transformation can be illustrated by **Figure 2.5**.

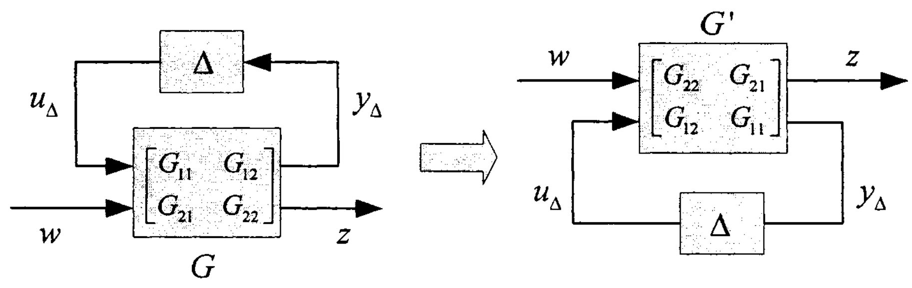

Figure 2.5 Transformation from upper LFT to lower LFT.

The derivation of $F_u(G, \Delta)$ is equivalently changed to that of $F_l(G', \Delta)$. Let $\Phi = (I - \Delta D_{11})^{-1}$ and consider that Δ is real diagonal matrix. A state-space realization of upper LFT is then derived based on the state-space representation in (2.16):

$$F_u(G, \Delta) = \left[\begin{array}{c|c} A + B_1\Phi\Delta C_1 & B_2 + B_1\Phi\Delta D_{12} \\ \hline C_2 + D_{21}\Phi\Delta C_1 & D_{22} + D_{21}\Phi\Delta D_{12} \end{array}\right] = \left[\begin{array}{c|c} A_{Fu} & B_{Fu} \\ \hline C_{Fu} & D_{Fu} \end{array}\right]. \tag{2.17}$$

The state-space realization of LFTs makes robustness analysis executable in Matlab.

2.2.2 H_∞ Control synthesis

2.2.2.1 H_∞ Norm and H_∞ Control

H_∞ synthesis is an optimization algorithm which aims to design a nominally stabilizing H_∞ controller to stabilize a plant and to gain the closed-loop system desired robustness to model perturbations. Consider a nominal system represented by a lower LFT framework in **Figure 2.6**.

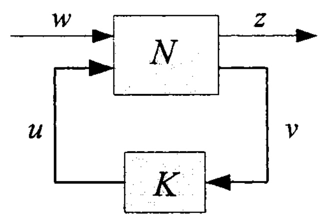

Figure 2.6 LFT framework of nominal closed-loop system.

The closed-loop transfer matrix can be denoted as $T_{zw} = F_l(N, K)$.. The H_∞ norm of the complex transfer matrix T_{zw} is defined as

$$\|T_{zw}(s)\|_\infty = \sup_{\omega \in \Re} \{\bar{\sigma}(T_{zw}(j\omega))\}. \tag{2.18}$$

where $\bar{\sigma}$ denotes the maximum singular value for a specific frequency ω, and $\Re$ is the collection of real numbers.

Two types of H_∞ Control are defined in literature:

Optimal H_∞ Control: Find all admissible controllers K(s) such that $\| T_{zw}(s) \|_\infty$ is minimized, i.e.

$$K(s) = \arg \min_{K(s) \in \mathcal{K}(s)} \|T_{zw}\|_\infty, \tag{2.19}$$

where $\mathcal{K}(s)$ is the set of all stabilizing controllers. It should be noted that the optimal H_∞ controllers are generally not unique for MIMO systems. Furthermore, finding an optimal controller is often both numerically and theoretically complicated. In practice, it is usually much cheaper to obtain controllers that are very close in the norm sense to the optimal ones, which will be called suboptimal controllers. A suboptimal controller may also have other nice properties (e.g. lower bandwidth) over the optimal ones.

Suboptimal H_∞ Control: Given γ >0, find all admissible controllers K(s), if there are any, such that $\| T_{zw}(s) \|_\infty < \gamma$ [16].

2.2.2.2 Weighting Functions and LFT Representation of Closed-Loop System

If the exogenous output vector z is weighted by a weighting function matrix $W(s)$, the objective of H_∞ synthesis becomes to minimize the H_∞ norm of a weighted transfer matrix $W \bullet T_{zw}$. Weighting functions, i.e. the elements in $W(s)$, are selected to shape the magnitude and frequency responses of the exogenous system output z. They are important in the control synthesis, and to a great extent, affect the control performance and robustness property of the closed-loop system.

For the considered plant (a single web span), the closed-loop system with selected weighting functions $W_e(s)$ and $W_u(s)$ is illustrated in **Figure 2.7**, where set-point vector $r = [T_{2r} \quad V_{1r}]^T$;

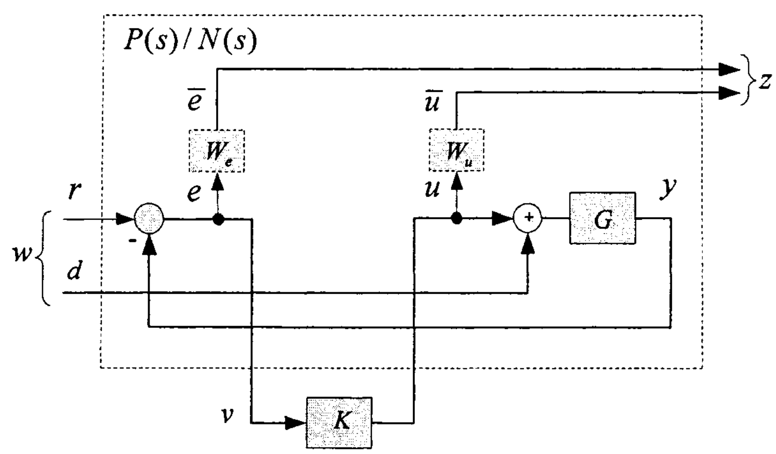

Figure 2.7 The closed-loop system with weighting functions.

$P(s)$ is an augmented interconnection system with an exogenous input vector w and an exogenous output vector z. $K(s)$ is the controller to be designed. $N(s)$ is the nominal part of the augmented interconnection system $P(s)$, when the plant $G(s)$ refers to the nominal model in (2.3) instead of (2.12). $N(s)$ is adopted in designing the nominally stabilizing H_∞ controller.

A standard LFT framework can equivalently represent the practical system in **Figure 2.7** in a compact way, which is shown in **Figure 2.8**. A mathematical representation of the closed-loop system, in a form of either transfer matrix or SSR, can be readily derived by LFT operations introduced in **2.2.1**. Robustness analysis of the closed-loop system will also be carried out based on the derived representations.

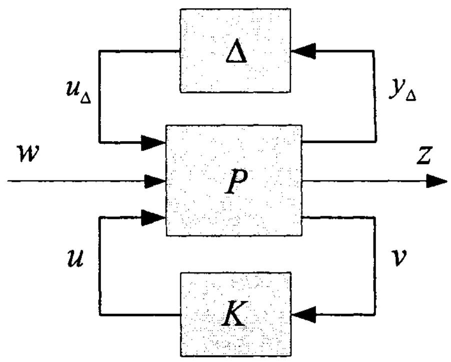

Figure 2.8 The standard LFT framework of closed-loop system.

According to definitions (2.18) and (2.19), the channel (component) selection of vector z and w is also critical to the closed-loop system properties. For the plant in this study, z and w are defined as $[\bar{e} \quad \bar{u}]^T$ and $[d \quad r]^T$, respectively, to achieve low tracking error, high disturbance rejection, and minimum control effort.

Weighting function $W_e(s)$, which is generally called performance weighting function, aims to limit the magnitude of the output sensitivity function $S_o = (I + GK)^{-1}$ within a particular frequency range. For the closed system in **Figure 2.7**, we have the following transfer equations:

$$\bar{e} = W_e S_o r - W_e S_o G d\,; \tag{2.20}$$

$$\bar{u} = W_u K S_o r - W_u S_i d\,. \tag{2.21}$$

where the input sensitivity function $S_i = (I + KG)^{-1}$.

$W_e S_o$ is the transfer function between the reference signal, r, and the weighted tracking error $\bar{e}$ (exogenous output). Equation (2.20) shows that the effects of reference signal r on the weighted tracking error can be made "small" by making the combined sensitivity function

W_eS_o small, in a sense of norm. Therefore, the H_∞ norm of W_eS_o becomes one of the objectives to be minimized by H_∞ synthesis. Its desired value is limited to be less than a particular value, usually unity, i.e. $\|W_e S_o\|_\infty < 1$ [17]. It also implies an equivalent objective $\|S_o\|_\infty < \|W_e^{-1}\|_\infty$. $W_e(s)$ is commonly selected with a high gain at low frequency to reject low frequency perturbations. The structure of $W_e(s)$ is selected in this work as

$$W_e = \frac{s + M\omega_b}{M(s + \varepsilon\omega_b)}, \tag{2.22}$$

where M is the peak magnitude of S_o, $\|S_o\|_\infty \le M$; ε is the allowed steady-state error; and ω_b is the required minimum frequency bandwidth.

The control signal weighting function $W_u(s)$ is selected to shape the frequency property of control signals. In this work, it is selected with the following structure

$$W_u(s) = \frac{s + \dfrac{\omega_u}{M_u}}{\varepsilon_u s + \omega_u}, \tag{2.23}$$

where M_u is the maximum gain of KS_o, i.e. $\|KS_o\|_\infty < \|W_u^{-1}\|_\infty$. ω_u is the bandwidth of the controller K; and ε_u is a real value to adjust the pole location of W_u [16].

Other weighting function structures are also discussed in literature. For example, paper [18] introduces different structures for $W_e(s)$ and $W_u(s)$, which are

$$W_e = \lambda \frac{s + \rho^\mu}{s + \tau}, \tag{2.24}$$

$$W_u(s) = \frac{m}{U_0}(1 + \frac{U_0}{2V_0}), \tag{2.25}$$

where $\mu \in \{0,1\}$, $1/\lambda = 1/W_e(\infty)$ represents the disturbance rejection ability of the system at high frequencies, and $\tau/\lambda\rho = 1/W_e(0)$ is the allowed steady-state error; U_0 is the maximal effort magnitude of an actuator and V_0 is its rate limit, corresponding to a step input of magnitude m. The structure here for $W_e(s)$ is similar with the previous one. A rational structure of $W_e(s)$ is also investigated in literature as

$$W_e = \frac{\lambda}{s + \omega_e}, \tag{2.26}$$

where ω_e is a small value related to steady-state error, and λ is used to adjust the gain.

The selection of weighting function structures and their numerical realization are conducted based on the considerations as follows:

- To achieve desired control performance;
- To optimize the control effort and avoid actuator saturation;
- To bring the best robustness property to the closed-loop system;
- To obtain the best balance among different robustness properties of the closed-loop system.

During the selection process, simulation test and robustness analysis are used as the verification tools. For example, a comparison was made between two types of combinations.

Table 2.1 Robustness property comparison between two combinations of weighting functions.

	$W_e(s)$ and $W_u(s)$	$\|M_{11}\|_\infty$	$\|M_{22}\|_\infty$
Combination 1	(2.22) and (2.23)	2.5569	1.1158
Combination 2	(2.26) and (2.25)	2.6112	1.9801

Not only does combination 1 provide a better robustness property, but also it presents better control performance and more practical control efforts than combination 2. This can be illustrated by Figure 2.9 and Figure 2.10.

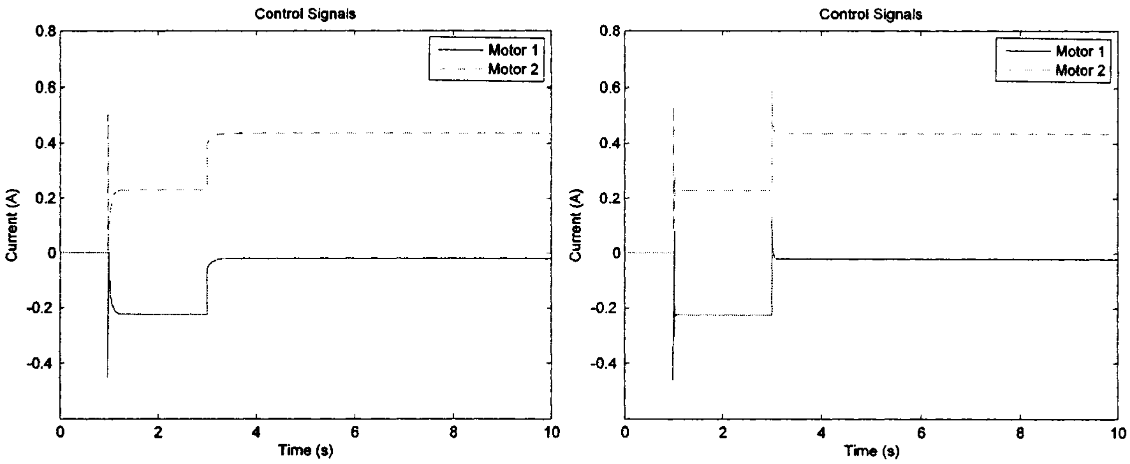

Figure 2.9 Control effort comparison. Combination 1 (left), Combination 2 (right).

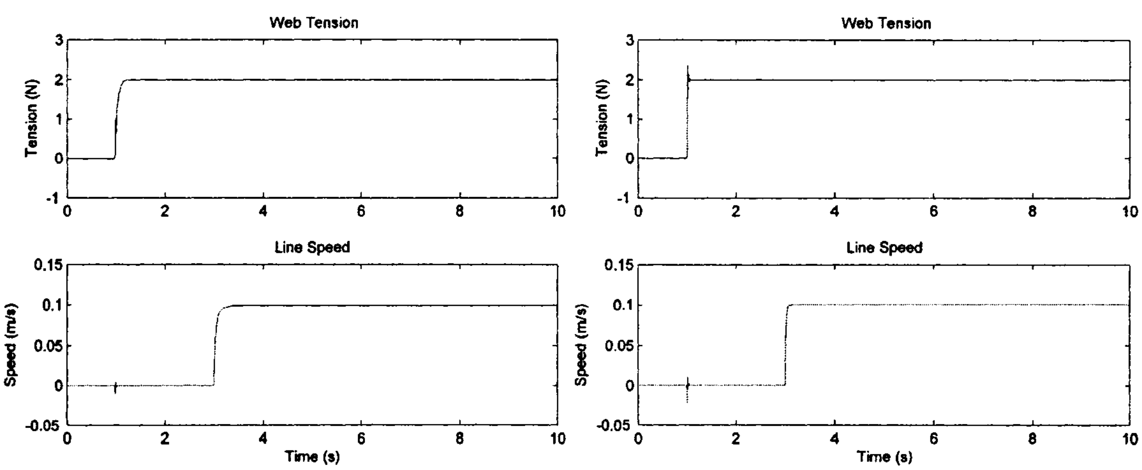

Figure 2.10 Control performance comparison. Combination 1 (left), Combination 2 (right).

In this work, $W_e(s)$ and $W_u(s)$ are numerically selected as (corresponding to combination 1)

$$W_e(s) = \begin{bmatrix} \dfrac{0.2s+8}{s+0.08} & 0 \\ 0 & \dfrac{0.2s+10}{s+0.01} \end{bmatrix}; \; W_u(s) = \begin{bmatrix} \dfrac{0.05s+0.1}{s+5} & 0 \\ 0 & \dfrac{0.05s+0.1}{s+5} \end{bmatrix}.$$

2.2.2.3 State-Space Realization of the Interconnection System

The augmented interconnection system $P(s)$, in a standard LFT framework as shown in **Figure 2.8**, should be constructed and realized into a state-space representation for a robust control design, based on a state-space solution of H_2 and H_∞ problems [19].

A state-space combination method is adopted in this work to generate the structure of $P(s)$, whose states are constituted by the states of W_u, W_e, and the plant G represented by (2.12). The map from exogenous inputs to outputs is

$$\begin{bmatrix} y_\Delta \\ z \\ v \end{bmatrix} = P(s) \begin{bmatrix} u_\Delta \\ w \\ u \end{bmatrix}, \tag{2.27}$$

where

$$P(s) = \begin{bmatrix} P_{00}(s) & P_{01}(s) & P_{02}(s) \\ P_{10}(s) & P_{11}(s) & P_{12}(s) \\ P_{20}(s) & P_{21}(s) & P_{22}(s) \end{bmatrix} = \left[\begin{array}{c|ccc} A & B_0 & B_1 & B_2 \\ \hline C_0 & D_{00} & D_{01} & D_{02} \\ C_1 & D_{10} & D_{11} & D_{12} \\ C_2 & D_{20} & D_{21} & D_{22} \end{array}\right]. \tag{2.28}$$

The state-space representation matrices in this work are

$$A = \begin{bmatrix} A_{wu} & 0 & 0 \\ 0 & A_{we} & -B_{we}C_{u1} \\ 0 & 0 & A_u \end{bmatrix}_{7\times 7};$$

$$B = \left[B_0 \mid B_1 \mid B_2\right] = \left[\begin{bmatrix} 0_{4\times 14} \\ B_{u0} \end{bmatrix} \,\middle|\, \begin{bmatrix} 0_{2\times 4} & \\ 0_{2\times 2} & B_{We} \\ B_{u1} & 0_{3\times 2} \end{bmatrix} \,\middle|\, \begin{bmatrix} B_{Wu} \\ 0_{2\times 2} \\ B_{u2} \end{bmatrix}\right];$$

$$C = \begin{bmatrix} C_0 \\ \hline C_1 \\ \hline C_2 \end{bmatrix} = \left[\begin{array}{c} \begin{bmatrix} 0_{14\times 4} & C_{u0} \end{bmatrix} \\ \hdashline \begin{bmatrix} 0 & C_{We} & -D_{We}C_{u1} \\ C_{Wu} & 0_{2\times 5} & \end{bmatrix} \\ \hdashline \begin{bmatrix} 0_{2\times 4} & -C_{u1} \end{bmatrix} \end{array}\right];$$

$$D=\left[\begin{array}{c|c|c} D_{00} & D_{01} & D_{02} \\ \hline D_{10} & D_{11} & D_{12} \\ \hline D_{20} & D_{21} & D_{22} \end{array}\right]=\left[\begin{array}{c|c|c} D_{u00} & \begin{bmatrix} D_{u01} & 0_{14\times 2} \end{bmatrix} & D_{u02} \\ \hline 0_{4\times 14} & \begin{matrix} 0_{2\times 2} & D_{We} \\ 0_{2\times 4} & \end{matrix} & \begin{bmatrix} 0_{2\times 2} \\ D_{Wu} \end{bmatrix} \\ \hline 0_{2\times 14} & \begin{bmatrix} 0 & 0 & 1 & 0 \\ 0 & 0 & 0 & 1 \end{bmatrix} & 0_{2\times 2} \end{array}\right].$$

Accordingly, the nominal augmented interconnection system $N(s)$ can be realized as (2.29) when the uncertain part is taken out of (2.27) and (2.28).

$$\begin{cases} \begin{bmatrix} z \\ v \end{bmatrix} = N(s)\begin{bmatrix} w \\ u \end{bmatrix} \\ N(s)=\begin{bmatrix} P_{11}(s) & P_{12}(s) \\ P_{21}(s) & P_{22}(s) \end{bmatrix}=\left[\begin{array}{c|cc} A & B_1 & B_2 \\ \hline C_1 & D_{11} & D_{12} \\ C_2 & D_{21} & D_{22} \end{array}\right]. \end{cases} \tag{2.29}$$

2.2.2.4 Assumptions on H_∞ Control Problem

The nominal interconnection system $N(s)$ in (2.29) should have $D_{11} = \mathbf{0}$ and $D_{22} = \mathbf{0}$ for a standard H_∞ problem, according to the paper [19]. With this condition, $N(s)$ becomes

$$N(s)=\left[\begin{array}{c|cc} A & B_1 & B_2 \\ \hline C_1 & 0 & D_{12} \\ C_2 & D_{21} & 0 \end{array}\right]. \tag{2.30}$$

Furthermore, four assumptions should be satisfied to make the H_∞ problem solvable:

a1. (A, B_1) and (A, B_2) are stabilizable;

a2. (C_1, A) and (C_2, A) are detectable;

a3. $D_{12}^T[C_1 \ \ D_{12}]=\begin{bmatrix} 0 & I \end{bmatrix}$;

a4. $\begin{bmatrix} B_1 \\ D_{21} \end{bmatrix} D_{21}^T = \begin{bmatrix} 0 \\ I \end{bmatrix}$.

Given the selected weighting function $W_e(s)$ in (2.22), the condition described by (2.30). assumption a3 and assumption a4 are not satisfied. To relax the conditions and assumptions, a general H_∞ problem was explored in [20], [21] and [16]. The nominal interconnection system $N(s)$ in a general H_∞ problem takes a form of

$$N(s)=\left[\begin{array}{c|cc} A & B_1 & B_2 \\ \hline C_1 & D_{11} & D_{12} \\ C_2 & D_{21} & D_{22} \end{array}\right]. \tag{2.31}$$

For the plant model considered in this work, D_{22}=0. A basic solution of a general H_∞ problem is given in the references upon D_{22}=0. If $D_{22}\neq 0$ in some cases, a scaling procedure can then be applied to the controller designed from the solution.

The following assumptions are made for a general problem:

A1. (A, B_2) is stabilizable and (C_2, A) is detectable;

A2. The rank of D_{12} is equal to the number of control signals (u). The rank of D_{21} is equal to the number of error signals (e);

A3. $D_{12}=\begin{bmatrix} 0 \\ I \end{bmatrix}$, $D_{21}=\begin{bmatrix} 0 & I \end{bmatrix}$;

A4. $\begin{bmatrix} A-j\omega I & B_2 \\ C_1 & D_{12} \end{bmatrix}$ has full column rank for all ω;

A5. $\begin{bmatrix} A-j\omega I & B_1 \\ C_2 & D_{21} \end{bmatrix}$ has full row rank for all ω.

The assumption A3 is not completely satisfied in this work, because

$$D_{12}=\begin{bmatrix} 0 & 0 \\ 0 & 0 \\ 0.05 & 0 \\ 0 & 0.05 \end{bmatrix};$$

$$D_{21}=\begin{bmatrix} 0 & 0 & 1 & 0 \\ 0 & 0 & 0 & 1 \end{bmatrix}.$$

A normalization of D_{12} (the assumption on D_{21} has been met in this work) can be conducted to have the assumption satisfied, but a corresponding interconnection system transformation will arise from the normalization. First of all, perform singular value decomposition on D_{12} to obtain the matrix factorization

$$\tilde{D}_{12} = U_N \begin{bmatrix} 0 \\ I \end{bmatrix} R_N ,$$

where U_N is square and unitary. Now scale related variables by $z = U_N \tilde{z}$, $u = R_N \tilde{u}$. The original nominal interconnection system $N(s)$ can be reformulated as

$$\begin{aligned} \tilde{N}(s) &= \begin{bmatrix} U_N^* & 0 \\ 0 & I \end{bmatrix} N(s) \begin{bmatrix} I & 0 \\ 0 & R_N^{-1} \end{bmatrix} \\ &= \left[\begin{array}{c|cc} A & B_1 & B_2 R_N^{-1} \\ \hline U_N^* C_1 & U_N^* D_{11} & U_N^* D_{12} R_N^{-1} \\ C_2 & D_{21} & 0 \end{array}\right]; \\ &=: \left[\begin{array}{c|cc} \tilde{A} & \tilde{B}_1 & \tilde{B}_2 \\ \hline \tilde{C}_1 & \tilde{D}_{11} & \tilde{D}_{12} \\ \tilde{C}_2 & \tilde{D}_{21} & 0 \end{array}\right] \end{aligned} \tag{2.32}$$

with $\tilde{D}_{12} = \begin{bmatrix} 0 \\ I \end{bmatrix}$ and $\tilde{D}_{21} = \begin{bmatrix} 0 & I \end{bmatrix}$. [16]

The transformation is illustrated by **Figure 2.11**.

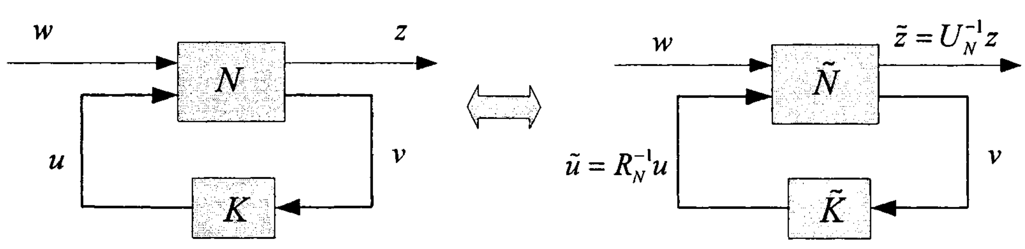

Figure 2.11 Reformulation of the nominal interconnection system.

Further more, it can be found that

$$\|T_{zw}\|_\infty = \|F_l(N,\ K)\|_\infty = \|U_N F_l(N,\ K)\|_\infty = \|F_l(\tilde{N},\ K)\|_\infty = \|T_{\tilde{z}w}\|_\infty , \tag{2.33}$$

since U_N is unitary. The scaling relation between controllers K and $\tilde{K}$ is

$$K(s) = R_N^{-1}\tilde{K}(s). \tag{2.34}$$

Based on the reformulated system $\tilde{N}(s)$, with all assumptions satisfied, suboptimal H_∞ controllers $\tilde{K}(s)$ can be derived upon the solutions of two Riccati equations and then $K(s)$ will be obtained by the scaling relation in (2.34). The detailed procedure can be found in the references and it has been programmed in a Matlab function 'hinfsyn', which aims to solve a general H_∞ problem. The set of all suboptimal H_∞ controllers is represented by $K(s) = F_l(M_\infty, Q)$, where Q is any stable proper transfer matrix such that $\|Q\|_\infty < \gamma$.

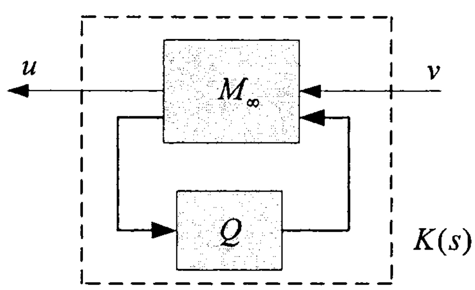

Figure 2.12 All suboptimal H_∞ controllers.

2.2.3 Nominal Plant Model Identification

Although some parameter values of the plant model can be measured (e.g. radii) or have been given by manufacturers (e.g. motor toque constant), there is no clue for the nominal values of some parameters (e.g. Young's modulus of the paper roll, E, and viscous friction coefficient of the overall transmission system, B_f). Such plant parameters were identified by recursive least squares (RLS). Winding process model is adopted for the identification purpose since it has fewer disturbances and fewer items to estimate. Data sets were collected from a closed-loop system controlled by a PI controller, which had been tuned for best performance. Reference signals were set to square waves. It should be noted that one of the advantages of using square wave references is that the radius of winding/unwinding rolls will not vary much and can be considered as constants.

Recursive least square algorithm is summarized as follows. Suppose there is a discrete time difference equation for system output y:

$$y(t) = a_1 y(t-1) + b_1 u_1(t) + b_2 u_2(t). \tag{2.35}$$

Define

$\theta^T = \begin{bmatrix} a_1 & b_0 & b_1 \end{bmatrix}$, and

$\varphi^T(t-1) = \begin{bmatrix} y(t-1) & u_1(t) & u_2(t) \end{bmatrix}$.

Then the current output can be represented as:

$$y(t) = \varphi^T(t-1)\theta.$$

The recursive estimation equations are

$$\hat{\theta}(t) = \hat{\theta}(t-1) + K(t)\left[y(t) - \varphi^T(t-1)\hat{\theta}(t-1)\right]; \tag{2.36}$$

$$P(t) = \left\{P(t-1) - P(t-1)\varphi(t-1)\left[\lambda + \varphi^T(t-1)P(t-1)\varphi(t-1)\right]^{-1}\varphi^T(t-1)P(t-1)\right\}/\lambda; \tag{2.37}$$

$$K(t) = P(t)\varphi(t-1) = P(t-1)\varphi(t-1)\left[\lambda + \varphi^T(t-1)P(t-1)\varphi(t-1)\right]^{-1}, \tag{2.38}$$

where λ is the forgetting factor [22].

A commonly used linearized time-invariant model for winding process in literature is:

$$\begin{cases} \dot{V}_u = \dfrac{R_u^2}{J_u}T_w - \dfrac{B_f}{J_u}V_u + \dfrac{R_u}{J_u}K_m I_u \\ \dot{V}_w = -\dfrac{R_w^2}{J_w}T_w - \dfrac{B_f}{J_w}V_w + \dfrac{R_w}{J_w}K_m I_w \\ \dot{T}_w = -\dfrac{v_{w0}}{L}T_w - \dfrac{aE}{L}V_u + \dfrac{aE}{L}V_w \end{cases}$$

The third equation has an operating value of the winding velocity. When a square wave reference is set for the line speed, this operating speed value reaches an equivalence of zero. All velocity changes, in this case, correspond to the real-time velocities. The first two equations are used to determine the viscous friction coefficient B_f, and the motor torque constant K_m. The third equation was mainly used in this work to estimate Young's modulus of the web material. The discrete time counterpart of the model representation is

$$v_u(t) = \underbrace{\frac{J_u}{J_u + B_f T_s}}_{a_{u1}} v_u(t-1) + \underbrace{\frac{R_u^2 T_s}{J_u + B_f T_s}}_{b_{u1}} t_w(t) + \underbrace{\frac{R_u T_s K_m}{J_u + B_f T_s}}_{b_{u2}} i_u(t); \tag{2.39}$$

$$v_w(t) = \underbrace{\frac{J_w}{J_w + B_f T_s}}_{a_{w1}} v_u(t-1) - \underbrace{\frac{R_w^2 T_s}{J_w + B_f T_s}}_{b_{w1}} t_w(t) + \underbrace{\frac{R_w T_s K_m}{J_w + B_f T_s}}_{b_{w2}} i_w(t); \tag{2.40}$$

$$T_w(t) = \underbrace{\frac{L}{L + T_s v_{w0}}}_{a_{t1}} T_w(t-1) - \underbrace{\frac{aET_s}{L + T_s v_{w0}}}_{b_{t1}} v_u(t) + \underbrace{\frac{aET_s}{L + T_s v_{w0}}}_{b_{t2}} v_w(t). \tag{2.41}$$

For example, the RLS estimation distributions based on one data set are shown in **Figure 2.14** to **Figure 2.16**.

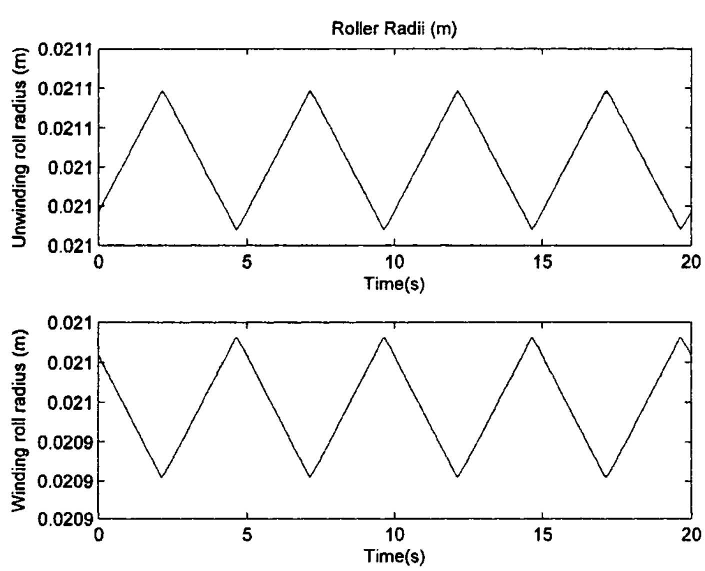

Figure 2.13 Radii changes during estimation.

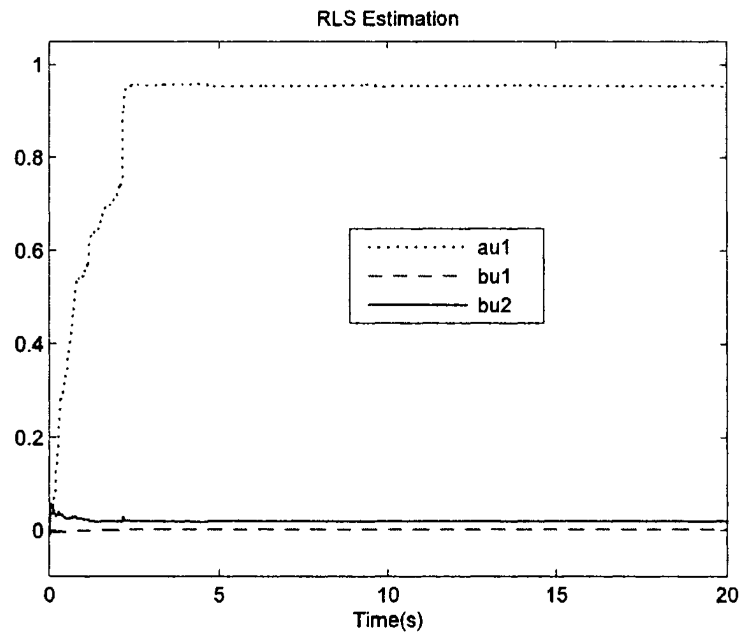

Figure 2.14 RLS estimation on equation (2.39).

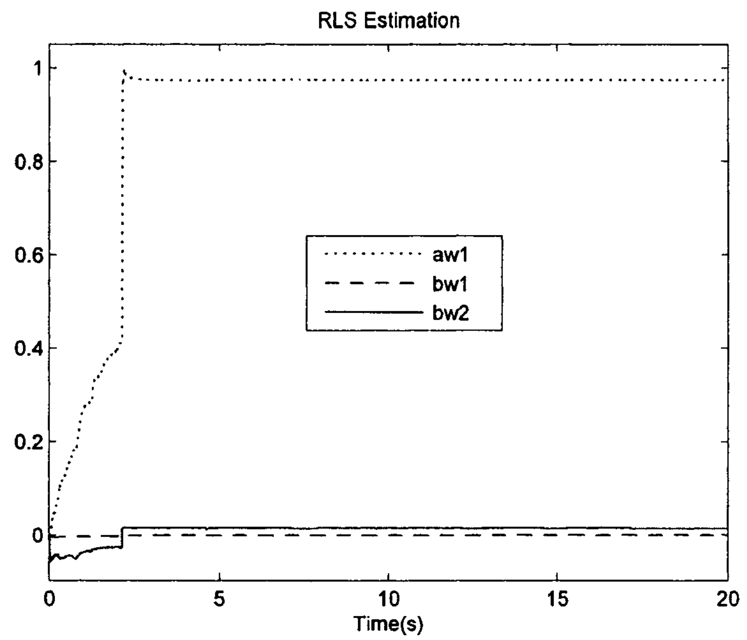

Figure 2.15 RLS estimation on equation (2.40).

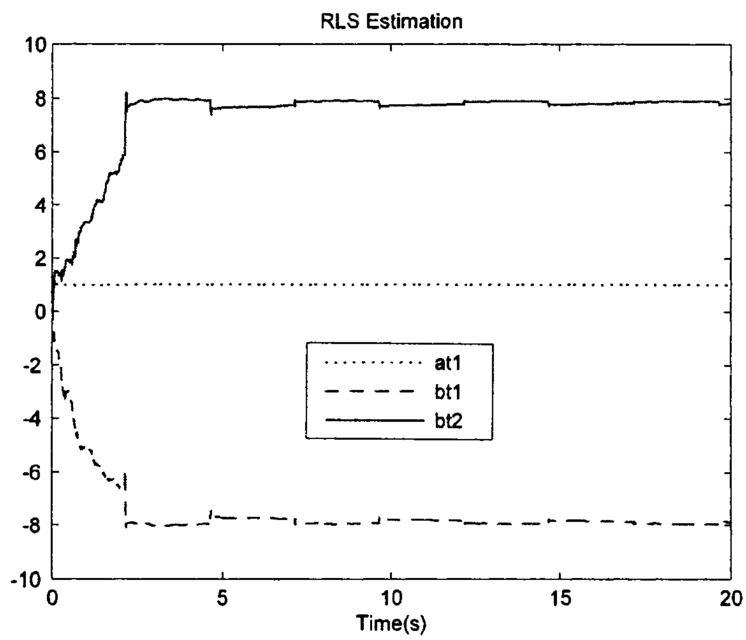

Figure 2.16 RLS estimation on equation (2.41).

The following parameters are identified by the recursive least square method.

E	$1.7\ GPa$	K_m	$0.185\ N \cdot m / A$
B_f	$0.008\ N \cdot m / (rad / s)$	J	$2.19 \times 10^{-4}\ kg \cdot m^2$

Other parameter values are measured or specified as:

$a = 3.376 \times 10^{-6}\ m^2$;

$L_2 = 0.725\ m$;

$R = 0.02\ m$;

$v_{10} = v_{20} = 0.4\ m/\sec$.

This numerical realization is applied in this work for controller design and robustness analysis.

2.2.4 H_∞ Controller

One of the suboptimal H_∞ controllers can be derived for the considered general H_∞ problem by solving two algebraic Riccati equations [16] [21]. For example, one can be represented by the following transfer functions:

$$K(s) = \begin{pmatrix} K_{11}(s) & K_{12}(s) \\ K_{21}(s) & K_{22}(s) \end{pmatrix},$$

where

$$K_{11}(s) = \frac{-590.2s^6 - 7.331e5s^5 - 6.203e7s^4 - 8.47e9s^3 - 8.429e10s^2 - 2.174e11s - 2.166e9}{s^7 + 2855s^6 + 3.369e6s^5 + 1.668e9s^4 + 1.74e10s^3 + 4.653e10s^2 + 4.062e9s + 3.598e7};$$

$$K_{12}(s) = \frac{3416s^5 + 5.808e6s^4 + 4.919e9s^3 + 1.768e11s^2 + 1.403e12s + 3.203e12}{s^6 + 2855s^5 + 3.369e6s^4 + 1.668e9s^3 + 1.727e10s^2 + 4.515e10s + 4.498e8};$$

$$K_{21}(s) = \frac{679.8s^6 + 8.692e5s^5 + 5.559e7s^4 + 8.084e9s^3 + 8.098e10s^2 + 2.096e11s + 2.088e9}{s^7 + 2855s^6 + 3.369e6s^5 + 1.668e9s^4 + 1.74e10s^3 + 4.653e10s^2 + 4.062e9s + 3.598e7};$$

$$K_{22}(s) = \frac{3467s^5 + 5.81e6s^4 + 4.919e9s^3 + 1.768e11s^2 + 1.403e12s + 3.203e12}{s^6 + 2855s^5 + 3.369e6s^4 + 1.668e9s^3 + 1.727e10s^2 + 4.515e10s + 4.498e8}.$$

2.3 Other Control Strategies

2.3.1 LQR Tracking Control

Suppose that there is a plant model with a state-space representation as

$$\begin{cases} \dot{x}_p = A_n x_p + B_{n1} d + B_{n2} u \\ y = C_n x_p \end{cases}.$$

A general linear quadratic regulator (LQR) design is to derive an LQR feedback gain $u = -Kx_p$ to stabilize the system and to minimize a cost function, which could be

$$J = \int_0^\infty \left\{ x_p^T Q x_p + 2x_p^T N u + u^T R u \right\} dt \tag{2.42}$$

or

$$J = \int_0^\infty \left\{ y^T Q y + 2 y^T N u + u^T R u \right\} dt, \tag{2.43}$$

depending on if only the output or all state variables shall be optimized. The cross weighting matrix N is omitted in this work (set to zero). Weighting matrices Q and R are positive definite real matrices, which define the tradeoff between regulation performance (how fast $\beta(t)$ goes to zero) and control effort u.

The synthesis is to solve the Riccati equation

$$PA_n + A_n^T P - PB_{n2} R^{-1} B_{n2}^T P + Q = 0 \tag{2.44}$$

to get the solution of P. Then we can derive the LQR state feedback gain:

$$K = R^{-1} B_{n2}^T P .$$

The state feedback closed-loop system is shown in **Figure 2.17**.

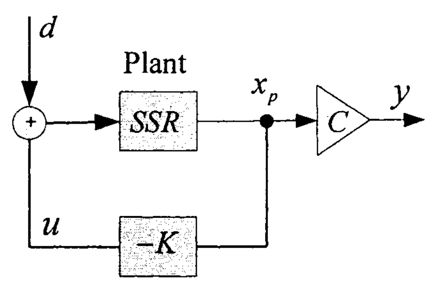

Figure 2.17 LQR state feedback control .

However, for a tracking control, the variable to be minimized is changed to the tracking error instead. It means that the cost function needs to be modified correspondingly as

$$J = \int_0^\infty \left\{ e^T Q e + u^T R u \right\} dt . \tag{2.45}$$

To eliminate the steady state error of the output, an integral control is introduced. The closed-loop system with an LQR tracking control is illustrated in **Figure 2.18**.

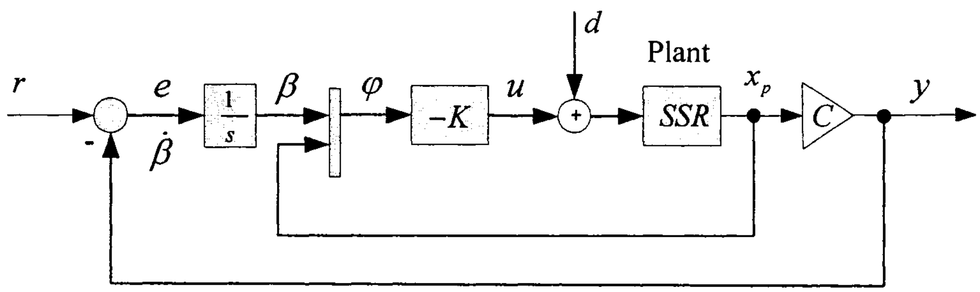

Figure 2.18 LQR tracking control.

The LQR state feedback design also needs to be modified correspondingly based on an augmented system. The output error signals are represented by

$$\dot{\beta} = e = r - y = r - C_n x_p .$$

Consider β a new state variable. The augmented state vector becomes

$$\varphi = \begin{bmatrix} \beta & x_p \end{bmatrix}^T .$$

If β is taken as the system output instead, the augmented state-space representation will be

$$\begin{cases} \dot{\varphi} = A_{naug}\varphi + B_{n1aug}d + B_{n2aug}u + B_r r \\ \beta = C_{\beta aug}\varphi \end{cases},$$

with

$$A_{naug} = \begin{bmatrix} 0 & -C_n \\ 0 & A_n \end{bmatrix};\ B_{n1aug} = \begin{bmatrix} 0 \\ B_{n1} \end{bmatrix};\ B_{n2aug} = \begin{bmatrix} 0 \\ B_{n2} \end{bmatrix};\ B_r = \begin{bmatrix} I \\ 0 \end{bmatrix};\ C_{\beta aug} = \begin{bmatrix} I & 0 \end{bmatrix}.$$

Considering that the tracking errors are normally not zero-mean periodic signals, the cost function in (2.45) can be equivalently replaced by a cost function in (2.46), with respect to β instead of the direct error signal e.

$$J = \int_0^{\infty} \left\{ \beta^T Q \beta + u^T R u \right\} dt . \tag{2.46}$$

And the corresponding Riccati equation becomes

$$PA_{naug} + A_{naug}^T P - PB_{n2aug} R^{-1} B_{n2aug}^T P + Q = 0 . \tag{2.47}$$

The state feedback gain for tracking control can be derived by solving the above Riccati equation. It yields

$$K = R^{-1} B_{n2aug}^{T} P .$$

Weighting matrices Q and R are selected based on the considerations as follows:

- To achieve good control performance;
- To reduce the tracking error (by limiting β);
- To limit the control effort and avoid actuator saturation;
- To obtain the best balance among the robust properties of the closed-loop system.

The two weighting matrices are finally tuned as:

$$Q = \begin{bmatrix} 1 & 0 \\ 0 & 1000 \end{bmatrix};\ R = \begin{bmatrix} 1 & 0 \\ 0 & 1 \end{bmatrix}.$$

The first column in Q and R corresponds to the tracking error of tension output and the second corresponds to the tracking error of line speed output. Although an increase in the weight of tension tracking error can improve system robust stability, the transient tension control performance will become worse.

The derived feedback gain is

$$K = \begin{bmatrix} 0.7020 & -22.5206 & 0.0005 & 0.4931 & 0.0818 \\ -0.7122 & -22.1996 & 0.0024 & 0.0818 & 0.4968 \end{bmatrix}.$$

2.3.2 PI Control

Decentralized PI control for web handling systems has been investigated for decades and prevails in real-world industrial applications due mainly to its advantage in implementation. This SISO PI-based control is designed based on decoupled speed loop and tension loop and can be simply implemented regardless of the interaction between tension and speed. As introduced in **Chapter 1**, without feedforward compensations, the transient performance of both speed control and tension control could not be satisfactory. The decoupling technique and feedforward loop design can be found in several references, e.g. [4], [23] and [24].

In this work, no feedforward compensation design is considered. To illustrate the conventional PI-based decentralized web system control, two PI controllers are separately applied to the two driving motors in a single intermediate web span. One of the controllers is in charge of line speed control, while the other one takes tension feedback signal and control the web tension. The configuration is illustrated in **Figure 2.19**.

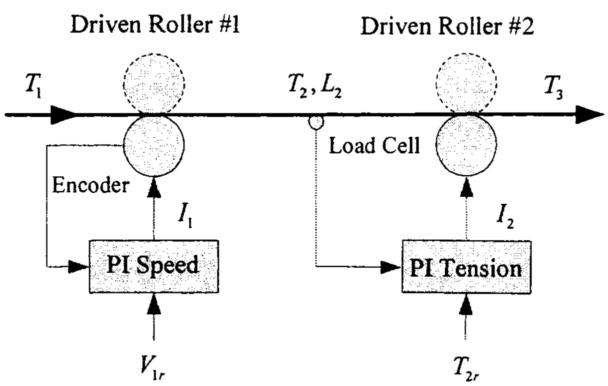

Figure 2.19 Decentralized PI Control.

The formulas of PI controllers are:

$$I_1 = K_{p1}e_V(t) + K_{i1}\int e_V(t)dt\,;$$

$$I_2 = K_{p2}e_T(t) + K_{i2}\int e_T(t)dt\,.$$

where e_V and e_T are the tracking error of line speed and tension output signal, respectively.

The proportional and integral gains, K_p and K_i, are tuned by trial and error as:

Speed control loop: $K_{p1} = 4$, $K_{i1} = 20$,

Tension control loop: $K_{p2} = 0.11$, $K_{i2} = 2$.

The decentralized PI control can be represented by

$$K=\begin{bmatrix} 0 & \dfrac{4s+20}{s} \\ \dfrac{0.11s+2}{s} & 0 \end{bmatrix}=\left[\begin{array}{cc|cc} 0 & 0 & 2 & 0 \\ 0 & 0 & 0 & 4 \\ \hline 0 & 5 & 0 & 4 \\ 1 & 0 & 0.11 & 0 \end{array}\right]$$

2.4 Robustness Property Analysis

Robust stability, nominal performance and robust performance, the three main robustness properties, are analyzed in this section for the closed-loop system controlled by the designed H_∞ controller, LQR and PI controller, respectively.

2.4.1 General Robustness Analysis

To describe the closed-loop system for the purpose of robustness analysis, the LFT standard framework, shown in **Figure 2.8**, is transformed first into a Δ-M structure as illustrated in **Figure 2.20**. During the derivation of P, weighting functions were considered in order to design a best compensating H_∞ controller. However, they do not actually exist in a practical system. Therefore, for the purpose of robustness analysis, the exogenous input/output vectors are changed to $z=e=r-y$; and $w=\begin{bmatrix} d & r \end{bmatrix}^T$. Correspondingly, without considering any weighting functions, the state-space representation of the interconnection system P in **Figure 2.20** should also be modified.

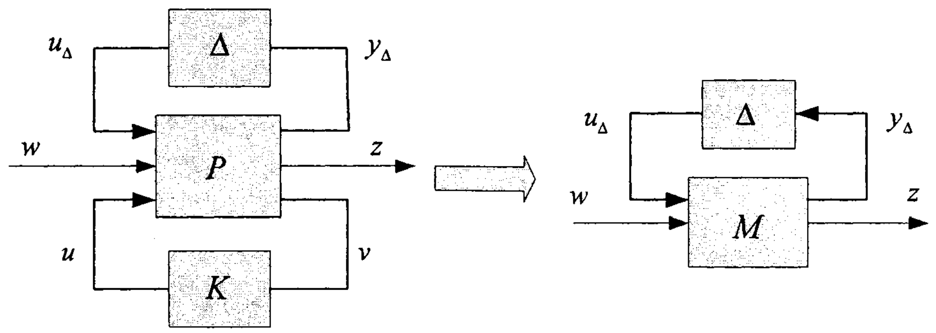

Figure 2.20 The Δ-M structure.

With the representation of the interconnection system P in (2.28), applying lower LFT yields

$$M_{11}(s) = F_l\left\{\begin{bmatrix} P_{00} & P_{02} \\ P_{20} & P_{22} \end{bmatrix}, K\right\} = P_{00} + P_{02}(I - KP_{22})^{-1}KP_{20}, \tag{2.48}$$

$$M_{22}(s) = F_l\left\{\begin{bmatrix} P_{11} & P_{12} \\ P_{21} & P_{22} \end{bmatrix}, K\right\} = P_{11} + P_{12}(I - KP_{22})^{-1}KP_{21}, \tag{2.49}$$

$$\begin{aligned} M(s) &= \begin{bmatrix} M_{11} & M_{12} \\ M_{21} & M_{22} \end{bmatrix} \\ &= F_l\left\{\left[\begin{array}{cc|c} P_{00} & P_{01} & P_{02} \\ P_{10} & P_{11} & P_{12} \\ \hline P_{20} & P_{21} & P_{22} \end{array}\right], K\right\} = F_l\left\{\begin{bmatrix} G_{11} & G_{12} \\ G_{21} & G_{22} \end{bmatrix}, K\right\} = G_{11} + G_{12}(I - KG_{22})^{-1}KG_{21}. \end{aligned} \tag{2.50}$$

The state-space realization of lower LFT in (2.16) should be adopted in Matlab, such that a state-space representation of the closed-loop system can be derived to facilitate the numerical robustness analysis.

Several concepts need to be explained first:

- **Internal stability**: The transfer matrix $M(s)$ is stable, i.e. $M_{11}(s)$, $M_{12}(s)$, $M_{21}(s)$ and $M_{22}(s)$ are all stable;
- **Robust stability**: The set of closed-loop systems represented by the above Δ-M structure are internally stale for all possible $\Delta(s)$;
- **Nominal performance**: If a nominal closed-loop system $M(s)$ is internally stable, it achieves nominal performance if and only if the energy of the exogenous output z due to disturbances (references) with energy bounded by 1 is also bounded by 1. This can be stated by

  $\|z(s)\|_2 \leq 1, \ \forall \ \|w(s)\|_2 \leq 1$.
- **Robust performance**: A closed-loop system with a Δ-M structure achieves robust performance if and only if all members of the family of plants described by the

interconnection of $M(s)$ and $\Delta(s)$ achieve nominal performance. It means the output z should have bounded energy for all disturbances (references) with bounded energy and for all possible plant models. This can be stated by

$\|z(s)\|_2 \le 1,\ \forall\ \|w(s)\|_2 \le 1,\ \forall\ \Delta(s)$ such that $\|\Delta(s)\|_\infty \le 1$.

Robustness evaluation can be implemented by singular value analysis or structured singular value (μ) analysis. The former is an H_∞-norm based method, while the criterion of the latter is structured singular values. The structured singular value μ is defined as

$$\mu_\Delta(M) = \frac{1}{\min\{\bar{\sigma}(\Delta):\ \Delta \in \Delta_s, \det(I - M\Delta) = 0\}}, \tag{2.51}$$

where Δ_s is the set of all possible perturbation blocks Δ in a Δ-M structure. The upper and lower μ bounds with respect to a specified perturbation block structure can be derived over a specific bandwidth. Define an augmented uncertainty block structure

$$\tilde{\Delta} = \begin{bmatrix} \Delta & 0 \\ 0 & \Delta_p \end{bmatrix}, \tag{2.52}$$

where $\|\Delta\|_\infty \le 1$ and $\|\Delta_p\|_\infty \le 1$. Δ_p is a full complex block with a size corresponding to the input/output dimension of M_{22}. Robustness analyses are then conducted by:

1) **Robust stability**: the system achieves robust stability iff $\|M_{11}\|_\infty < 1$ (singular value analysis), or $\mu_\Delta(M_{11}) < 1$ (μ-analysis), for all $\|\Delta\|_\infty \le 1$;
2) **Nominal performance**: the system has nominal performance iff $\|M_{22}\|_\infty < 1$ (singular value analysis), or $\mu_{\Delta p}(M_{22}) < 1$ (μ-analysis), for all $\|\Delta_p\|_\infty \le 1$;
3) **Robust performance**: the system achieves robust performance iff $\|F_u(\mathrm{M}, \Delta)\|_\infty < 1$, for all $\|\Delta\|_\infty \le 1$ (singular value analysis), or $\mu_{\tilde{\Delta}}(M) < 1,\ \forall\ \|\tilde{\Delta}\|_\infty \le 1$ (μ-analysis).

Here are several remarks on robustness analysis:

1. $\|M_{11}\|_\infty < 1$ implies stability, but not conversely, because this test ignores the known block diagonal structure of the uncertainties (Δ) and is equivalent to regarding as Δ

unstructured. A stable system can have arbitrarily large $\| M_{11} \|_{\infty}$. The conservativeness of this test will be illustrated by the testing results.

2. The two methods will give same results in nominal performance test. Δ_p is a full unstructured complex block. For such unstructured uncertainties, an alternative definition of the largest singular value can be derived as [16]

$$\bar{\sigma}(M_{22}) = \frac{1}{\inf\{\bar{\sigma}(\Delta_p):\ \det(I - M_{22}\Delta_p) = 0\}}$$

   This matches the corresponding definition of structured singular value.

3. For singular value robust performance test, the robust performance condition can be made equivalent to a robust stability condition with the augmented perturbation block $\tilde{\Delta}$ [25]. However, in this work, the robust performance by singular value analysis will be illustrated only for the situation in which Δ is an identity matrix, i.e. all parameters increases to their maximum values.

The general robustness analysis can be applied directly to the output feedback control systems, e.g. H_{∞} controller and PI control. However, for LQR tracking control, an augmented state-space plant model should be considered in the derivation of the corresponding Δ-M structure.

2.4.2 Robustness Analysis of LQR Control

Assume that we have got an SSR of the plant with uncertainty as in (2.12). LQR tracking control introduces a new state β, which satisfies

$$\dot{\beta} = e = r - y = r - C_{u1}x_p.$$

Consider that the exogenous output $z = e$ and the exogenous input $w = \begin{bmatrix} d & r \end{bmatrix}^T$. The SSR of corresponding augmented system with respect to an augmented state vector $\varphi = \begin{bmatrix} \beta & x_p \end{bmatrix}^T$ is

$$\begin{cases} \dot{\varphi} = A_{aug}\varphi + B_{0aug}u_{\Delta} + \begin{bmatrix} B_{1aug} & B_r \end{bmatrix} w + B_{2aug}u \\ y_{\Delta} = C_{0aug}\varphi + D_{u00}u_{\Delta} + \begin{bmatrix} D_{u01} & 0 \end{bmatrix} w + D_{u02}u \\ e = -C_{1aug}\varphi + \begin{bmatrix} 0 & I \end{bmatrix} w \end{cases}, \tag{2.53}$$

where

$$A_{aug} = \begin{bmatrix} 0 & -C_n \\ 0 & A_u \end{bmatrix};\ B_{0aug} = \begin{bmatrix} 0 \\ B_{u0} \end{bmatrix};\ B_{1aug} = \begin{bmatrix} 0 \\ B_{u1} \end{bmatrix};\ B_{2aug} = \begin{bmatrix} 0 \\ B_{u2} \end{bmatrix};\ B_r = \begin{bmatrix} I \\ 0 \end{bmatrix};$$

$$C_{0aug} = \begin{bmatrix} 0 & C_{u0} \end{bmatrix};\ C_{1aug} = \begin{bmatrix} 0 & C_{u1} \end{bmatrix}.$$

The SSR of the closed-loop system can be derived by substituting $u = -K\varphi$ into (2.45).

$$\begin{cases} \dot{\varphi} = (A_{aug} - B_{2aug}K)\varphi + B_{0aug}u_{\Delta} + \begin{bmatrix} B_{1aug} & B_r \end{bmatrix} w \\ y_{\Delta} = (C_{0aug} - D_{u02}K)\varphi + D_{u00}u_{\Delta} + \begin{bmatrix} D_{u01} & 0 \end{bmatrix} w \\ e = -C_{1aug}\varphi + \begin{bmatrix} 0 & I \end{bmatrix} w \end{cases}. \tag{2.54}$$

A Δ-M structure representing the above closed-loop system is shown in **Figure 2.21**.

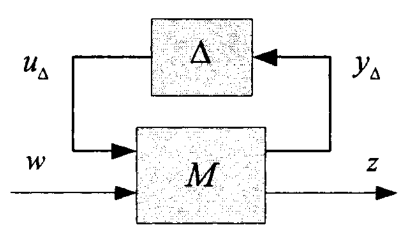

Figure 2.21 The Δ-M structure of LQR control.

The following expression can be derived based on the above transformations.

$$\begin{bmatrix} y_\Delta \\ z \end{bmatrix} = M \begin{bmatrix} u_\Delta \\ w \end{bmatrix}$$
$$= \begin{bmatrix} M_{11} & M_{12} \\ M_{21} & M_{22} \end{bmatrix} \begin{bmatrix} u_\Delta \\ w \end{bmatrix}$$
$$= \left[\begin{array}{c|cc} A_{aug} - B_{2aug}K & B_{0aug} & \begin{bmatrix} B_{1aug} & B_r \end{bmatrix} \\ \hline C_{0aug} - D_{u02}K & D_{u00} & \begin{bmatrix} D_{u01} & 0 \end{bmatrix} \\ -C_{1aug} & 0 & \begin{bmatrix} 0 & I \end{bmatrix} \end{array}\right] \begin{bmatrix} u_\Delta \\ w \end{bmatrix};$$
$$= \left[\begin{array}{c|cc} A_m & B_{m1} & B_{m2} \\ \hline C_{m1} & D_{m11} & D_{m12} \\ C_{m2} & D_{m21} & D_{m22} \end{array}\right] \begin{bmatrix} u_\Delta \\ w \end{bmatrix}$$

$$M_{11} = \left[\begin{array}{c|c} A_m & B_{m1} \\ \hline C_{m1} & D_{m11} \end{array}\right]; \; M_{22} = \left[\begin{array}{c|c} A_m & B_{m2} \\ \hline C_{m2} & D_{m22} \end{array}\right].$$

The general robustness analysis can then be implemented on the derived closed-loop representation.

2.4.3 Robustness Analysis Results

Table 2.2 shows the H_∞ norms of the controlled closed-loop systems. The uncertain factors δ_i are considered as $\delta_R = 0.1$; $\delta_L = 0.05$; $\delta_v = 0.1$; $\delta_E = 0.01$. In the derivation of $\|F_u(M, \Delta)\|_\infty$, Δ is taken as an identity matrix for the singular value test.

Table 2.2 H_∞ norms of the closed-loop systems with designed controllers.

	$\|M_{11}\|_\infty$	$\|M_{22}\|_\infty$	$\|F_u(M, \Delta)\|_\infty$
H_∞ Controller	2.5569	1.1158	1.1371
LQR	6.7195	3.6995	4.0278
PI Controller	5.0574	49.6259	48.9921

Figure 2.22 through **Figure 2.24** illustrate the results of robustness property analysis by using singular value and μ value testing tools. Nominal and robust performance tests of PI controller are not plotted here because the norm values are too large.

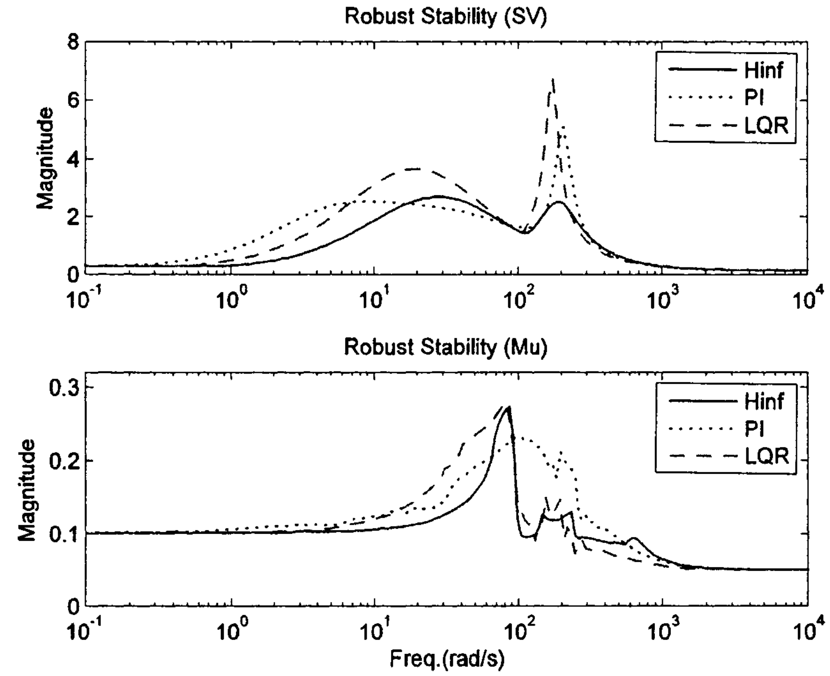

Figure 2.22 Robust stability analysis (H_∞, PI and LQR).

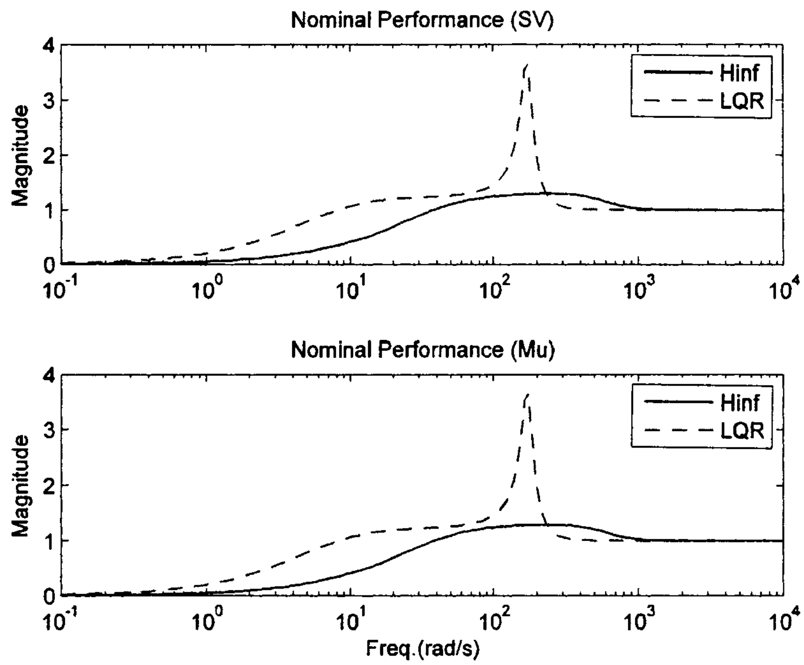

Figure 2.23 Nominal performance analysis (H_∞ and LQR).

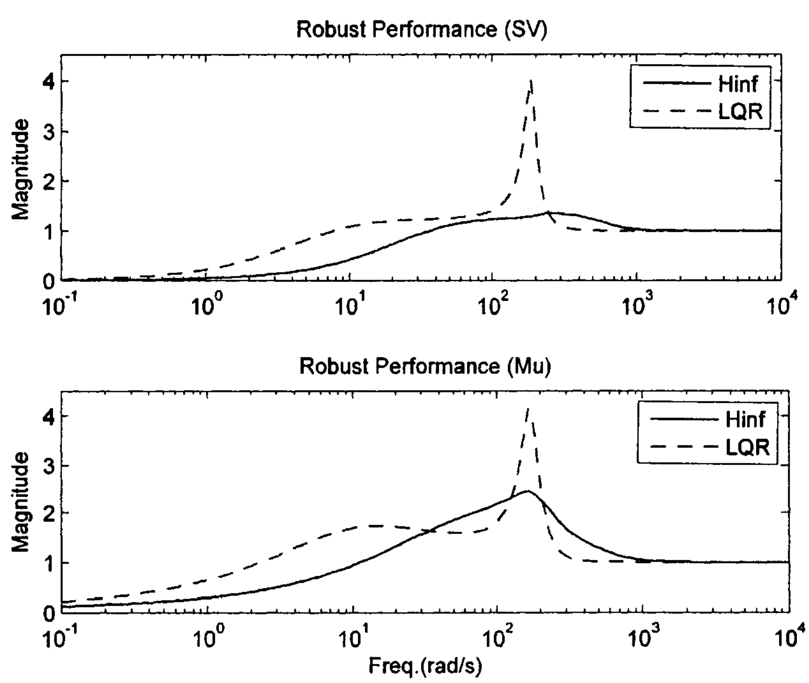

Figure 2.24 Robust performance analysis (H_∞ and LQR).

It is seen that with the specified parametric uncertainties and selected weighting functions, the closed-loop system, controlled by any one of the three controllers, achieves robust stability, in a sense of μ analysis. The proposed H_∞ control presents the best results in nominal and robust performance tests, and performs best in robust stability test but only in a sense of singular value analysis. Furthermore, it can also be illustrated that the singular value analysis is more conservative than μ-analysis for robust stability test, when the system has structured uncertainties as in this work. Robust performance test can not be fulfilled by using singular value analysis since the uncertainty block Δ could have infinite patterns. μ-analysis brings a test result, through which it can be illustrated that no controller achieves robust performance.

2.4.4 Robust Stability and Parametric Uncertainties

In real-world industrial applications, an important issue is to investigate the impact that each parameter variation could have on system stability. If the impacts can be quantified by numerical analysis, it will be helpful for engineers to determine the accuracy level or tolerance of electrical/mechanical components. To explore this issue for web handling systems in this work, one parameter is set to vary while the others are kept as their nominal values. **Figure 2.25** shows the impacts on robust stability (using H_∞ norm analysis for demonstration). In deriving the results, each parameter goes through identical variation in the range of $\pm10\%$ of its nominal value and the plant is controlled by the designed H_∞ controller. It is seen that the web length, cross-sectional area, and Young's modulus have the most significant influence on system robust stability. This result provides a valuable reference for the robust stability acquisition in a multistage web system.

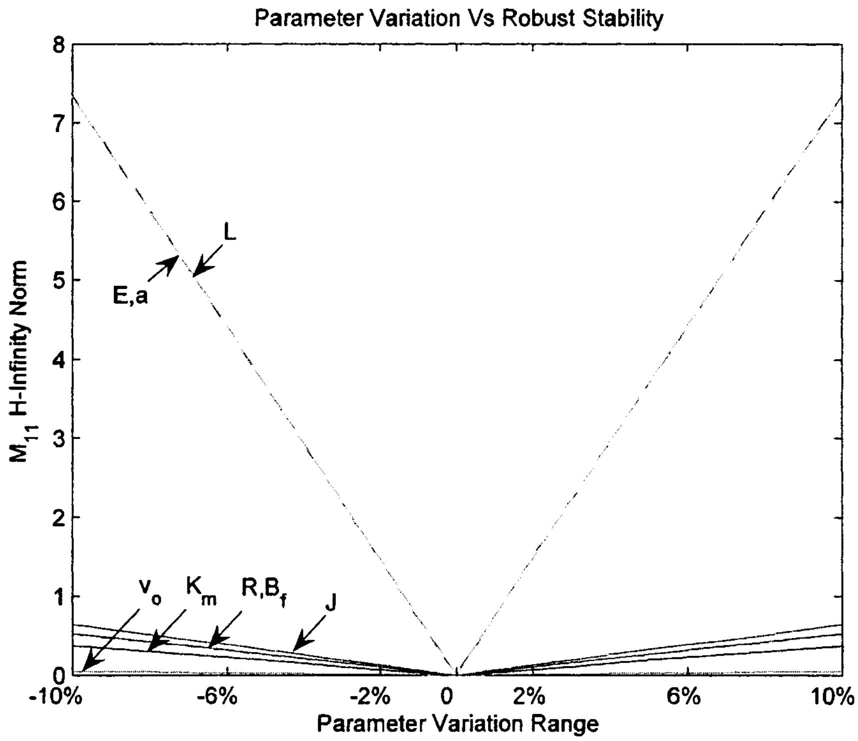

Figure 2.25 Robust stability and parametric uncertainties.

2.5 Evaluation and Comparison

In order to verify the viability of the proposed robust H_∞ controller, a comparison study is taken in this section based on both simulation and experimental tests.

2.5.1 Simulation Tests

In this work, two centralized MIMO controllers, the proposed H_∞ controller and a Linear-quadratic regulator (LQR), are implemented. In addition, a SISO PI-based decentralized control strategy is also designed and implemented to the decoupled tension control loop and speed control loop. Control performance evaluation of the three controllers is conducted by simulation tests under two operating conditions. **Figure 2.26** shows the simulation results without plant disturbances. **Figure 2.27** and **Figure 2.28** illustrate the simulation results with an upstream tension disturbance.

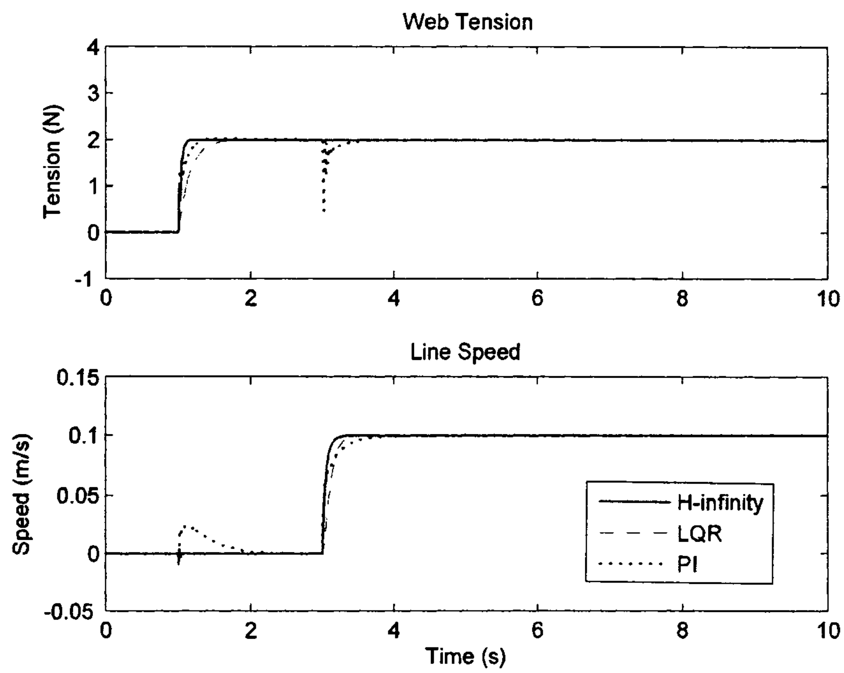

Figure 2.26 Simulation: H_∞, LQR, and PI control.

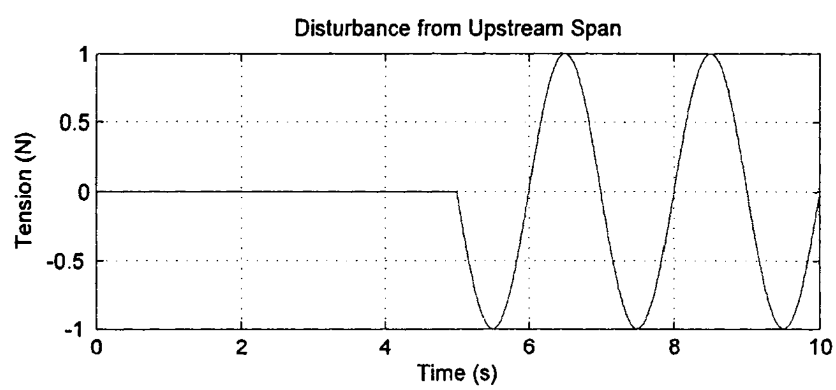

Figure 2.27 Upstream tension disturbance.

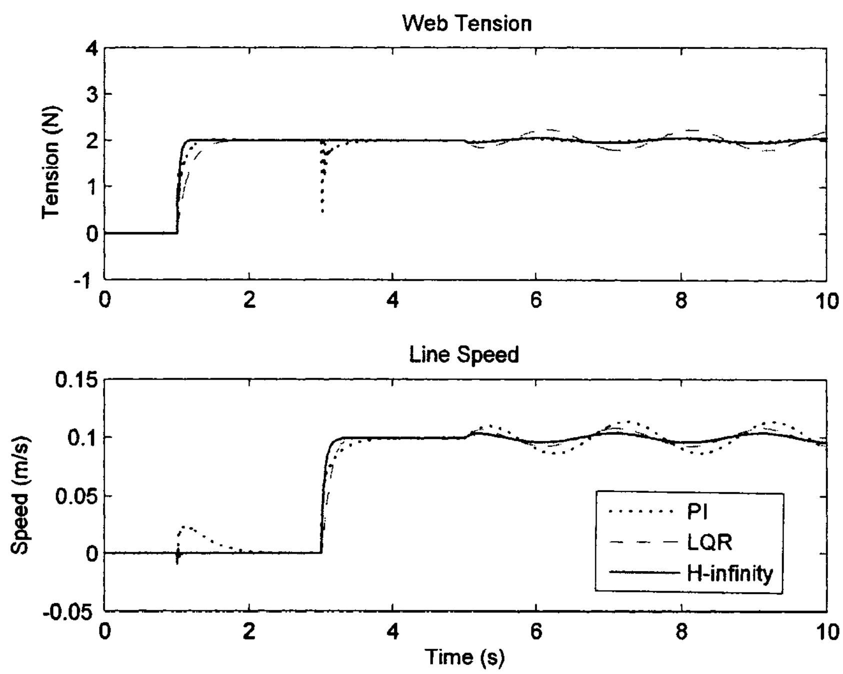

Figure 2.28 Simulation: H_∞, LQR, and PI control with upstream disturbance.

It is clear from examining these simulation results that the proposed H_∞ controller performs best in terms of the rising time and disturbance rejection. Furthermore, the advantage of centralized MIMO control design can also be recognized. When the two driving motors of the web span are controlled, respectively, by a PI tension controller and a PI speed controller, if web speed varies, web tension fluctuates dramatically and vice versa. On the other hand, the centralized MIMO controllers, H_∞ and LQR, can effectively attenuate the interaction between tension and speed. Furthermore, the proposed H_∞ controller presents the best disturbance rejection among all three controllers.

In real experiments or applications, measurement noise is unavoidable and will affect the control performance through the feedback loop. Simulation tests when considering white measurement noise are shown in **Figure 2.29** through **Figure 2.32**.

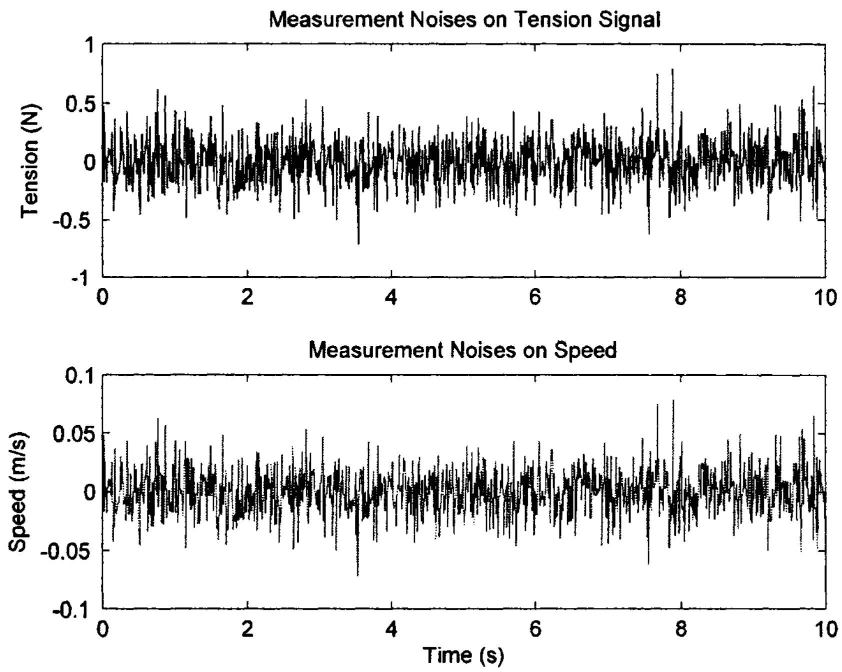

Figure 2.29 Measurement noises.

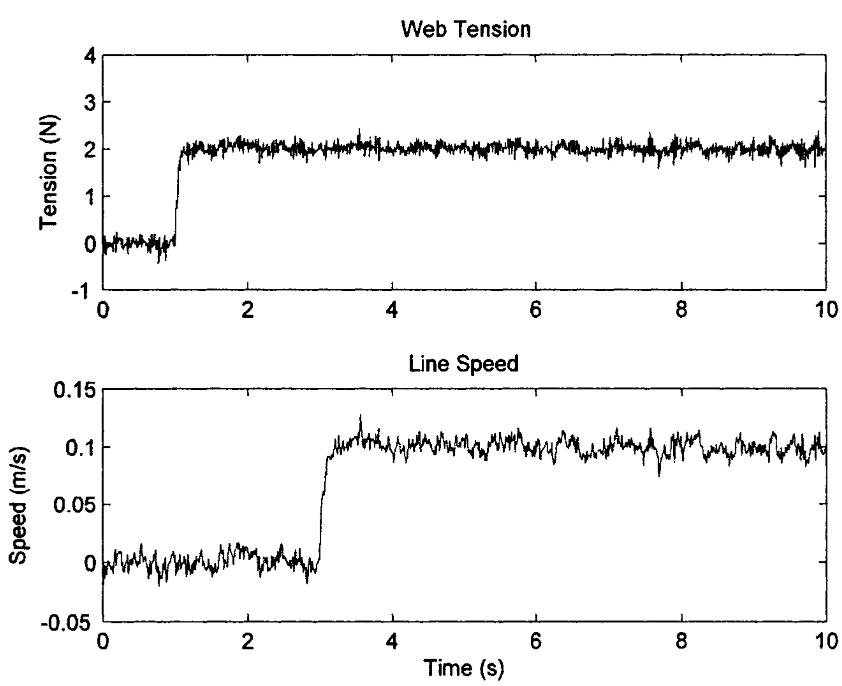

Figure 2.30 Simulation: H_∞ control with measurement noise.

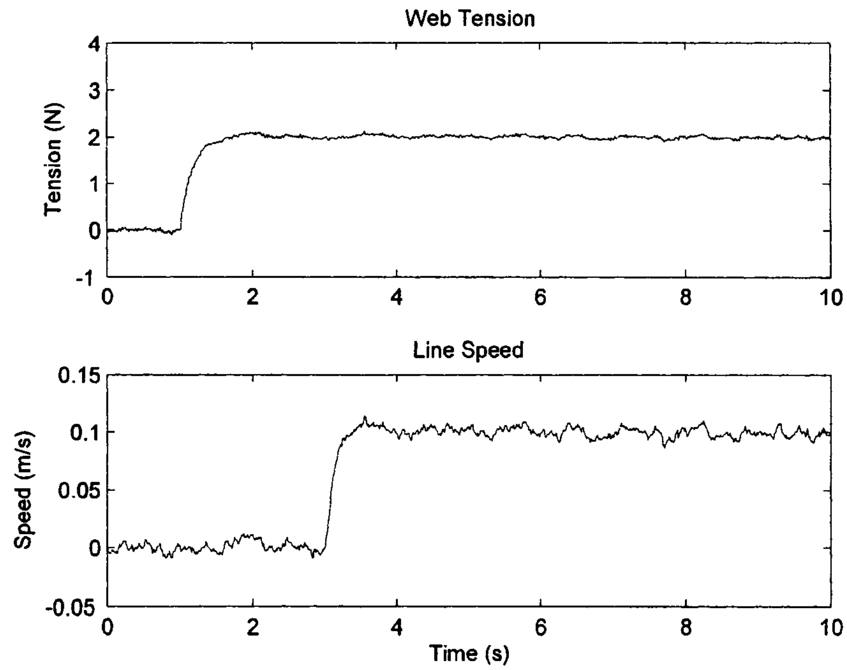

Figure 2.31 Simulation: LQR control with measurement noise.

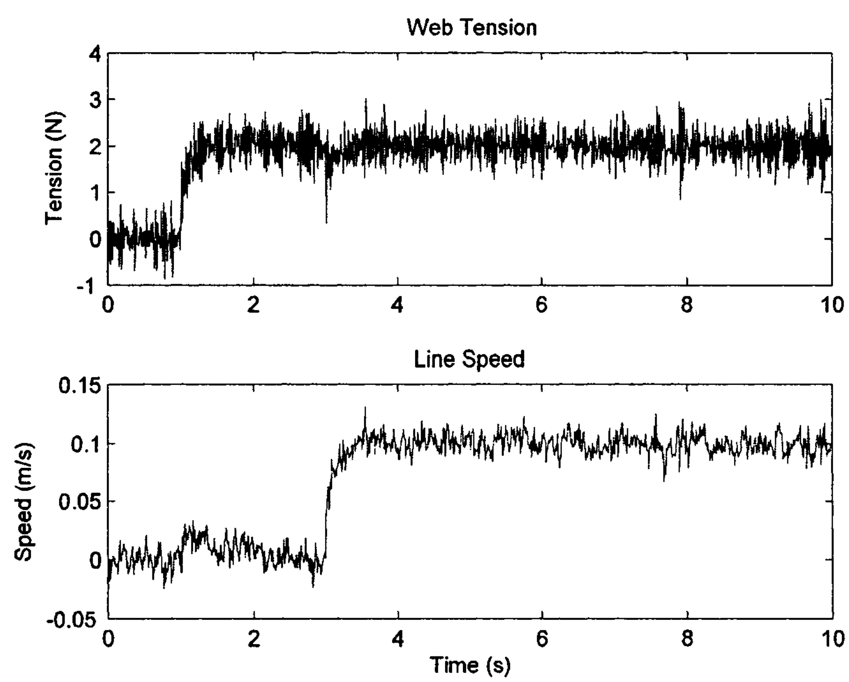

Figure 2.32 Simulation: PI control with measurement noise.

It is illustrated that PI control is very sensitive to tension measurement noise. This cannot be improved even when the gains are adjusted, although the disturbance rejection of PI control can be significantly improved by adjusting the gains. It implies that in the real experiments, PI control will rely on feedback signal processing much more than LQR and H_∞ controllers do.

2.5.2 Experimental Tests

Figure 2.33 shows a two-span web system configured by using the testing apparatus in LIMS (Laboratory for Intelligent Mechatronic Systems). The testing apparatus contains two identical drive units. Each of the units consists of two 24V brush-commutated DC servo motors and two idler shafts. The DC motors are powered and controlled through a linear current multi-channel drive unit. Each motor can be controlled separately to simulate various drive/load configurations. Eight 2048-line encoders and a rotational tension measurement transducer are mounted to measure the shaft angular displacements and the web tension. The testing apparatus is ideal for implementing multi-stage web system control strategies.

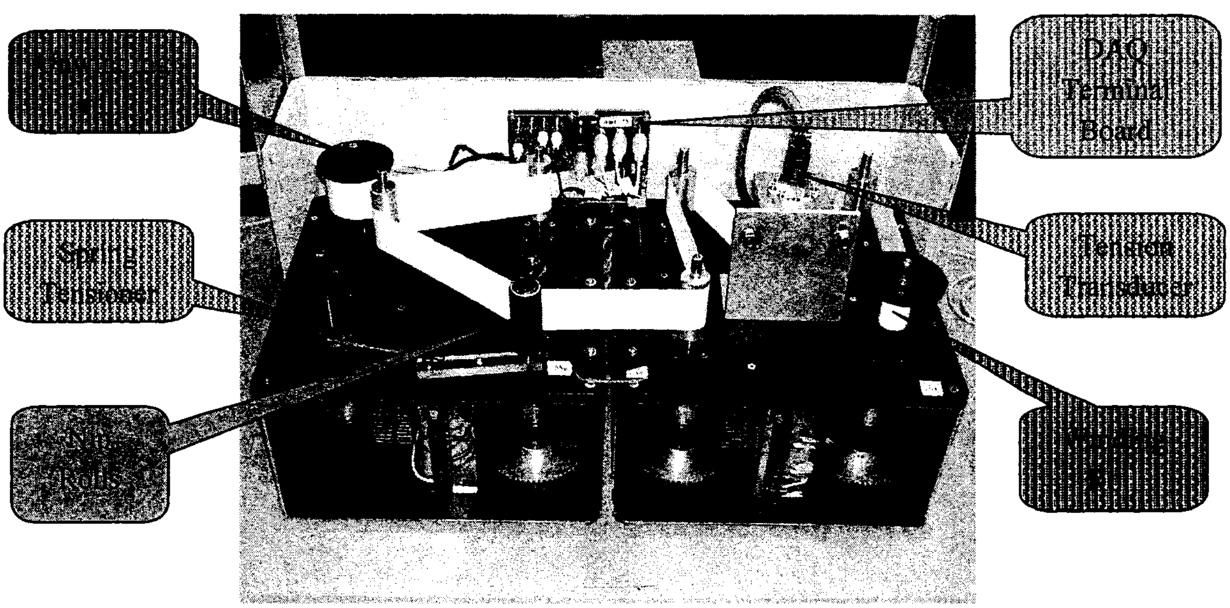

Figure 2.33 Testing apparatus.

To test the designed controllers on a typical single intermediate web span, an experimental setup is configured as shown in **Figure 2.34**.

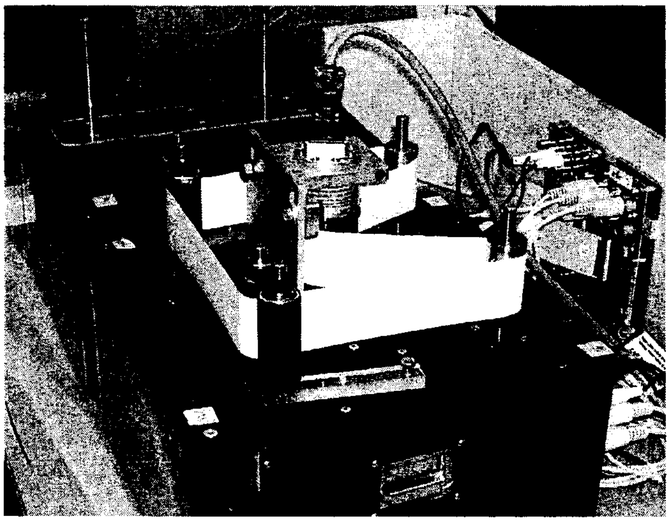

Figure 2.34 Single intermediate span setup.

Wincon system is adopted for the real time implementation. The overall configuration is illustrated by the block diagram in Figure 2.35.

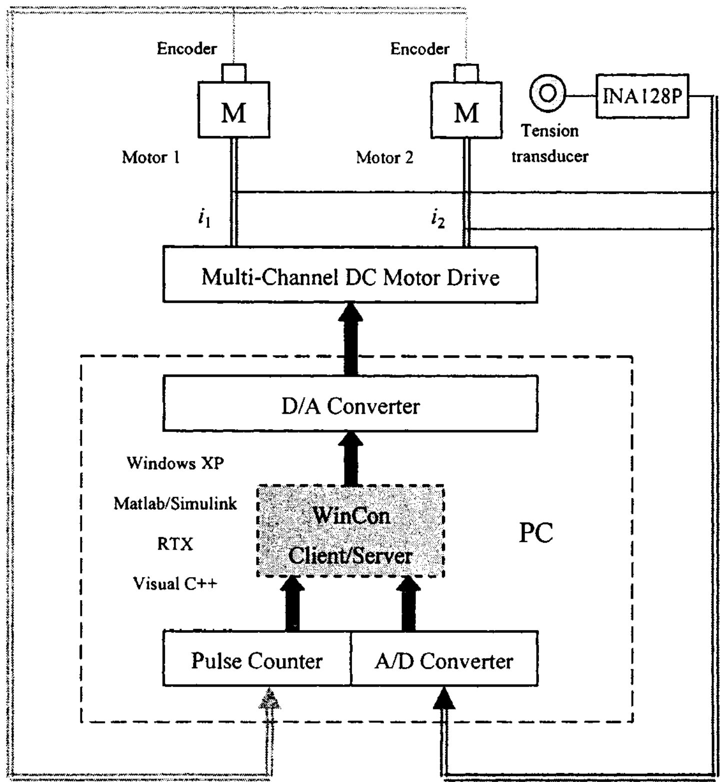

Figure 2.35 Real time experiment configuration.

The output of the tension measurement device is an analog signal of 0 to 500mv, which is a little low in magnitude compared to the A/D converter input range (0 to 10v). Furthermore, noise corruption makes a measurement fluctuate ±0.5 Newton from its real value. Since the tension signal is wired out from two nodes of an electrical bridge, noise is added on each wire in a common mode. A differential-mode amplifier (INA128P) is thus adopted to amplify the tension feedback signal and to reject the common mode noise. The effect is illustrated by a static tension signal (when there is no web motion) in **Figure 2.36**.

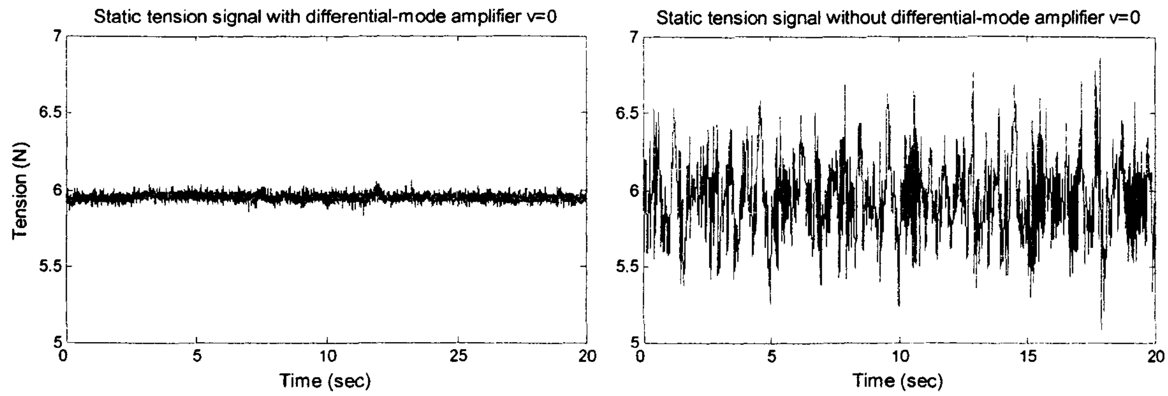

Figure 2.36 The effect of differential-mode amplifier.

H_∞ controller, LQR controller, and PI controller are implemented and validated on the experimental setup. All controllers are tested under the identical experimental configuration, including the same sampling time and tension/speed signal processing. **Figure 2.37** to **Figure 2.39** illustrate the control response of these three controllers, respectively. It can be observed that the experimental results match the analysis conclusions from the simulation results. For a 6*N* tension set point (with a speed rise from $0.1\ m/s$ to $0.2\ m/s$), for example, the maximum tension variation ($\Delta T/T$) is 6.01% with the proposed H_∞ controller, 9.13% with the LQR, and 23.07% with the distributed PI control. For a $0.1\ m/s$ speed set point (with a tension rise from 4*N* to 6*N*), on the other hand, the maximum speed variation ($\Delta v/v$) is 13.60%, 35.28% and 29.55%, respectively, with the H_∞, LQR and PI controllers. It is clear that the proposed robust H_∞ controller can attenuate the interaction between tension and line speed more effectively, and presents the best control performance among the three controllers.

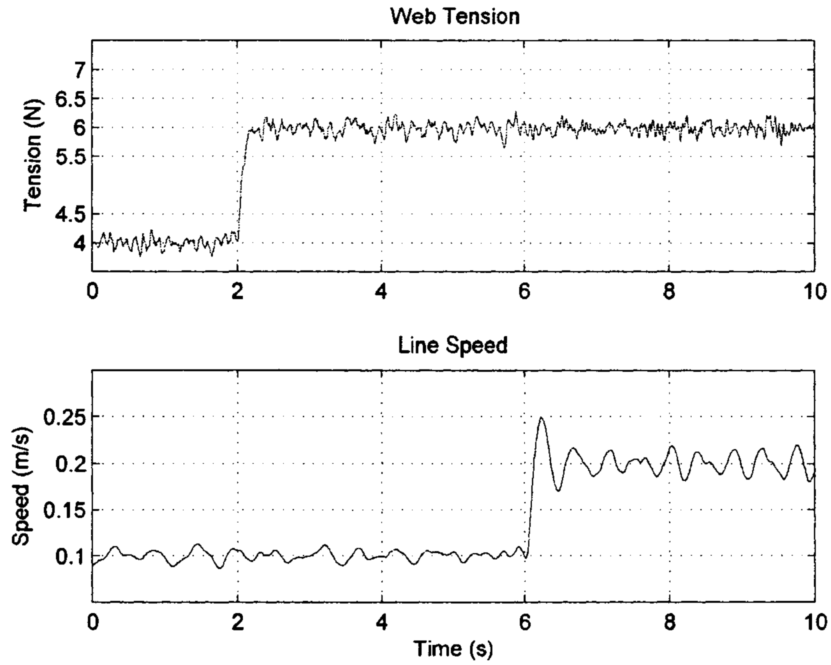

Figure 2.37 Experiment: H_∞ control.

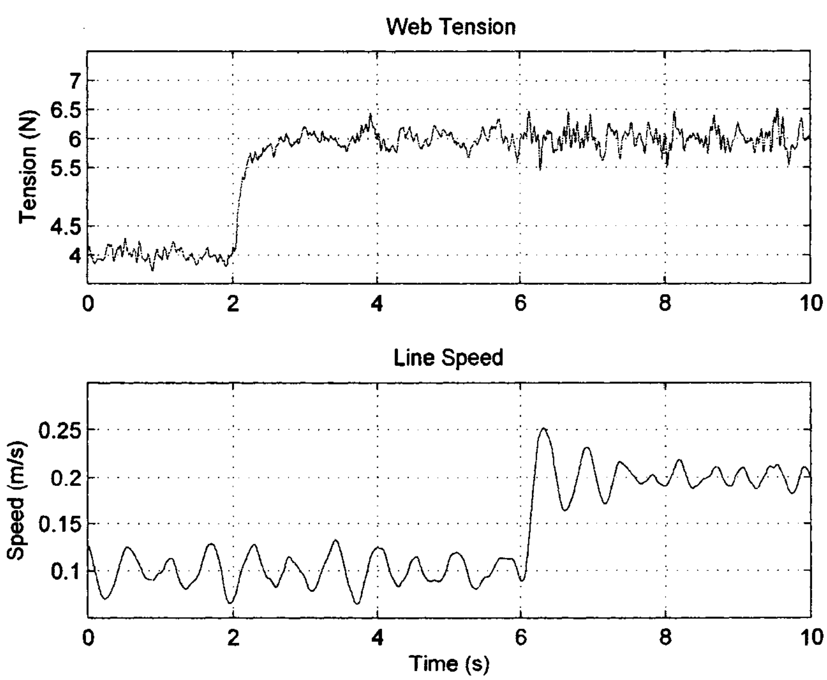

Figure 2.38 Experiment: LQR control.

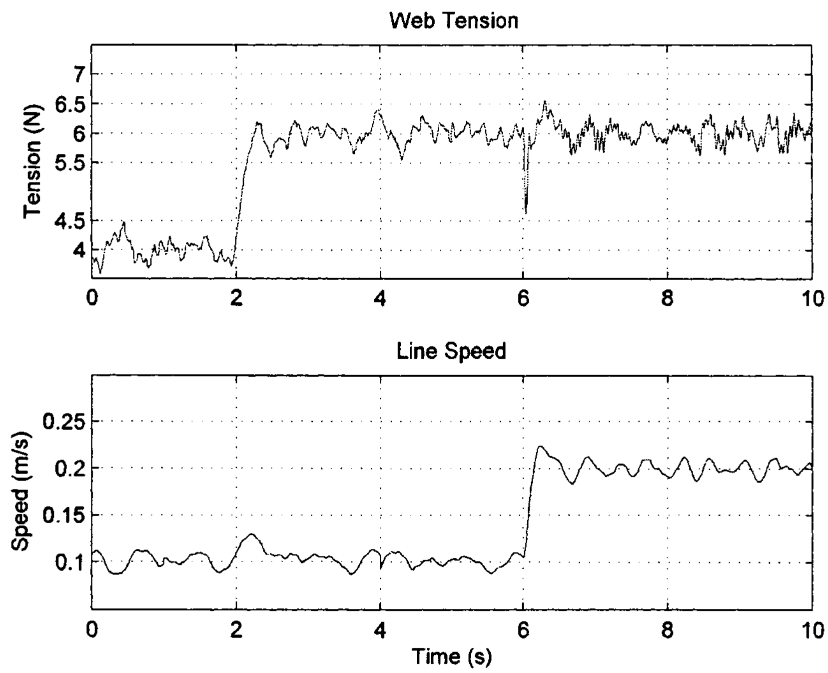

Figure 2.39 Experiment: PI control.

2.6 Conclusion

A robust H_∞ controller is proposed in this chapter for intermediate web span control applications. Bounded real parametric uncertainties are described and integrated into the sate-space representation of a typical intermediate web span. The investigation consists of a state-space oriented H_∞ control design and robustness property analysis. Of the two robustness analysis tools, singular value test is proved to be more conservative than μ-analysis especially for roust stability analysis, when structured model uncertainties are considered. The variations of different parameters have different impacts on system's robustness property. For a web system, the web length, cross-sectional area, and Young's modulus are found to have the most significant influence on robust stability of the closed-loop system. Furthermore, both simulation and experimental tests have demonstrated that compared with a LQR and a distributed PI control system, the proposed multivariable H_∞ control can be sued to attenuate web tension and speed fluctuations more effectively.

Chapter 3 **Winding Process Control**

A multi-stage web handling system usually includes an unwinding roll and a wingding roll as primitive elements for web material supply and accumulation. The operating characteristics of these elements can be studied by investigating a winding process. A pure wingding process is the web transportation process from an unwinding roll to a winding roll. Such reel-to-reel web winding systems are common in the manufactures, fabrication, and transport of many materials such as paper, metal, and photographic film. Advances in web winding system control might benefit these industries in a number of ways, such as increasing transient performance or reliability, and facilitating tighter tracking of the desired velocity and tension.

3.1 System Modeling

3.1.1 Nominal Plant Modeling

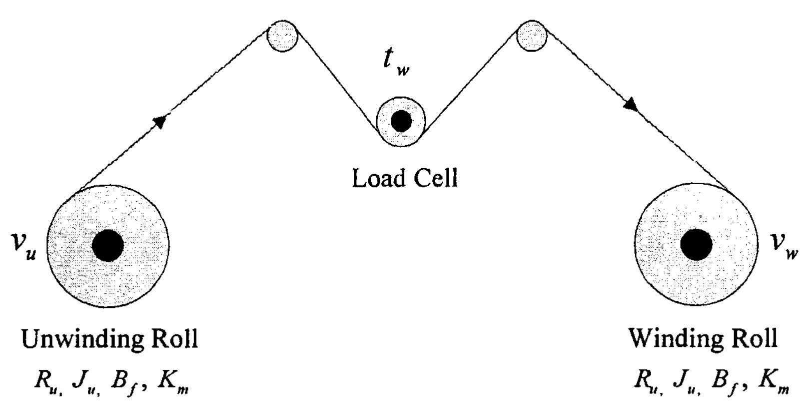

Figure 3.1 A Winding process.

A winding (or winding/unwinding) process model is shown in **Figure 3.1.** The driving motors of winding and unwinding rolls are assumed to have identical specifications. Neglecting dynamics of the load cell and idler rolls and with the assumptions on a web system described in **Chapter 2**, following time-invariant equations can be obtained to describe the dynamics of a winding process [24].

$$L\dot{t}_w = -v_w t_w + v_u t_{wo} - aEv_u + aEv_w; \tag{3.1}$$

$$\frac{d}{dt}(J_u \frac{v_u}{R_u}) = R_u t_w - B_f \frac{v_u}{R_u} + K_m i_u; \tag{3.2}$$

$$\frac{d}{dt}(J_w \frac{v_w}{R_w}) = -R_w t_w - B_f \frac{v_w}{R_w} + K_m i_w. \tag{3.3}$$

where

t_w:	Web tension (*N*);
t_{wo}:	Wound-out tension of the unwinding roll (*N*);
v_u:	Tangential velocity at the periphery of the unwinding roll (*m/s*);
v_w:	Tangential velocity at the periphery of the winding roll (*m/s*);
i_u:	Input current to the driving motor of the unwinding roll (*A*);
i_w:	Input current to the driving motor of the winding roll (*A*);
L:	Web length between the winding and unwinding rolls (*m*);
B_f:	Coefficient of bearing viscous friction (*N·m·s/rad*).
K_m:	Toque constant of winding/unwinding motor (*N·m/A*).
R_u:	Radius of unwinding roll (*m*).
J_u:	Moment of inertia of unwinding roll ($kg \cdot m^2$).
R_w:	Radius of winding roll (*m*).
J_w:	Moment of inertia of winding roll ($kg \cdot m^2$).

t_{wo}, the wound-out tension, is an initial static tension within the web roll, which is generated by the previous winding process. It is assumed to be zero in this work for the sake of simplicity.

With the web material transmitted from the unwinding roll to winding roll, the roll radius and inertia vary with time. Assume that the winding and unwinding rolls have the same roll cores. The radius and inertia varying patterns can be described by following equations:

$$R_u^2 = R_{u0}^2 - \frac{h}{\pi}\int v_u(t)dt; \tag{3.4}$$

$$R_w^2 = R_{w0}^2 + \frac{h}{\pi}\int v_w(t)dt; \tag{3.5}$$

$$J_u = J_c + \frac{1}{2}\rho w\pi(R_u^4 - R_c^4); \tag{3.6}$$

$$J_w = J_c + \frac{1}{2}\rho w\pi(R_w^4 - R_c^4). \tag{3.7}$$

where

R_{u0}, R_{w0}: Initial radius of unwinding/winding roll (m);

R_c, J_c: Radius (m) and moment of inertia ($kg\cdot m^2$) of unwinding/winding roll core;

ρ, w, h: Density (kg/m^3), width and thickness (m) of the web material.

Correspondingly we have

$$\dot{R}_u = -\frac{hv_u}{2\pi R_u}; \tag{3.8}$$

$$\dot{R}_w = \frac{hv_w}{2\pi R_w}; \tag{3.9}$$

$$\dot{J}_u = -\rho whv_u R_u^2; \tag{3.10}$$

$$\dot{J}_w = \rho whv_w R_w^2. \tag{3.11}$$

Substituting equations (3.8) through (3.11) into (3.2) and (3.3), it gives

$$\dot{v}_u = \frac{R_u^2}{J_u} t_w - \frac{B_f}{J_u} v_u + \frac{R_u K_m}{J_u} i_u + h\left[\frac{\rho w R_u^2}{J_u} - \frac{1}{2\pi R_u^2}\right] v_u^2 ; \tag{3.12}$$

$$\dot{v}_w = -\frac{R_w^2}{J_w} t_w - \frac{B_f}{J_w} v_w + \frac{R_w K_m}{J_w} i_w - h\left[\frac{\rho w R_w^2}{J_u} - \frac{1}{2\pi R_w^2}\right] v_w^2 , \tag{3.13}$$

The last item in equation (3.12) and (3.13) indicates the nonlinearity due to the time varying radii and inertias. Since the web thickness h is usually very small (e.g. $7.62\times 10^{-5} m$ in this work), the last item can be omitted to make the expressions (3.12) and (3.13) linear. The final real time model representation becomes

$$\begin{cases} \dot{t}_w = -\dfrac{v_w}{L} t_w - \dfrac{aE}{L} v_u + \dfrac{aE}{L} v_w \\ \dot{v}_u = \dfrac{R_u^2}{J_u} t_w - \dfrac{B_f}{J_u} v_u + \dfrac{R_u}{J_u} K_m i_u \\ \dot{v}_w = -\dfrac{R_w^2}{J_w} t_w - \dfrac{B_f}{J_w} v_w + \dfrac{R_w}{J_w} K_m i_w \end{cases} . \tag{3.14}$$

A further linearization by applying Taylor series yields

$$\dot{T}_w = -\frac{v_{w0}}{L} T_w - \frac{aE}{L} V_u + \frac{aE - t_{w0}}{L} V_w ; \tag{3.15}$$

$$\dot{V}_u = \frac{R_u^2}{J_u} T_w - \frac{B_f}{J_u} V_u + \frac{R_u}{J_u} K_m I_u ; \tag{3.16}$$

$$\dot{V}_w = -\frac{R_w^2}{J_w} T_w - \frac{B_f}{J_w} V_w + \frac{R_w}{J_w} K_m I_w . \tag{3.17}$$

where

T_w, V_u, V_w, I_u, V_w:	Changes to corresponding variables from their operating values;
v_{w0}:	Steady-state operating tangential velocity of winding roll (m/s).
t_{w0}:	Steady-state operating web tension (N).

In equation (3.15), usually $aE \gg t_{w0}$, so the equation can be further approximated by (3.18), which can also be derived by omitting the upstream and downstream disturbances in equation (2.1).

$$\dot{T}_w = -\frac{v_{w0}}{L}T_w - \frac{aE}{L}V_u + \frac{aE}{L}V_w; \tag{3.18}$$

The state-space representation of the nominal winding process plant is

$$\begin{cases} \dot{x}_p = A_n x_p + B_n u \\ y = C_n x_p \end{cases}, \tag{3.19}$$

where the subscript *p* represents *plant*, *n* stands for *nominal* and

$$x_p = \begin{bmatrix} x_1 & x_2 & x_3 \end{bmatrix}^T = \begin{bmatrix} T_w & V_u & V_w \end{bmatrix}^T;$$

$$u = \begin{bmatrix} u_1 & u_2 \end{bmatrix}^T = \begin{bmatrix} I_u & I_w \end{bmatrix}^T;$$

$$y = \begin{bmatrix} y_1 & y_2 \end{bmatrix}^T = \begin{bmatrix} T_w & V \end{bmatrix}^T.$$

$$A_n = \begin{bmatrix} -\frac{v_{w0}}{L} & -\frac{aE}{L} & \frac{aE}{L} \\ \frac{R_u^2}{J_u} & -\frac{B_f}{J_u} & 0 \\ -\frac{R_w^2}{J_w} & 0 & -\frac{B_f}{J_w} \end{bmatrix}, \quad B_n = \begin{bmatrix} 0 & 0 \\ \frac{R_u K_m}{J_u} & 0 \\ 0 & \frac{R_w K_m}{J_w} \end{bmatrix}, \quad C_n = \begin{bmatrix} 1 & 0 & 0 \\ 0 & 0.5 & 0.5 \end{bmatrix}.$$

The matrix C_n is defined such that the output signal is the tension and the line speed of the moving web, the latter of which is calculated by $V = (V_u + V_w)/2$.

3.1.2 Plant Modeling with Uncertainty Description

The parametric uncertainties of the considered winding process model are specified as:

$$\tilde{E} = E(1+\delta_E\Delta_E), \quad \tilde{B}_f = B_f(1+\delta_B\Delta_B), \quad \tilde{R}_u = R_u(1+\delta_{Ru}\Delta_{Ru}), \quad \tilde{R}_w = R_w(1+\delta_{Rw}\Delta_{Rw}),$$

$$\tilde{J}_u = J_u(1+\delta_{Ju}\Delta_{Ju}), \quad \tilde{J}_w = J_w(1+\delta_{Jw}\Delta_{Jw}), \quad \tilde{v}_{w0} = v_{w0}(1+\delta_v\Delta_v).$$

For winding process, we will try to use robustness analysis of the closed-loop system to numerically illustrate the effects of the slowly time varying radii and inertias, when the plant is controlled by H_∞, LQR and PI controllers, respectively. In order to associate the time varying parameters with the parametric uncertainty description introduced in **Chapter 2**, the system is considered at the operating point when both unwinding roll and winding roll are dimensionally half loaded. Varying ranges of roll radii can then be specified by the following uncertainty factors:

$$\delta_{Ru} = 0.5\,;\ \delta_{Rw} = 0.5\,.$$

Correspondingly, according to equations (3.6) and (3.7), and applying the parameter values of the testing apparatus, varying patterns of roll inertias can be described as

$$\delta_{Ju} = 0.22\,;\ \delta_{Jw} = 0.22\,.$$

Another definition of half loaded rolls can be made in a sense of inertia, instead of radius. However, in this research, the one based on radius is adopted. It should also be noted that for a winding process, the following expressions are assumed to be always held according to the mass conservation principle:

$$\Delta_{Ru} = -\Delta_{Rw}\,;\ \Delta_{Ju} = -\Delta_{Jw}\,.$$

A similar procedure is adopted to describe the specified parametric uncertainties, as demonstrated in **Chapter 2**. The state-space representation of the winding process model with uncertainty description is given by

$$\begin{cases} \dot{x}_p = A_u x_p + B_{u0} u_\Delta + B_{u2} u \\ y_\Delta = C_{u0} x_p + D_{u00} u_\Delta + D_{u02} u\,, \\ y = C_{u1} x_p \end{cases} \tag{3.20}$$

where

$$A_u = A_n;\quad B_{u0} = \begin{bmatrix} 1_{1\times3} & 0_{1\times10} & \\ 0_{1\times3} & 1_{1\times5} & 0_{1\times5} \\ 0_{1\times8} & & 1_{1\times5} \end{bmatrix}_{3\times13};\quad B_{u2} = B_n;\quad C_{u1} = C_n$$

$$C_{u0}=\begin{bmatrix} -\frac{v_{20}\delta_v}{L} & 0 & 0 & \frac{2R_u^2\delta_{Ru}}{J_u} & \frac{R_u^2\delta_{Ru}^2}{J_u} & 0 & 0 & -\frac{R_u^2\delta_{Ju}}{J_u} & -\frac{2R_w^2\delta_{Rw}}{J_w} & -\frac{R_w^2\delta_{Rw}^2}{J_w} & 0 & 0 & \frac{R_w^2\delta_{Jw}}{J_w} \\ 0 & -\frac{aE}{L}\delta_E & 0 & 0 & 0 & -\frac{B_f\delta_B}{J_u} & 0 & \frac{B_f\delta_{Ju}}{J_u} & 0 & 0 & 0 & 0 & 0 \\ 0 & 0 & \frac{aE}{L}\delta_E & 0 & 0 & 0 & 0 & 0 & 0 & 0 & 0 & -\frac{B_f\delta_B}{J_w} & \frac{B_f\delta_{Jw}}{J_w} \end{bmatrix}^T;$$

$$D_{u00}=\begin{bmatrix} 0_{7\times13} & & \\ 0_{1\times3} & [-\delta_{Ju}]_{1\times5} & 0_{1\times5} \\ 0_{4\times13} & & \\ 0_{1\times8} & [-\delta_{Jw}]_{1\times5} & \end{bmatrix}_{13};$$

$$D_{u02}=\begin{bmatrix} 0_{2\times6} & \frac{R_uK\delta_{Ru}}{J_u} & -\frac{R_uK\delta_{Ju}}{J_u} & 0_{2\times3} & 0 & 0 \\ 0 & 0 & 0 & & \frac{R_wK\delta_{Rw}}{J_w} & -\frac{R_wK\delta_{Jw}}{J_w} \end{bmatrix}^T.$$

3.2 Derivation of the Standard LFT Framework

The practical connection of the closed-loop system with two weighting functions is illustrated in **Figure 3.2**. When the plant model $G(s)$ refers to its nominal representation in (3.19), $P(s)$ is denoted as the nominal interconnection system $N(s)$. The standard LFT framework compactly describing the closed-loop system is shown in **Figure 3.3**, where the exogenous input and output: $w=r=\begin{bmatrix}T_{wr} & V_r\end{bmatrix}^T$, and $z=\begin{bmatrix}\bar{e} & \bar{u}\end{bmatrix}^T$, respectively.

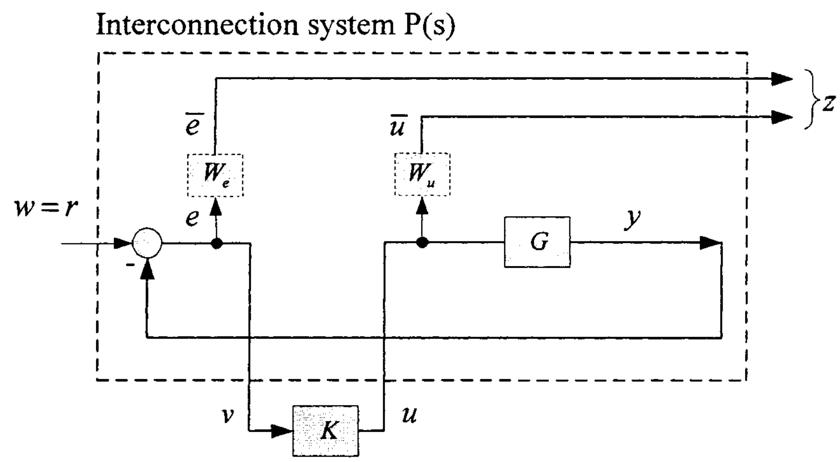

Figure 3.2 The closed-loop system with weighting functions.

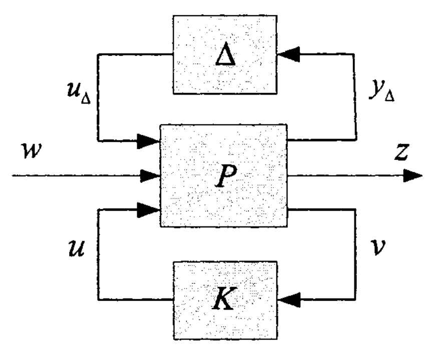

Figure 3.3 The standard LFT framework.

The derived state-space representation of the interconnection system $P(s)$ is

$$P(s)=\begin{bmatrix} P_{00}(s) & P_{01}(s) & P_{02}(s) \\ P_{10}(s) & P_{11}(s) & P_{12}(s) \\ P_{20}(s) & P_{21}(s) & P_{22}(s) \end{bmatrix}=\left[\begin{array}{c|ccc} A & B_0 & B_1 & B_2 \\ \hline C_0 & D_{00} & D_{01} & D_{02} \\ C_1 & D_{10} & D_{11} & D_{12} \\ C_2 & D_{20} & D_{21} & D_{22} \end{array}\right]; \tag{3.21}$$

and its nominal counterpart $N(s)$ is

$$N(s)=\begin{bmatrix} P_{11}(s) & P_{12}(s) \\ P_{21}(s) & P_{22}(s) \end{bmatrix}=\left[\begin{array}{c|cc} A & B_1 & B_2 \\ \hline C_1 & D_{11} & D_{12} \\ C_2 & D_{21} & D_{22} \end{array}\right], \tag{3.22}$$

where

$$A = \begin{bmatrix} A_{We} & 0_{2\times2} & -B_{We}C_{u1} \\ 0_{2\times2} & A_{Wu} & 0_{2\times3} \\ 0_{3\times4} & & A_u \end{bmatrix}_{7\times7}$$

$$B = \left[B_0 \;\vdots\; B_1 \;\vdots\; B_2\right] = \left[\begin{array}{c|c|c} \begin{bmatrix} 0_{4\times13} \\ B_{u0} \end{bmatrix} & \begin{bmatrix} B_{We} \\ 0_{5\times2} \end{bmatrix} & \begin{bmatrix} 0_{2\times2} \\ B_{Wu} \\ B_{u2} \end{bmatrix} \end{array}\right]$$

$$C = \begin{bmatrix} C_0 \\ \hline C_1 \\ \hline C_2 \end{bmatrix} = \left[\begin{array}{c} \begin{bmatrix} 0_{13\times}4 & C_{u0} \end{bmatrix} \\ \hline \begin{bmatrix} C_{We} & 0_{2\times2} & -D_{We}C_{u1} \\ 0_{2\times2} & C_{Wu} & 0_{2\times3} \end{bmatrix} \\ \hline \begin{bmatrix} 0_{2\times4} & -C_{u1} \end{bmatrix} \end{array}\right]$$

$$D = \left[\begin{array}{c|c|c} D_{00} & D_{01} & D_{02} \\ \hline D_{10} & D_{11} & D_{12} \\ \hline D_{20} & D_{21} & D_{22} \end{array}\right] = \left[\begin{array}{c|c|c} D_{u00} & 0_{13\times2} & D_{u02} \\ \hline 0_{4\times13} & \begin{bmatrix} D_{We} \\ 0_{2\times2} \end{bmatrix} & \begin{bmatrix} 0_{2\times2} \\ D_{Wu} \end{bmatrix} \\ \hline 0_{2\times13} & \begin{bmatrix} 1 & 0 \\ 0 & 1 \end{bmatrix} & 0_{2\times2} \end{array}\right]$$

Based on the similar considerations and procedure as illustrated in **Chapter 2**, the frequency weighting functions $W_e(s)$ and $W_u(s)$ are selected as

$$W_e(s) = \begin{bmatrix} \dfrac{0.5s+10}{s+0.01} & 0 \\ 0 & \dfrac{0.33s+10}{s+0.01} \end{bmatrix};$$

$$W_u(s) = \begin{bmatrix} \dfrac{0.2s+1}{s+10} & 0 \\ 0 & \dfrac{0.2s+1}{s+10} \end{bmatrix}.$$

3.3 Control Design

Initial ccontrollers are designed based on the basic linear and time invariant model in (3.19), in which both the winding and unwinding roll are considered dimensionally half loaded. One of the suboptimal H_∞ controllers is derived and represented by the following transfer functions:

$$K(s) = \begin{pmatrix} K_{11}(s) & K_{12}(s) \\ K_{21}(s) & K_{22}(s) \end{pmatrix},$$

where

$$K_{11}(s) = \frac{\text{-16.95s}^6\text{-1.012e4s}^5\text{-1.507e6s}^4\text{-3.703e8s}^3\text{-1.856e10s}^2\text{-2.524e11s-2.018e9}}{\text{s}^7\text{+1347s}^6\text{+8.186e5s}^5\text{+2.178e8 s}^4\text{+1.066e10s}^3\text{+1.428e11s}^2\text{+2.283e9s+9.128e6}};$$

$$K_{12}(s) = \frac{\text{411.6s}^5\text{+3.633e5s}^4\text{+1.744e8s}^3\text{+1.391e10s}^2\text{+3.903e11s+3.652e12}}{\text{s}^6\text{+1347s}^5\text{+8.186e5s}^4\text{+2.178e8s}^3\text{+1.066e10s}^2\text{+1.427e11s+1.141e9}};$$

$$K_{21}(s) = \frac{\text{16.95s}^6\text{+1.012e4s}^5\text{+1.507e6s}^4\text{+3.703e8s}^3\text{+1.856e10s}^2\text{+2.524e11s+2.018e9}}{\text{s}^7\text{+1347s}^6\text{+8.186e5s}^5\text{+2.178e8s}^4\text{+1.066e10s}^3\text{+1.428e11s}^2\text{+2.283e9s+9.128e6}};$$

$$K_{22}(s) = \frac{\text{411.6s}^5\text{+3.633e5s}^4\text{+1.744e8s}^3\text{+1.391e10s}^2\text{+3.903e11s+3.652e12}}{\text{s}^6\text{+1347s}^5\text{+8.186e5s}^4\text{+2.178e8s}^3\text{+1.066e10s}^2\text{+1.427e11s+1.141e9}}.$$

A similar procedure is used for the linear quadratic regulator design as in Chapter 2. The derived LQR feedback gain is

$$K = \begin{bmatrix} 2.2361 & -70.7107 & -0.0039 & 1.2405 & 0.0730 \\ -2.2361 & -70.7107 & 0.0039 & 0.0730 & 1.2405 \end{bmatrix}.$$

PI control for the winding process adopts a commonly used configuration in literature, which is different from the one for intermediate span control. The unwinding roll is under tension control instead of the winding roll, as shown in **Figure 3.4**. In this work, the proportional and integral gains, K_p and K_i, are tuned as:

Tension control loop: $K_p = 0.15$, $K_i = 3$;

Speed control loop: $K_p = 2$, $K_i = 15$.

The decentralized PI control can be represented by

$$K=\begin{bmatrix}\dfrac{0.15s+3}{s} & 0\\ 0 & \dfrac{2s+15}{s}\end{bmatrix}=\left[\begin{array}{cc|cc}0 & 0 & 2 & 0\\ 0 & 0 & 0 & 4\\ \hline 1.5 & 0 & 0.15 & 0\\ 0 & 3.75 & 0 & 2\end{array}\right].$$

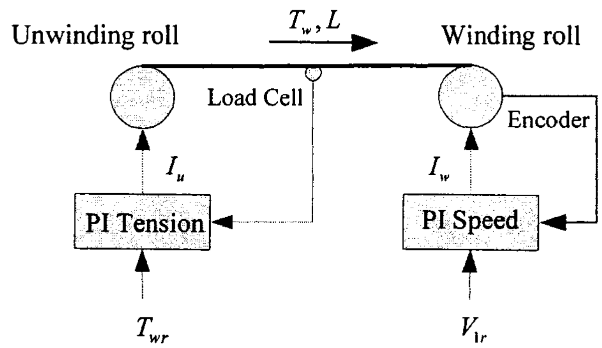

Figure 3.4 PI control of winding process.

3.4 Gain Scheduling

As stated previously, control system design for a winding process is conducted based on the basic linear and time invariant model, in which all parameters take their nominal values at the specified operating point. It would be intuitive to recognize that the time varying parameters-roll radius and inertia-will have their effects on control performance and robustness property of the corresponding closed-loop system. Such effects can be illustrated by Matlab simulation, as shown in **Figure 3.5**. H_∞ controller is used for this demonstration.

Within the design region, in which both winding and unwinding rolls are around dimensionally half loaded, the control performance achieves design requirements and the interaction between tension and speed can be attenuated effectively. However, at starting and ending stages, tension output becomes rather sensitive to speed changes, although the system remains stable and the steady-state error is small.

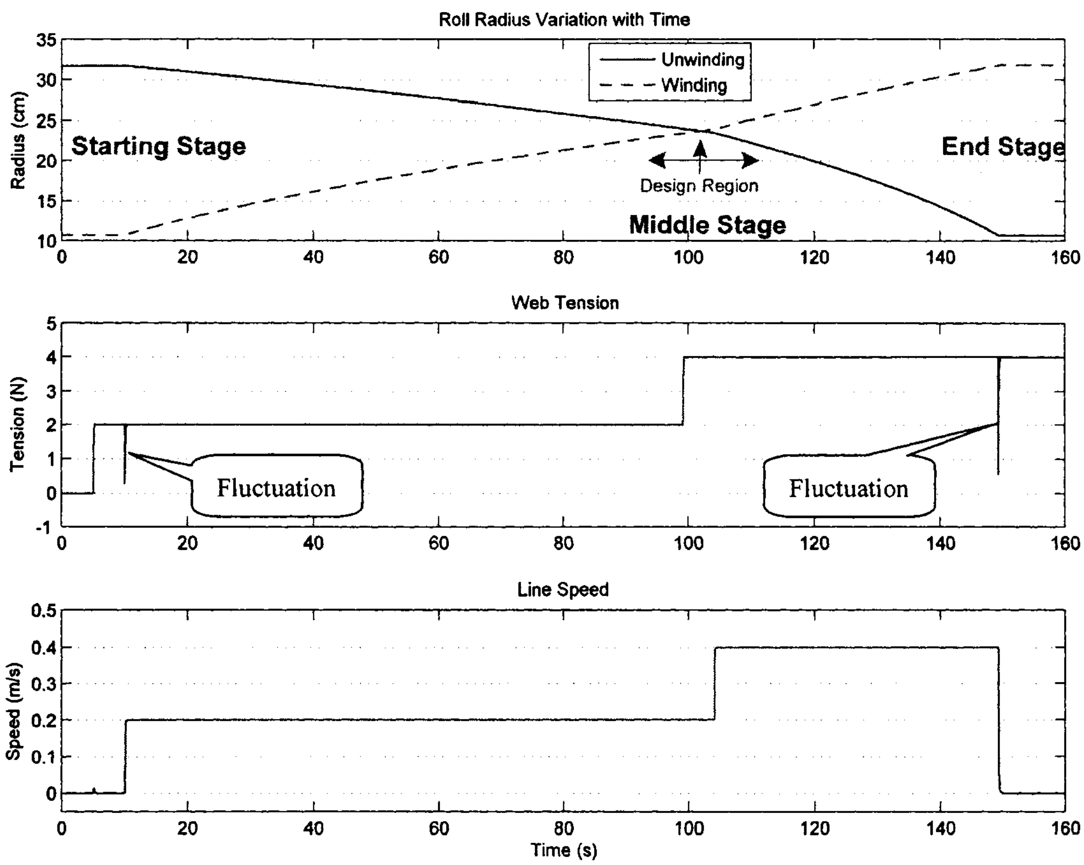

Figure 3.5 The effects of time varying radii on control performance.

There are very few papers in literature working on strategies to deal with the time varying parameters. It is generally assumed that the impact on control performance is not significant since the variation is slow, especially when the web roll is small. However, this assumption is arbitrary and lack of analytical support. As just observed in **Figure 3.5**, the robustness of tension output to speed changes does deteriorate significantly with radius/inertia changing. In this work, the necessity of gain scheduling will be determined by a quantifiable criterion, robust stability, which will be discussed in the following section.

A simple gain scheduling can be derived by dc gain analysis of the tension output. Since tension control is always the first priority in web system control and as we just observed from **Figure 3.5** that tension control deteriorates more than speed control with radius/inertia varying, more attention is paid to tension control gain scheduling.

Assume that unwinding roll radius and inertia are constants and there is no change in tangential velocity of the winding roll. Taking Laplace transform to equations (3.18) and (3.16), a transfer equation between tension change and winding motor current change can be derived as

$$\frac{T_w(s)}{I_u(s)} = \frac{EaR_uK_m}{J_uLs^2 + (LB_f + J_uv_{w0})s + B_fv_{w0} + EaR_u^2},$$

Assume that winding roll radius and inertia are constants and there is no change in tangential velocity of the unwinding roll. It gives similarly

$$\frac{T_w(s)}{I_w(s)} = \frac{EaR_wK_m}{J_wLs^2 + (LB_f + J_wv_{w0})s + B_fv_{w0} + EaR_w^2}.$$

Considering that $E >> 1$, and $EaR_u^2 >> B_fv_{w0}$ (e.g. the former is 2.59 while the latter is 3.2×10^{-3} in this work), B_fv_{w0} can be neglected from the denominator. It finally yields the dc component of the transfer function between tension change and unwinding/winding motor current change.

$$\lim_{s\to 0}\frac{T_w(s)}{I_u(s)} = \frac{EaR_uK_m}{B_fv_{w0} + EaR_u^2} \cong \frac{K_m}{R_u}; \tag{3.23}$$

$$\lim_{s\to 0}\frac{T_w(s)}{I_w(s)} = \frac{EaR_wK_m}{B_fv_{w0} + EaR_w^2} \cong \frac{K_m}{R_w}. \tag{3.24}$$

The dc gains are inversely proportional to the roll radii. A gain scheduling scheme is to adaptively compensate the error of control effort due to its dependence on radius variation. Considering all controllers are designed at the defined operating point, at which the radii take their initial values R_{u0} and R_{w0} and the control efforts should not be adjusted, a gain scheduling scheme is suggested as

$$\tilde{i}_u(t) = \frac{R_{u0}}{R_u} i_u(t); \tag{3.25}$$

$$\tilde{i}_w(t) = \frac{R_{w0}}{R_w} i_w(t). \tag{3.26}$$

where R_{u0} and R_{w0} are adopted for initial control design. They are used here to scale control signals out of the operating point. $\tilde{i}_u(t)$ and $\tilde{i}_w(t)$ are final control signals.

The validity of the above scheme is demonstrated by simulation test. A comparison can be made by observing **Figure 3.6**, which shows the control performance with the gain scheduling scheme applied.

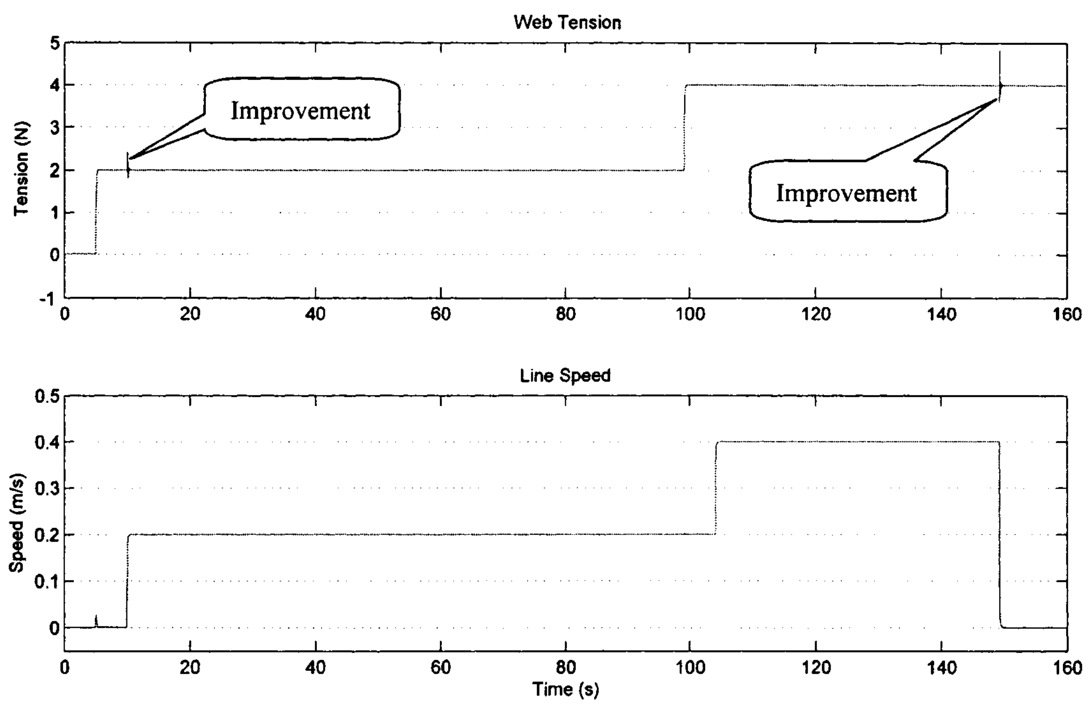

Figure 3.6 Control performance with gain scheduling.

The improvement due to gain scheduling is obvious at other operating stages (e.g. starting or end) outside of the control design region. Similar improvements can also be demonstrated by LQR or PI control (less obvious) based simulation.

3.5 Robustness Analysis

Three robustness properties, robust stability, nominal performance and robust performance, are also analyzed in this section for a winding process. The criteria are the same as the ones used in Chapter 2. The parametric uncertainties are specified by the following factors:

$\delta_{Ru} = 0.5$, $\delta_{Rw} = 0.5$, $\delta_{Ju} = 0.22$, $\delta_{Jw} = 0.22$, $\delta_{B} = 0.1$, $\delta_{v} = 0.1$; $\delta_{E} = 0.01$.

Table 3.1 shows the H_∞ norm test result of the corresponding closed-loop systems.

Table 3.1 H_∞ norms of the closed-loop systems with designed controllers.

	$\lVert M_{11} \rVert_\infty$	$\lVert M_{22} \rVert_\infty$	$\lVert F_u(M, \Delta) \rVert_\infty$
H_∞ Controller	11.9610	1.0218	15.8878
LQR	10.6040	1.4244	5.9114
PI Controller	7.2788	18.9103	12.1207

Alternatively, singular value and structured singular value plots can illustrate the robustness properties over frequencies. Since μ-analysis is less conservative than singular value test for structured uncertainties, only μ-analysis results are presented here. Nominal and robust performance tests of PI controller are not plotted together because the μ values are too large (around 20).

As illustrated by **Figure 3.7** to **Figure 3.9**, H_∞ Controller is the best in terms of nominal performance, which is almost achieved. Although LQR control reaches the best in robust performance analysis, no one controller could achieve robust performance. With the winding process model, none of the three controllers has the closed-loop system robustly stable. The time varying parameters, which have been defined as greatly varying uncertainties, have a significant impact on robust stability of the closed-loop system. One interesting phenomenon is that PI controller shows the best achievement in stability analysis. This matches a conclusion presented by some researches, such as in [26].

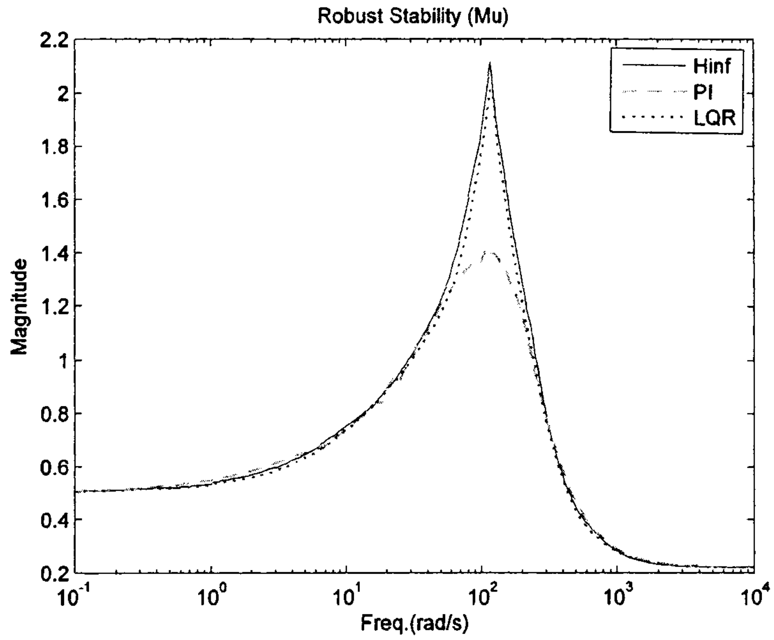

Figure 3.7 Robust stability analysis (H_∞, PI and LQR).

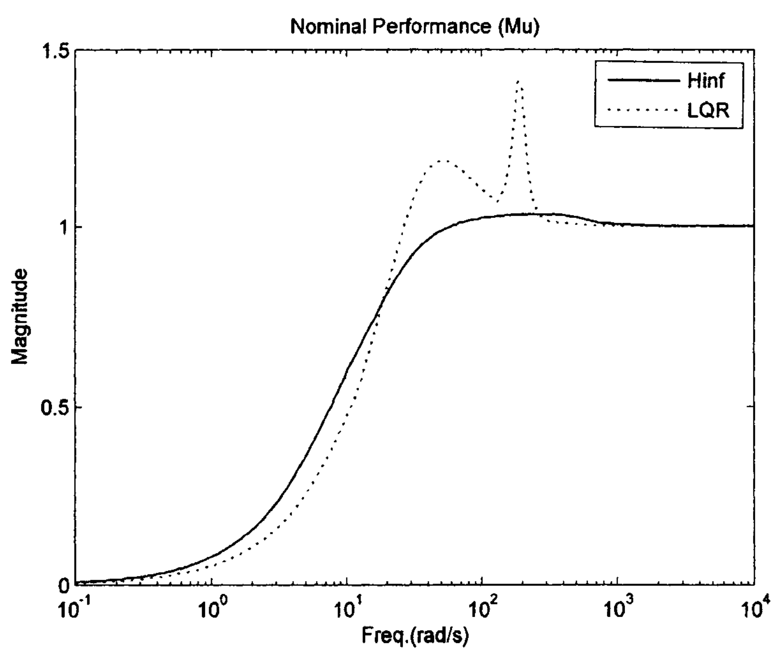

Figure 3.8 Nominal performance analysis (H_∞ and LQR).

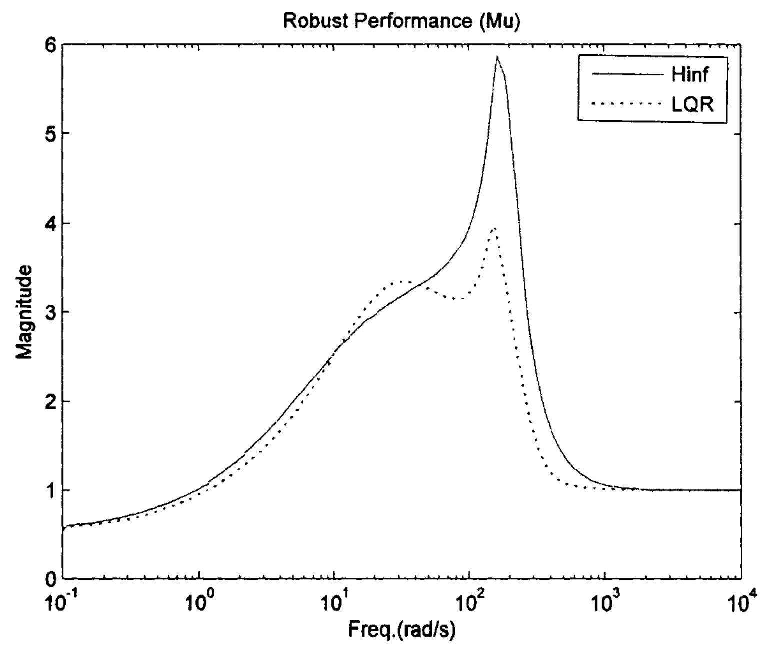

Figure 3.9 Robust performance analysis (H_∞ and LQR).

As we stated in the previous section, the necessity of a gain scheduling technique will be analyzed and determined based on robust stability analysis. The criterion is to have the closed-loop system achieve robust stability in a sense of μ-analysis test. The maximum radius varying range, within which the closed-loop system remains robustly stable, can also be derived for each controller. This analysis result is shown in **Table 3.2**. In the derivation, δ_{Ru}, δ_{Rw}, δ_{Ju}, and δ_{Jw} are gradually increased till robust stability is marginally achieved, and meanwhile, the uncertainty factors δ_B, δ_v and δ_E are specified 0.1.

Table 3.2 Maximum acceptable radius variations with different controllers

	δ_{Ru}, δ_{Rw}	δ_{Ju}, δ_{Jw}	**Maximum Radius Variation**
H_∞ Controller	0.27	0.088	**27%**
LQR	0.28	0.092	**28%**
PI Controller	0.39	0.149	**39%**

The result shows that the control system requires a gain scheduling in order to have the closed-loop system robustly stable over the whole winding process. PI controller presents the best capability in handling a large operating range, which also matches the robust stability analysis result in **Table 3.1**. However, more tests by simulation and experiments need to be conducted to make a comprehensive comparison among the three controllers, mainly in terms of control performance.

3.6 Evaluation and Comparison

3.6.1 Simulation Tests

Figure 3.10 shows the simulation setup for the overall winding/unwinding process, using H_∞ Control as an example. Fcn and Fcn1 in the diagram are gain scheduling functions. The subsystem block 'Nonlinear Model' describes the model represented by equations in (3.14). Time varying parameters are calculated according to equations (3.4) to (3.7). Step reference signals of tension and/or line speed occur at the starting, middle and end stage, respectively. Sinusoidal disturbances are applied to tension and line speed outputs to examine the disturbance rejection of a control strategy. Measurement noises are set to be white.

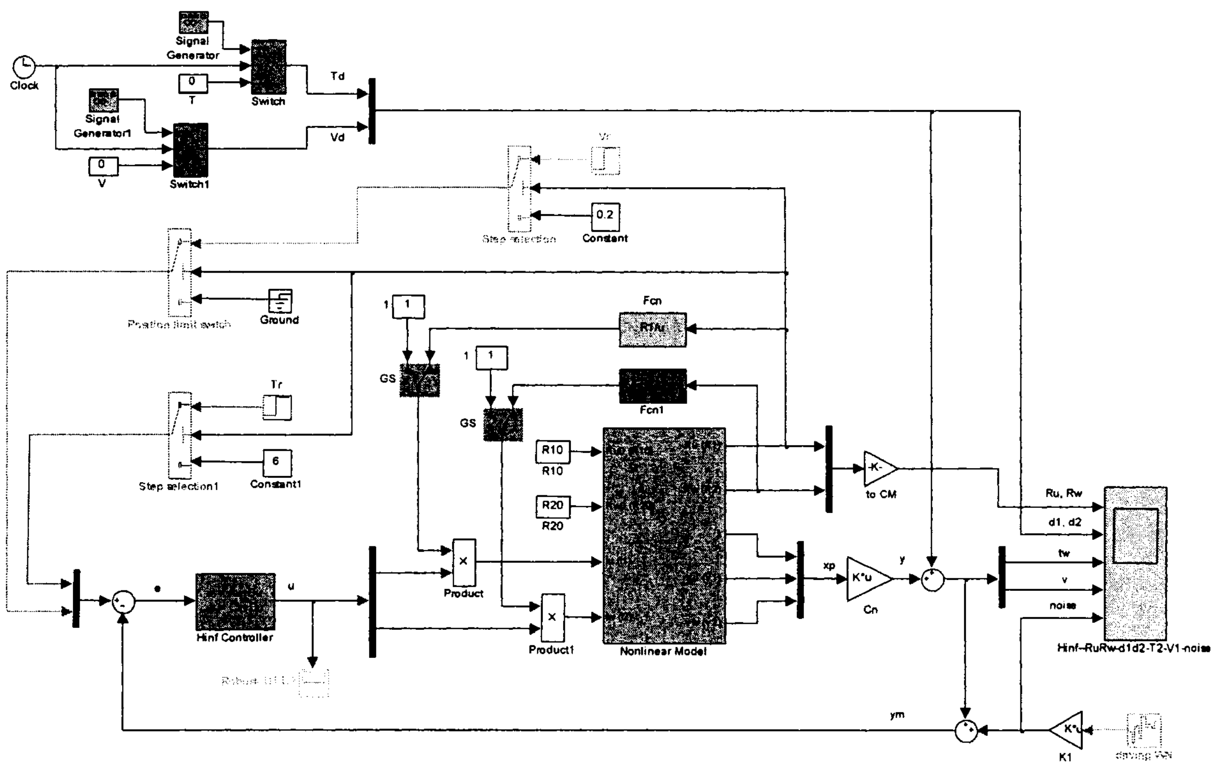

Figure 3.10 Simulation Configuration (H_∞).

All simulations are done with the previously described gain scheduling scheme. Simulation results are illustrated by the middle stage control of a winding process. The control performance is compared among the three controllers.

3.6.1.1 Nominal System Simulation Test

In this test, there is no any disturbance and measurement noise considered. All the parameters of the plant model are assigned to their nominal values at the operating point, except that the roll radius and inertia vary dynamically.

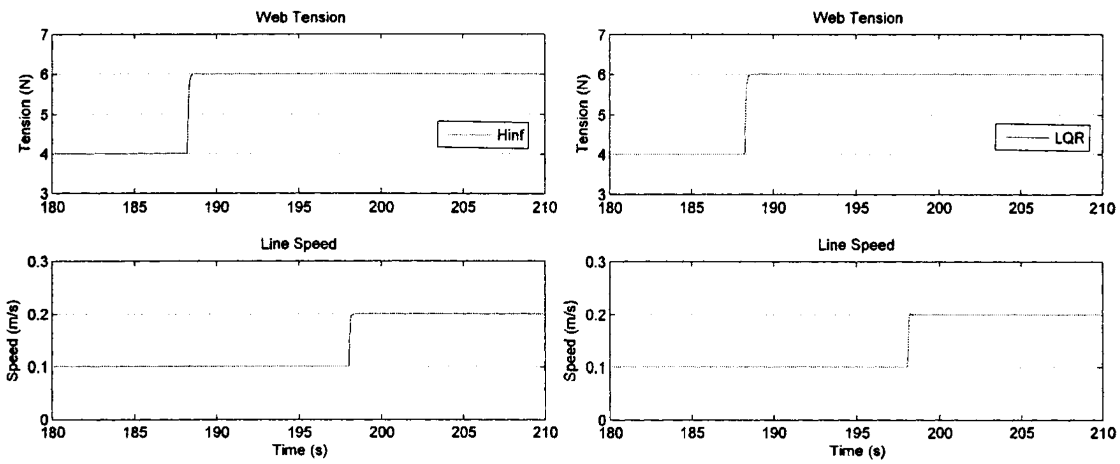

Figure 3.11 Simulation: H_∞ (left) and LQR (right) control, middle stage.

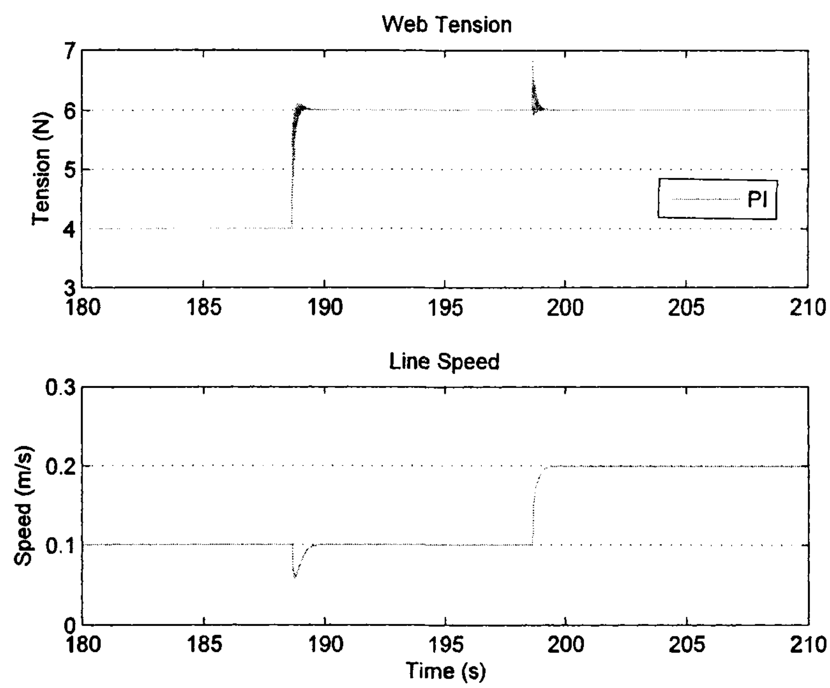

Figure 3.12 Simulation: PI control, middle stage.

The results illustrated in **Figure 3.11** and **Figure 3.12** show that H_∞ control has the best performance. LQR also presents good performance but with a small overshot on line speed response and tension fluctuates slightly with speed rising. Although PI controller is the best in robust stability test, its control performance is not as good as the two MIMO controllers. The interaction between speed and tension is not attenuated effectively by PI control. This demonstrates one of the advantages of MIMO control strategies when the plant is a MIMO system.

3.6.1.2 Simulation Test with Disturbance

This test is to examine the low frequency disturbance rejection of each controller. The tension disturbance is set to be a sinusoidal signal which is $1N$ in amplitude and $0.5Hz$ in frequency; the line speed disturbance is a sinusoidal signal with $0.05m/s$ amplitude and $0.5Hz$ frequency. **Figure 3.13** to **Figure 3.15** show the test results.

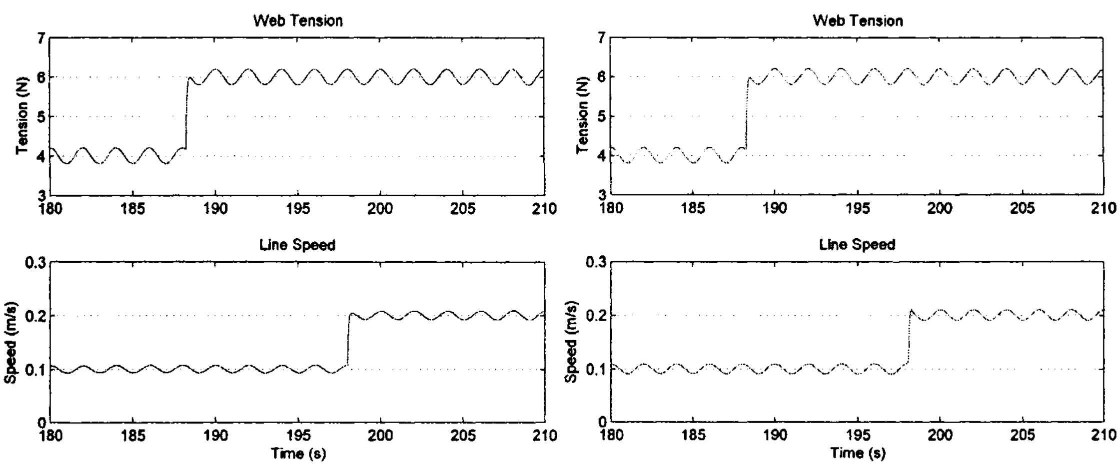

Figure 3.13 Simulation: H_∞ (left) and LQR (right) control with disturbance, middle stage.

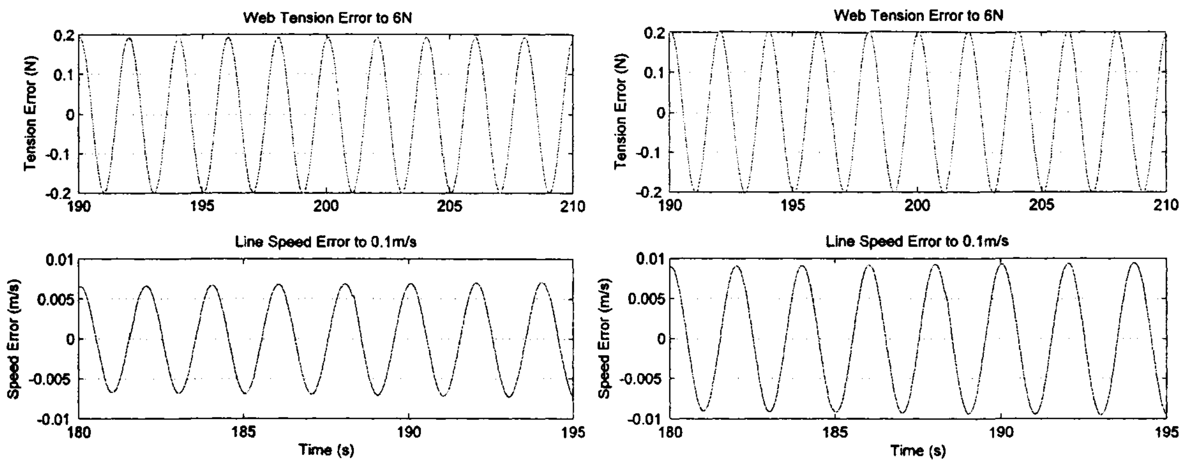

Figure 3.14 Simulation errors: H_∞ (left) and LQR (right) control with disturbance, middle stage.

Mean of Squared Errors (MSE): MSE (tension, H_∞) = 0.0193;
MSE (tension, LQR) = 0.0205;
MSE (speed, H_∞) = 2.4076e-005;
MSE (speed, LQR) = 4.2790e-005;

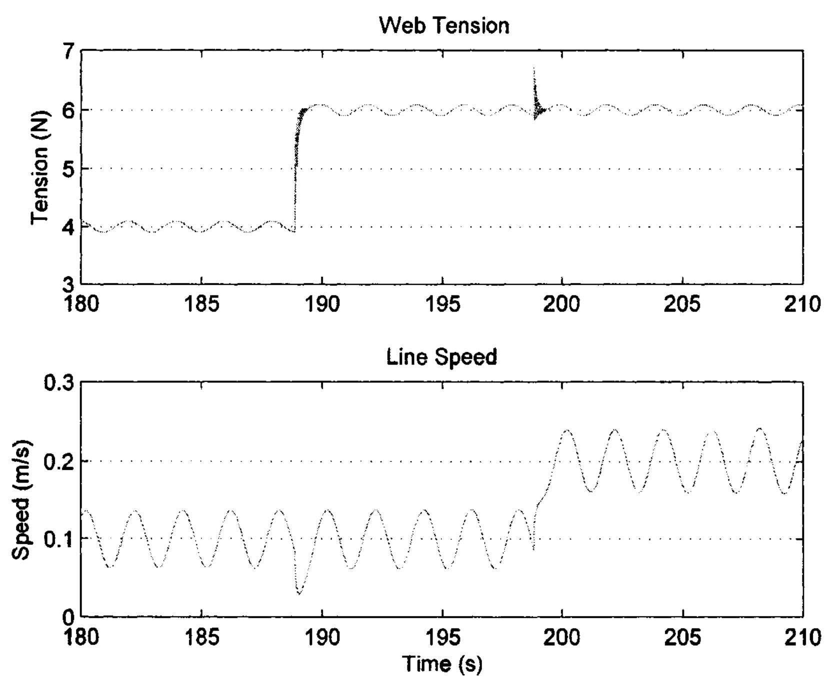

Figure 3.15 Simulation: PI control with disturbance, middle stage.

The results show that H_∞ and LQR control have similar low frequency disturbance rejection, except that the former is slightly better in speed control loop disturbance rejection. PI control has good performance in terms of tension disturbance rejection, but does not perform well with a line speed disturbance. Although the gains of tension loop PI and speed loop PI can be adjusted to have a better balance between tension and speed disturbance rejection, the control performance will then be affected correspondingly. The simulation results match the nominal performance tests in robustness analysis.

3.6.1.3 Simulation Test with Measurement Noise

The rejection capability to high frequency measurement noise is tested on each controller. The source is set to be zero-mean white noise, which is added to each measurement signal. From the following **Figure 3.17** to **Figure 3.19**, it can be observed that H_∞ control has the best rejection to web tension measurement noise. Although the speed loop in the PI control strategy performs not well in low frequency disturbance rejection, it is almost as good as the two MIMO control strategies in terms of measurement noise rejection. As it has been shown in **Chapter 2**, the PI tension control loop, on the other hand, is very sensitive to measurement noise.

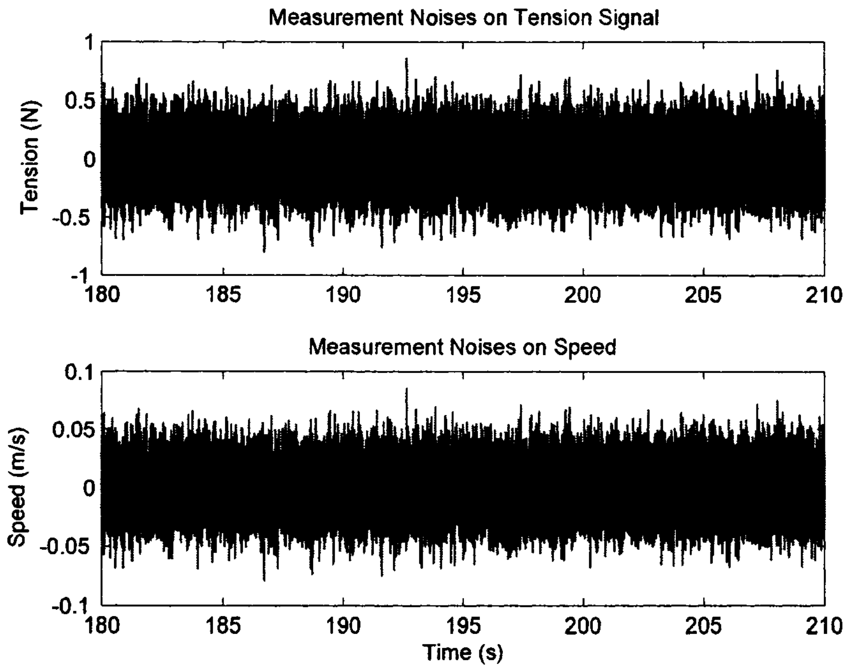

Figure 3.16 Simulation: Measurement noise.

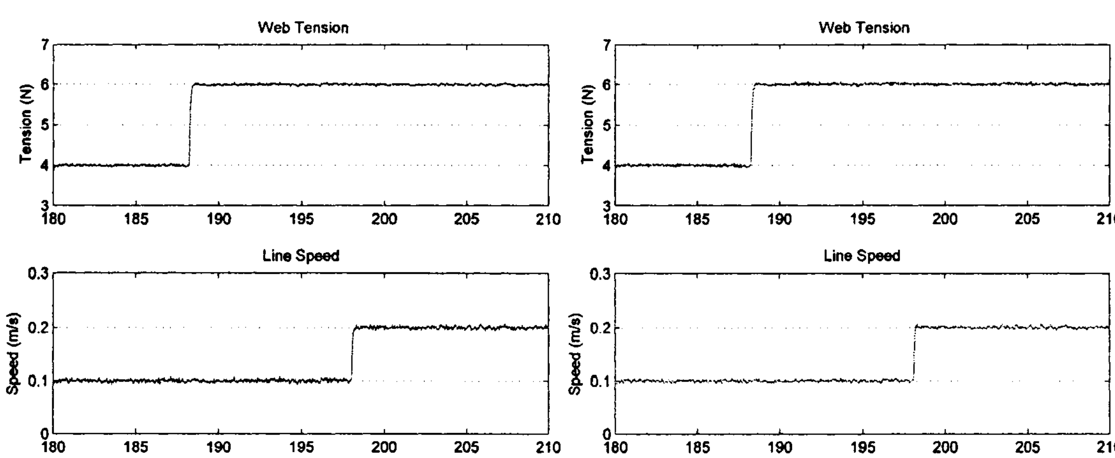

Figure 3.17 Simulation: H_∞ (left) and LQR (right) control with noise, middle stage.

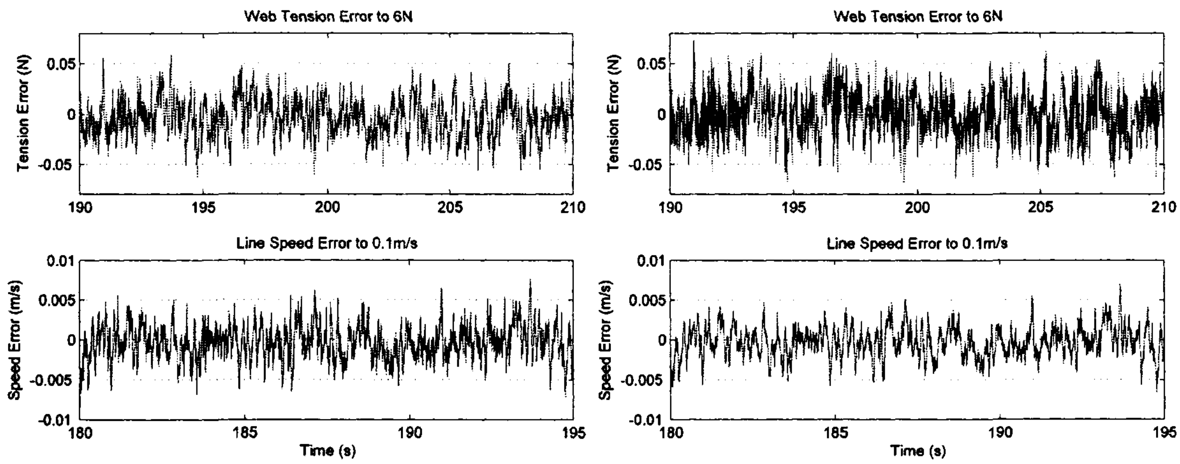

Figure 3.18 Simulation errors: H_∞ (left) and LQR (right) control with noise, middle stage.

Mean of Squared Errors (MSE): MSE (tension, H_∞) = 3.6487e-004;
MSE (tension, LQR) = 4.7331e-004;
MSE (speed, H_∞) = 5.0922e-006;
MSE (speed, LQR) = 3.9793e-006;

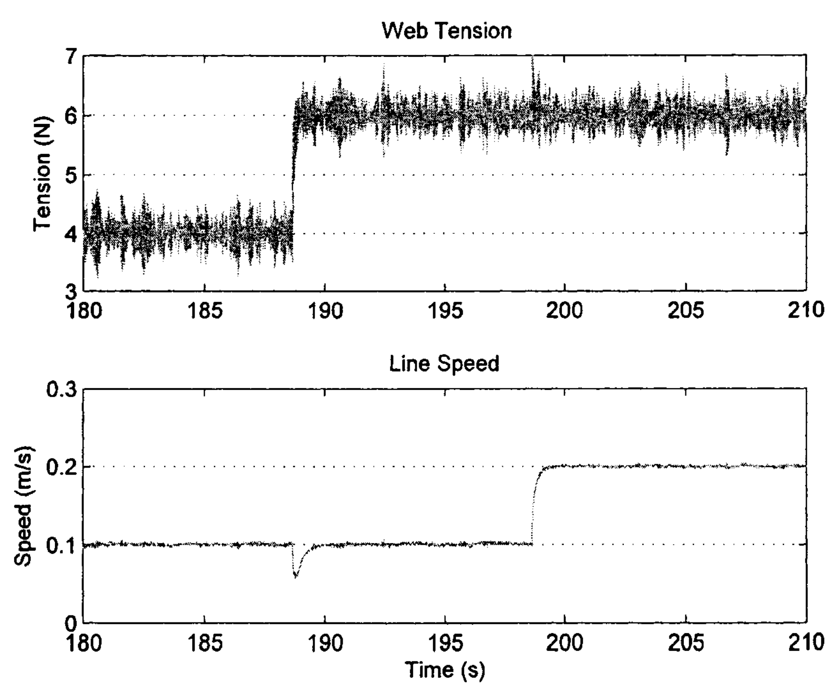

Figure 3.19 Simulation: PI control with noise, middle stage.

3.6.2 Experimental Tests

The experimental setup is shown in **Figure 3.20**. One of the two units is configured for the experiments.

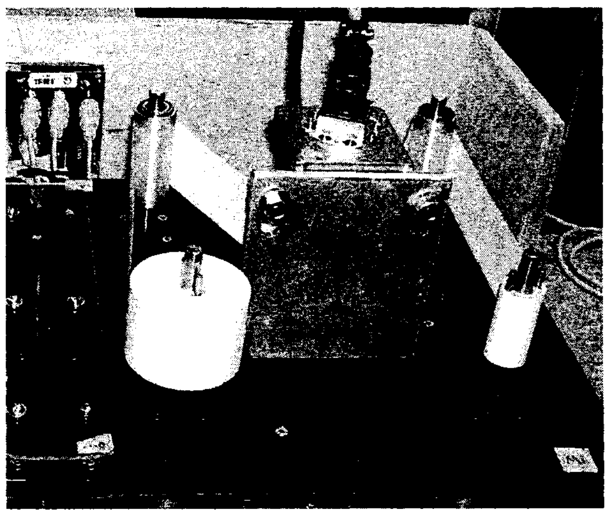

Figure 3.20 Winding process experimental setup.

The experiments are divided into two parts. Firstly, tests on the middle stage (control design region) of a winding process are conducted for each controller, to examine the control performance. Secondly, the effect of the gain scheduling scheme is verified by experiments at the starting stage of a winding process. Control performance with and without gain scheduling will be compared.

The radii of unwinding and wingding rolls can be calculated by the following equations:

$$R_u = R_{u0} - \frac{\theta_u}{2\pi} h, \tag{3.27}$$

$$R_w = R_{w0} + \frac{\theta_w}{2\pi} h, \tag{3.28}$$

where R_{u0} and R_{w0} denote the initial radius of unwinding and winding rolls, respectively. θ_u and θ_w are the integrated angular displacements of the rolls, and h is the web thickness. The initial radii have to be measured and determined before starting an experimental test. Angular displacements are detected by two encoders mounted on the driving shafts of unwinding and winding rolls.

3.6.2.1 Middle Stage Experimental Test

In this test, the winding roll and unwinding roll are operating in the control design region, in which both rolls are around dimensionally half loaded. The main comparison should be conducted between H_∞ control and LQR control. **Figure 3.21** shows the control performance of these two controllers.

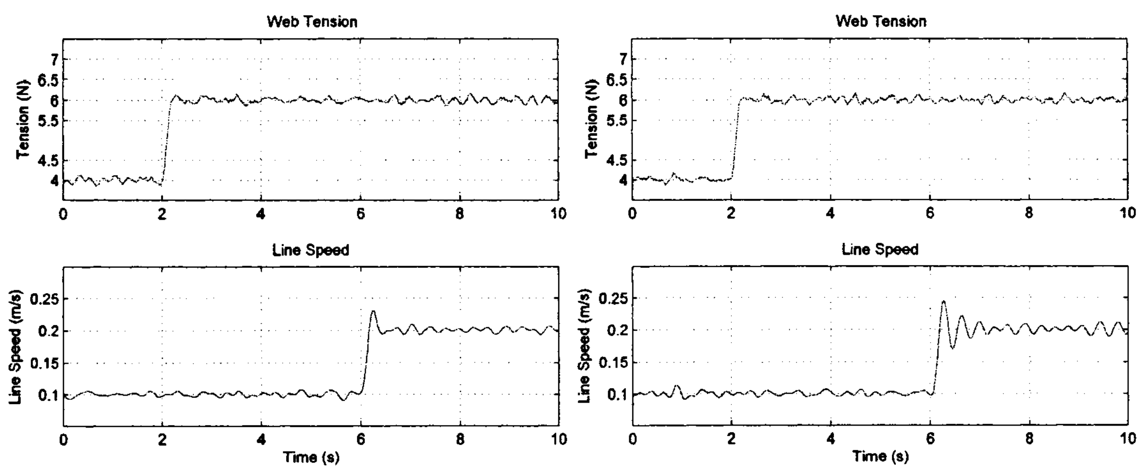

Figure 3.21 Experiment: H_∞ (left) and LQR (right) control, middle stage.

The tension control performance is similar between the two controllers. However, H_∞ control has a shorter settling time and smaller overshot than LQR in terms of line speed control. Furthermore, for a 6*N* tension set point (with a speed rise from $0.1\,m/s$ to $0.2\,m/s$), the maximum tension variation ($\Delta T/T$) is 2.69% with the proposed H_∞ controller, but 2.93% with the LQR. For a $0.1\ m/s$ speed set point (with a tension rise from 4*N* to 6*N*), on the other hand, the maximum speed variation ($\Delta v/v$) is 10% and 13.08%, respectively, with the H_∞ controller and LQR controller. These output errors are also illustrated by the error plots in **Figure 3.22**.

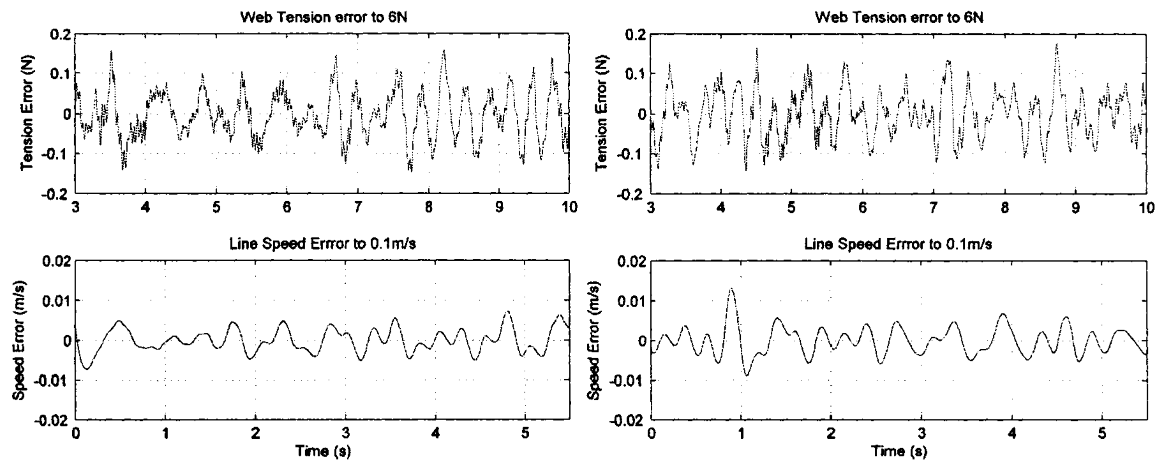

Figure 3.22 Experiment errors: H_∞ (left) and LQR (right) control, middle stage.

Mean of Squared Errors (MSE): MSE (tension, H_∞) = 0.0034;
MSE (tension, LQR) = 0.0036;
MSE (speed, H_∞) = 8.7282e-006;
MSE (speed, LQR) = 1.2620e-005;

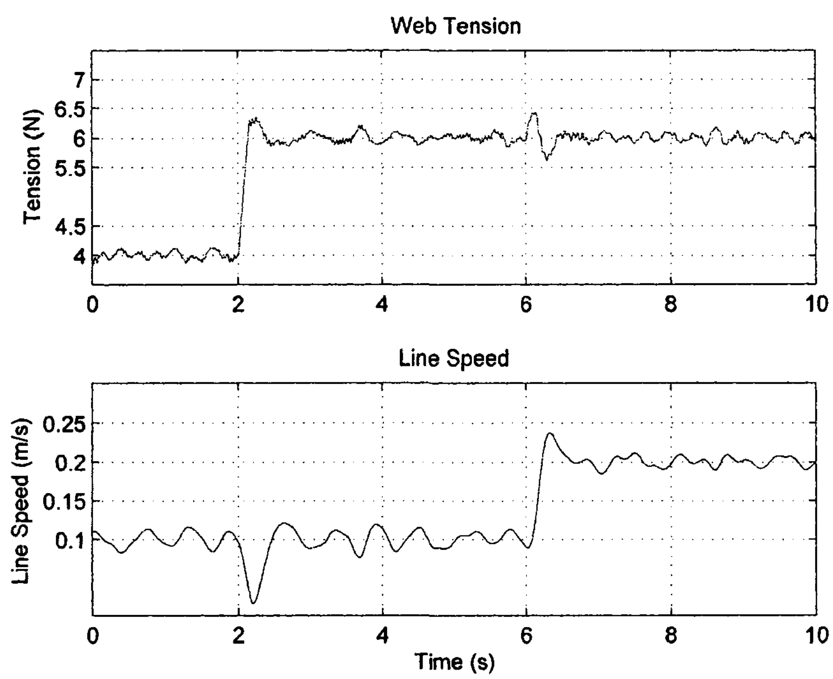

Figure 3.23 Experiment: PI control, middle stage.

PI control, which is implemented on the separate tension loop and speed loop, can not attenuate the interaction between tension and speed signals effectively, as shown in **Figure 3.23**. It should be noted that the interaction attenuation could be improved if feedforward compensation is applied to the tension and speed set points [4]. However, the effect of the compensation greatly relies on the accuracy of the mathematical model of the plant. In this demonstration, no such compensation loop is considered.

3.6.2.2 Starting Stage Experimental Test

In this test, the winding process is running from the starting point, at which the winding roll is unloaded and the unwinding roll is fully loaded. Only H_∞ control and LQR are used here for demonstration.

The performance improvement due to the gain scheduling scheme is clear from **Figure 3.24** and **Figure 3.25**.

- The tension fluctuation due to a line speed change is greatly suppressed, i.e. tension output becomes more robust to speed variations.
- The settling time is reduced, for both tension and speed responses.
- The overshot of speed response is decreased.

However, the speed fluctuation due to tension changes is not improved. It even becomes larger when the plant is controlled by LQR. This can also be detected by simulation. The reason is that the adopted gain scheduling scheme takes only the compensation to tension output into consideration, since tension control is the first priority in real-world applications. A more advanced adaptive technique could be a future work in dealing with the time varying parameters.

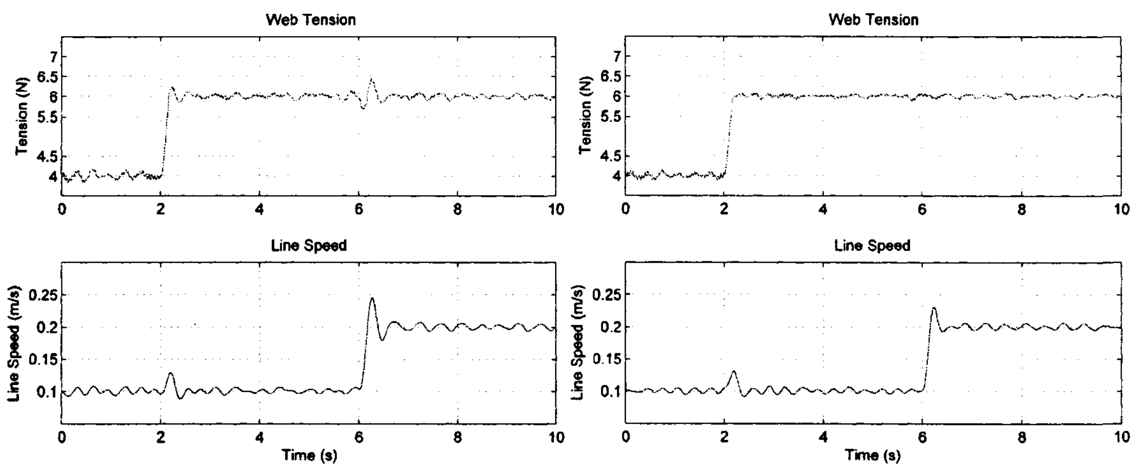

Figure 3.24 Experiment: H_∞ control, without (left) and with (right) gain scheduling, starting stage.

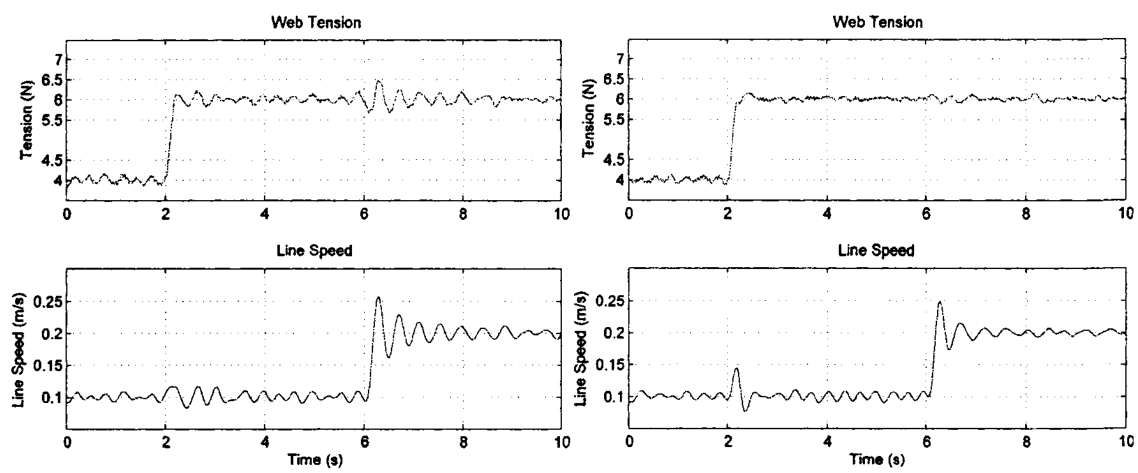

Figure 3.25 Experiment: LQR control, without (left) and with (right) gain scheduling, starting stage .

3.7 Conclusion

The three control strategies, H_∞, LQR and PI, which are discussed in intermediate web span control, are applied also to a winding process study in this chapter. As two MIMO control strategies, H_∞ and LQR are verified to be superior to the decentralized PI control in terms of interaction attenuation between web tension and line speed. However, the difference between H_∞ and LQR is not as obvious as in the intermediate span control. The former is just slightly better than the latter, considering only control performance. Robustness tests show that no controller achieves robust stability over the whole winding process. A dc gain analysis-based study provides a simple but efficient gain scheduling technique to deal with the time varying parameters of the plant. Verified by both simulation and experimental tests, the gain scheduling scheme improves the robustness of tension output to line speed variations at the operating stages out of the control design region.

Chapter 4 **Inactive Web Tension Control**

4.1 Introduction

The control techniques we discussed so far for intermediate web span and winding process are categorized into active web tension control. The actuators are roll (roller) driving motors, which are controlled to acquire both desired web speed and tension. Tension control is actually achieved through an active torque control of driving motors and is unavoidably coupled together with web speed control.

A distinct phenomenon in a multi-stage web system is called *tension transfer*. Consider again the following multi-span web system equations.

$$\dot{T}_i = -\frac{v_{i0}}{L_i}T_i - \frac{aE}{L_i}V_{i-1} + \frac{aE}{L_i}V_i + \frac{v_{(i-1)0}}{L_i}T_{i-1}, \tag{4.1}$$

$$\dot{V}_i = -\frac{R_i^2}{J_i}T_i - \frac{B_{fi}}{J_i}V_i + \frac{R_i^2}{J_i}T_{i+1} + \frac{R_i}{J_i}K_{mi}I_i. \tag{4.2}$$

From equation (4.1), a tension change in a certain web span (the *i*th) will affect the tension in the following span---the change is propagated backward. This behaviour is named *tension transfer*.

Also from equation (4.1), with an active control strategy, an upstream tension disturbance T_{i-1} can be compensated by a speed adjustment V_i of the *i*th driven roller (suppose $V_{i-1}=0$), so as to remain the desired tension set-point value of the *i*th web span, i.e. $T_i = 0$. However, this speed adjustment V_i tends to induce a tension fluctuation T_{i+1} in the following web span. It means another speed adjustment V_{i+1} needs to be generated by active control in the (*i*+1)th span to maintain its tension level. The result of this 'tension change-speed adjustment propagation' is that all the following spans have to go through a speed adjustment when tension varies in a certain web span. When a tension disturbance is large, the overall process speed change could be rather considerable. This is not allowed in an application where accurate speed control is required. The analysis indicates that active control strategy cannot eliminate tension transfer.

Besides active control, inactive (passive) method is an alternative for tension control and has been discussed in literature. In an inactive control strategy, the tension control actuator is no longer web driving motors. Dancer rolls and loopers are two common inactive tension control actuators. The mechanism of an inactive tension control is based on the relation between the tension variation and web length change of a web span. If in the *i*th web span, the web length is adjusted to control the tension and the length change $dL_i \ll L_i$, then

$$\dot{L}_i = dL_i / dt = V_i(t) - V_{i-1}(t)\,. \tag{4.3}$$

Substituting (4.3), equation (4.1) can be rewritten as

$$\dot{T}_i = -\frac{v_{i0}}{L_i} T_i + \frac{v_{(i-1)0}}{L_i} T_{i-1} + \frac{aE}{L_i} \dot{L}_i\,. \tag{4.4}$$

Paper [27] gives a comprehensive study on characteristics of active and passive dancers, and Pagilla etc. [28] has presented an application of active dancers to attenuate web tension disturbance. A dancer roll is illustrated in **Figure 1.6**.

According to if they are driven to actively move, dancer rolls are categorized into active dancers and passive dancers. Passive dancers are usually used to measure web tension in replacement of load cells [29]. If a dancer is driven to move back and forth so as to slightly change the web length, it can be used to adjust the web tension. One of the disadvantages of active dancer roll tension control is that the rotational motion of the actuator has to be converted to translational motion, which increases the complexity of the structure and needs more space for installation.

A looper, as shown in **Figure 4.1**, is commonly used in strip mills as a tension measurement device and a mass flow control actuator. The strategy there is to use looper height (or angle) as a tension feedback signal to achieve an active tension control, and to control the looper angle to maintain a desired upward pressure on the strip. Keeping the looper height (or angle) no change means the strip tension does not change [30] [31]. Although looper angle control also contributes to strip tension, the strategy by nature is still a type of active tension control because the main tension control actuators are strip driving motors.

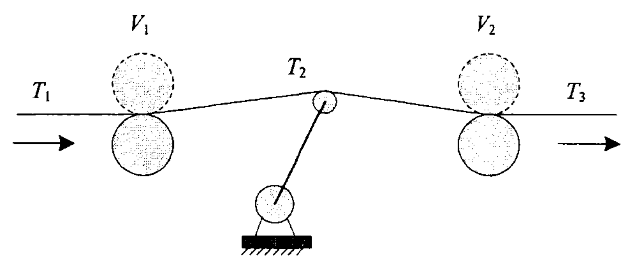

Figure 4.1 A looper structure.

In this work, a different way in utilizing loopers or looper-like structures is proposed. They will be adopted as actuators to attenuate tension fluctuations resulted from driven roller velocity variations or tension disturbances from adjacent web spans. Looper arm angle will be adjusted to have the tension follow a reference value. Tension change in a looper-controlled web span will not bring tension transfer to the following web spans, since no driven roller velocity has to be changed in order to achieve the tension control target.

4.2 System Modeling and Description

4.2.1 The Actuating Structure

Figure 4.2 shows the looper-like structure fabricated for the proposed inactive tension control. Transmission is conducted by a bevel gear pair and a worm shaft/gear pair. By using a worm gear box, firstly, large torque can be generated; and secondly, the arm angle can be held to maintain a tension level when without current input to the driving motor. The bevel gear ratio is 1:1, and the worm shaft/gear ratio is 60:1.

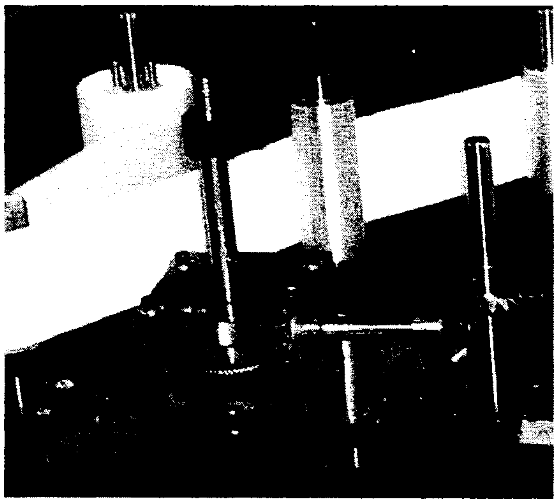

Figure 4.2 The fabricated actuator.

4.2.2 Structure Modeling

4.2.2.1 Nomenclature

t_w : Total web tension (N);

t_{w0} : Initial web tension at an operating point (N);

v_{10} : Initial tangential velocity of driven roller 1 (m/s);

v_{20} : Initial tangential velocity of driven roller 2 (m/s);

T_w : Tension change from an operating point value (N);

T_u : Tension disturbance from the upstream span (N);

L_0 : Initial total web length between two driven rollers at an operating point (m);

w : Web width (m);

h : Web thickness (m);

a : Cross-sectional area of the web material (m^2);

E : Young's modulus of the web material (GPa);

H_0 : Initial displacement of the contact point between looper roll and web (m);

θ : Looper angle (rad);

θ_0 : Initial looper angle at an operating point (rad);

L_a : Dimension between looper rotating origin and roller 1 (m);

L_b : Dimension between looper rotating origin and roller 2 (m);

R_a : Looper arm length (m);

R_r : Looper roll radius (m);

M_a : Looper arm mass (kg);

M_r : Looper roll mass (kg);

J_a : Looper arm inertia ($kg \cdot m^2$);

J_r : Looper roll inertia ($kg \cdot m^2$);

J_L : Mass moment of inertia of looper system ($kg \cdot m^2$);

B_f: Viscous friction coefficient of the structure transmission ($N \cdot m \cdot s/rad$);

$\theta_{\min}$: Minimum Looper angle (rad);

$\theta_{\max}$: Maximum Looper angle (rad);

K_m : Motor torque constant ($N \cdot m/A$);

γ : Total gear ratio.

4.2.2.2 Modeling Equations

The configuration of a looper tension control system is illustrated in **Figure 4.3**.

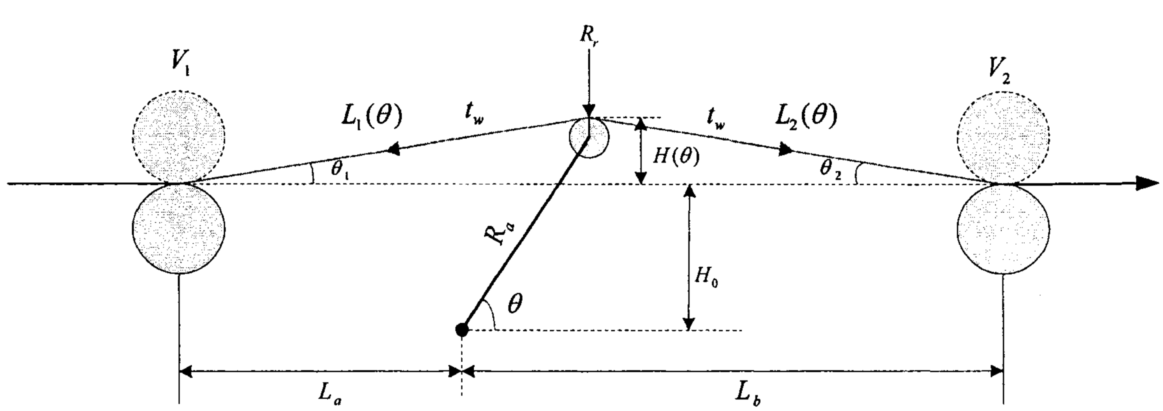

Figure 4.3 Looper system dimensions.

Assume there is no web slippage between any nipped driven rollers. The following equations are derived to describe the looper system:

$$t_w(\theta) = t_{w0} + T_w = t_{w0} + T_{w1} + T_{w2}; \tag{4.5}$$

$$T_{w1} = aE\frac{L(\theta) - L_0}{L_0}; \tag{4.6}$$

$$L(\theta) = L_1(\theta) + L_2(\theta) = \sqrt{H^2(\theta) + (L_a + R_a\cos\theta)^2} + \sqrt{H^2(\theta) + (L_b - R_a\cos\theta)^2}; \tag{4.7}$$

$$L_0 = L(\theta_0); \tag{4.8}$$

$$H(\theta) = R_a\sin(\theta) + R_r - H_0; \tag{4.9}$$

$$\dot{T}_{w2} = \frac{1}{L_0}\{-v_{20}T_{w2} + aE(V_2 - V_1) + v_{10}T_u\}; \tag{4.10}$$

Equation (4.10) describes the effects of two disturbances on web tension. One of the disturbances is from the variation of the velocity difference between the two driven rollers of the web span, (V_2-V_1); and the other one is from the tension variation in the upstream web span, T_u. Equations (4.7) to (4.9) describe the dimensional changes of the web length (L) and looper height (H) with looper angle varying.

An important issue is that the looper cannot be moved to any angle. The rotation should be restricted within a meaningful range. Looper angle constraints are defined as:

$$\theta_{max} = \frac{\pi}{2};$$

$$\theta_{min} = \sin^{-1}(\frac{H_0 - R_r}{R}), \quad \text{when } H(\theta)=0.$$

Next, a moment balance description shall be derived using Newton's second law. Due to the operating style of the testing apparatus and the mounting mode of the looper structure in this work, torques generated by weights of web material, looper arm and looper roll do not need to be considered.

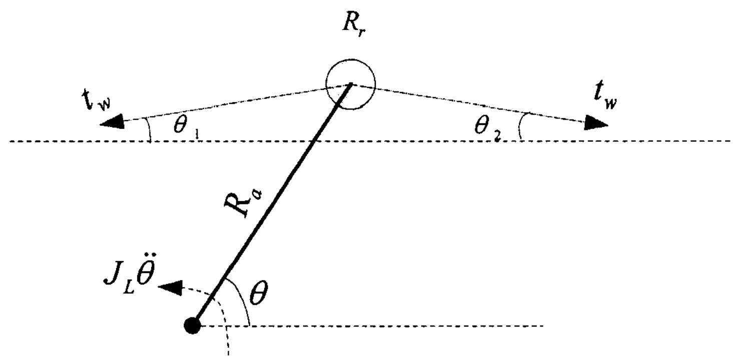

Figure 4.4 Free body diagram.

$$J_L\ddot{\theta} = \gamma\tau_m - \tau_t - \tau_f = \gamma K_m i_m - \tau_t - B_f\dot{\theta}; \tag{4.11}$$

$$J_L = J_r + J_a = \frac{1}{2}M_r R_r^2 + M_r R_a^2 + \frac{1}{3}M_a R_a^2, \tag{4.12}$$

where τ_m is the toque generated by the looper driving motor; τ_t is the toque generated by web tension; i_m is the current input of the driving motor.

The torque produced by web tension can be derived by analyzing the following diagram.

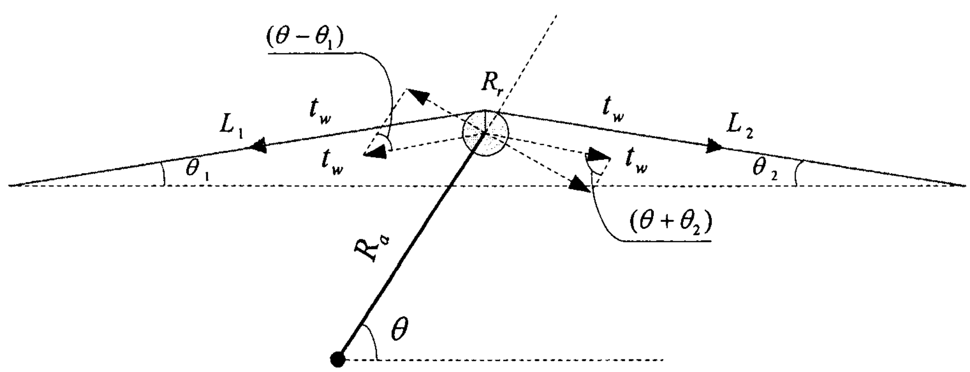

Figure 4.5 Derivation of web tension torque.

$$\begin{aligned}\tau_t &= t_w R_a \sin(\theta+\theta_2) - t_w R_a \sin(\theta-\theta_1)\\ &= t_w\{R_a[\sin(\theta+\theta_2) - \sin(\theta-\theta_1)]\} \; ;\\ &= t_w \Phi(\theta)\end{aligned} \tag{4.13}$$

$$\Phi(\theta) = R_a[\sin(\theta + \theta_2) - \sin(\theta - \theta_1)]; \tag{4.14}$$

$$\theta_1 = \tan^{-1}\frac{H(\theta)}{L_a + R_a\cos\theta}; \tag{4.15}$$

$$\theta_2 = \tan^{-1}\frac{H(\theta)}{L_b - R_a\cos\theta}. \tag{4.16}$$

4.2.2.3 Model Description of the Structure

From the above analysis, an overall description of the mathematical model can be

$$t_w(\theta) = t_{w0} + T_w = t_{w0} + T_{w1} + T_{w2}$$

$$T_{w1} = aE\frac{L(\theta) - L_0}{L_0}$$

$$\dot{T}_{w2} = \frac{1}{L_0}\{-v_{20}T_{w2} + aE(V_2 - V_1) + v_{10}T_u\}$$

$$J_L\ddot{\theta} = \gamma K_m i_m - \tau_t - B_f\dot{\theta}$$

$$\tau_t = t_w\Phi(\theta)$$

The mathematical model is highly nonlinear. A block diagram of the above structure model is given in **Figure 4.6**.

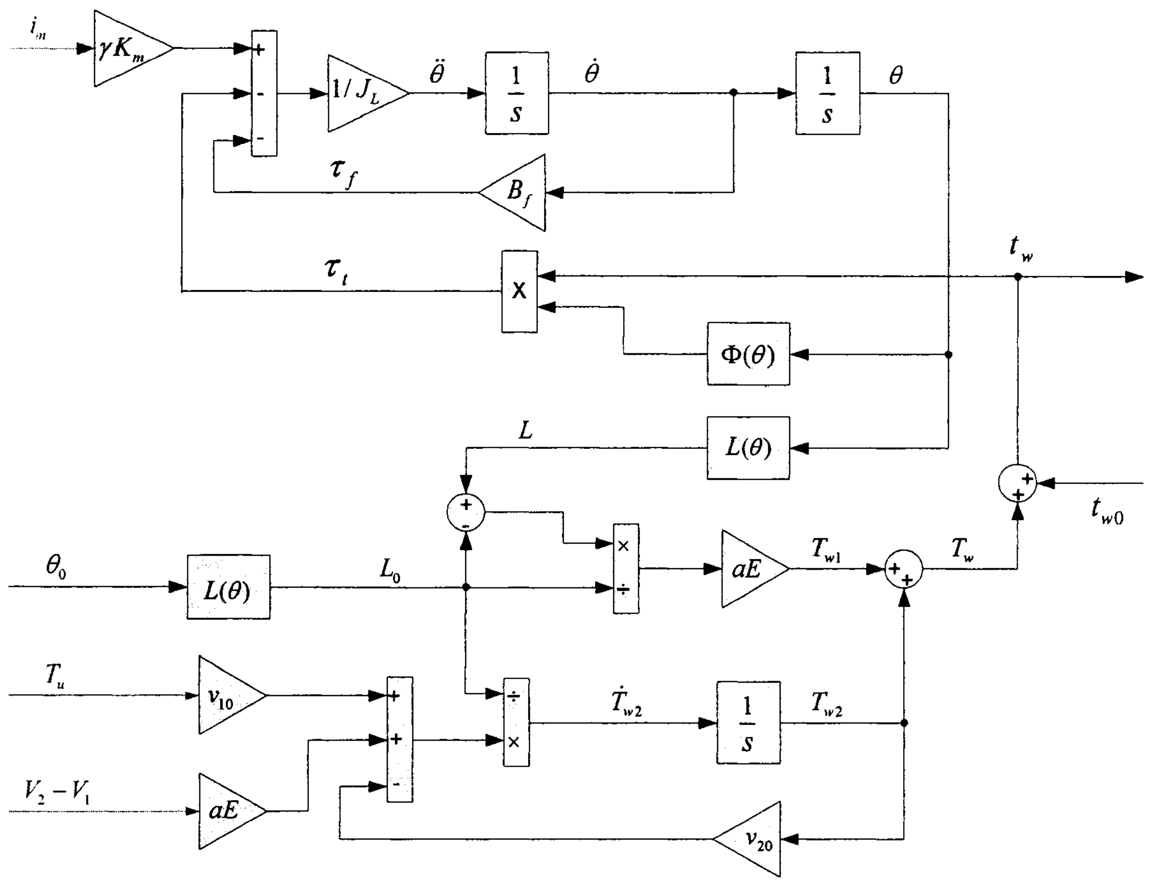

Figure 4.6 Block diagram of looper structure.

4.2.2.4 Looper in a Web Span with Idlers

There are usually idler rolls between the two end drive motors of a web span, for example, the one as shown in **Figure 4.7**.

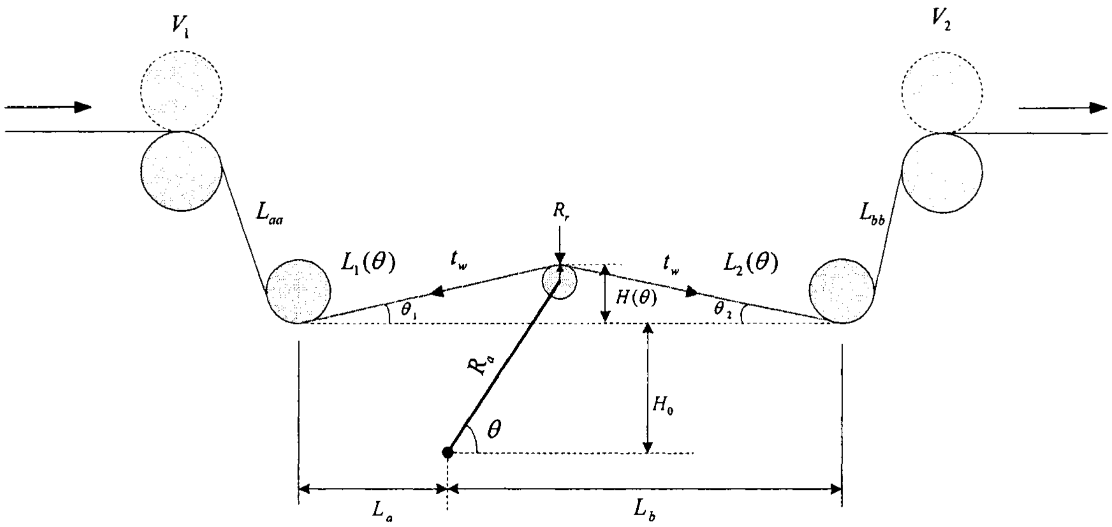

Figure 4.7 A web span with idler rolls.

For this type of web span, the model description can be derived by modifying the related equations, which are

$$\begin{aligned} L(\theta) &= L_{aa} + L_1(\theta) + L_2(\theta) + L_{bb} \\ &= L_{aa} + \sqrt{H^2(\theta) + (L_a + R_a\cos\theta)^2} + \sqrt{H^2(\theta) + (L_b - R_a\cos\theta)^2} + L_{bb} \end{aligned} \quad ; \qquad (4.17)$$

$$L_0 = L(\theta_0) = L_{aa} + L_1(\theta_0) + L_2(\theta_0) + L_{bb}\,. \qquad (4.18)$$

Then the previous mathematical model can be slightly modified considering the above two equations in order to describe the web span in **Figure 4.7**.

4.3 PID Control and Simulation

4.3.1 Simulation Setup

The mathematical model of an intermediate web span with the proposed looper actuator, as discussed in section **4.2.2**, is built in Matlab Simulink and shown in **Figure 4.8**. The block named 'worm gear position-hold' simulates the single transmission direction effect of a worm shaft/wheel pair.

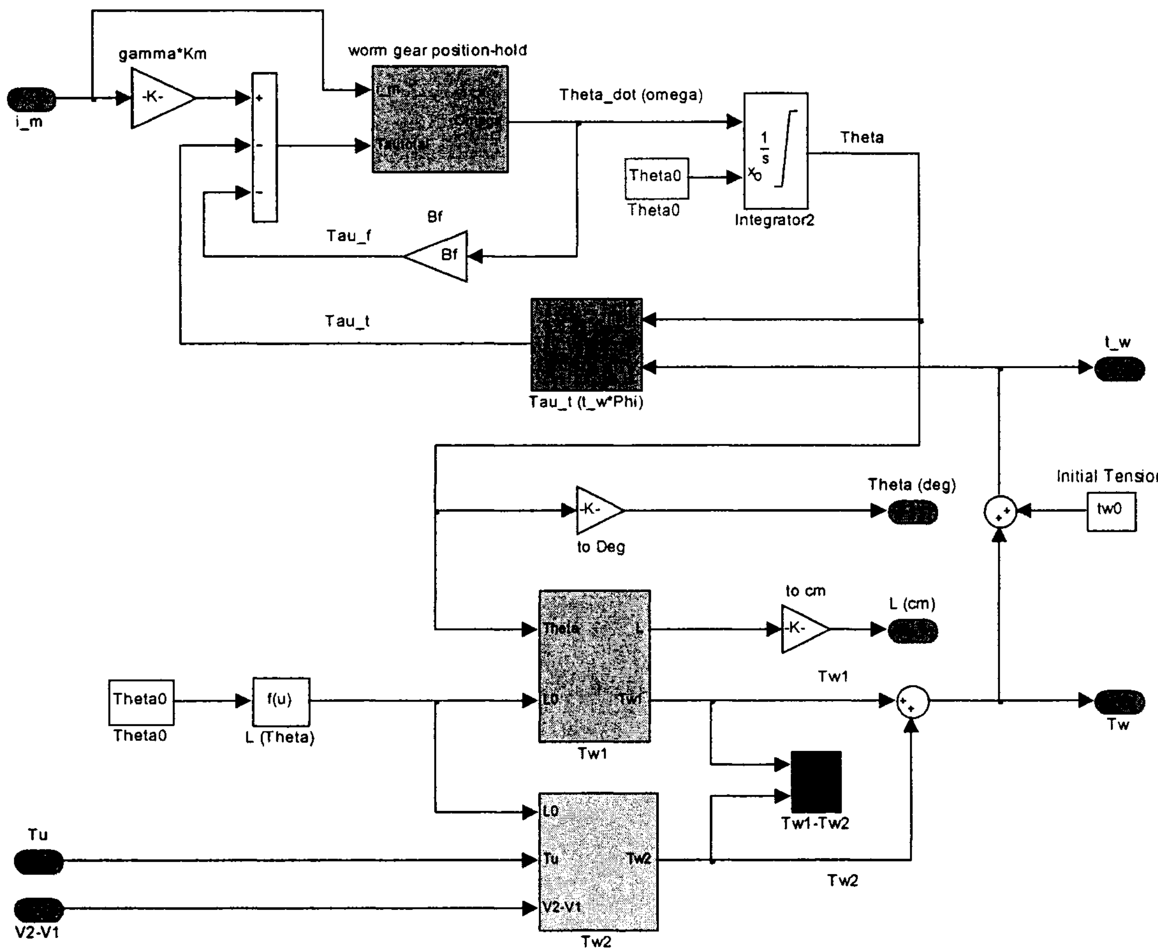

Figure 4.8 Plant block diagram in Simulink.

A PID controller is designed for the proposed inactive looper tension control. The gains are determined by trial and error method, finally with K_P=1.2; K_I=2.5; K_D=0.01. The simulation configuration diagram is illustrated in **Figure 4.9**. All the parameter values adopted in simulation are from the real actuator and testing apparatus used for experimental test. Some parameters are listed in **Table 4.1**.

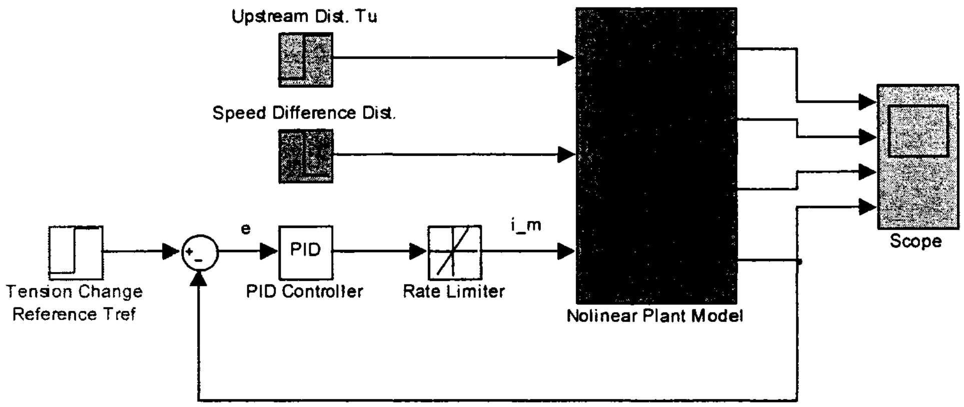

Figure 4.9 PID control simulation setup.

Table 4.1 Parameters of the simulation and experimental setup

L_a	51 mm	R_r	12.7 mm	θ_0	30 deg
L_b	200 mm	M_a	93.04 g	v_{10}	0.2 m/s
L_{aa}	180 mm	M_r	126.64 g	v_{20}	0.2 m/s
L_{bb}	675 mm	B_f	0.8 kg·m·s/rad	H_0	70 mm
R_a	123 mm	γ	180	t_{w0}	6 N

4.3.2 Simulation Test

The simulation is conducted on an intermediate web span which has an initial tension (it can be generated by speed difference control in real experiments). The tension signal is fed back to the control loop of the looper-like inactive actuator, instead of one of the driven rollers, as in the active control setup. **Figure 4.10** shows the step response of the closed-loop system when tension reference rises from $6N$ to $8N$. The change of looper arm angle and the slight change in the web length are also calculated and plotted.

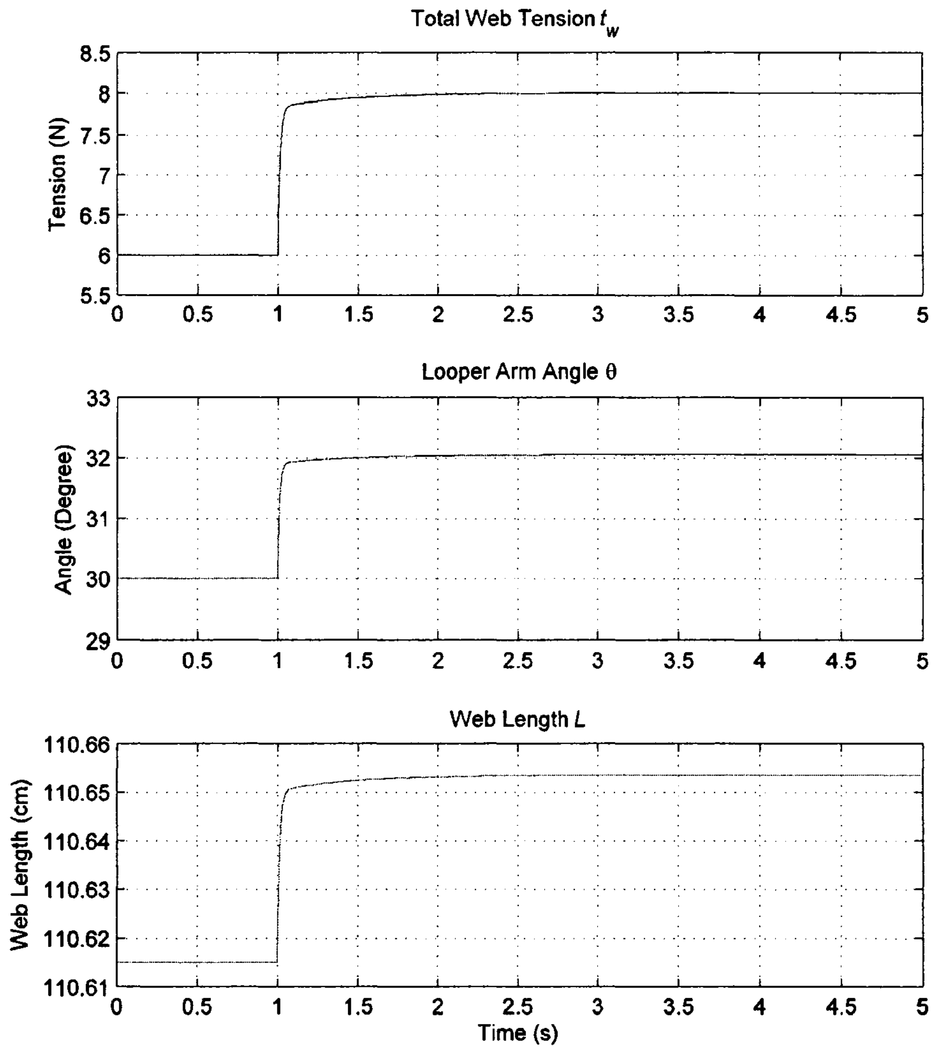

Figure 4.10 Response without disturbances.

According to equations (4.10) and (4.5), the real time web tension is also subject to two disturbances which contribute to the tension variation item T_{w2} in (4.5). One of the disturbance sources is the tension change in the upstream span, T_u; the other one is the variation in the tangential speed difference between two driven rollers, V_2-V_1. **Figure 4.11** shows these two disturbances specified for the simulation test, and **Figure 4.12** illustrates the system response to them.

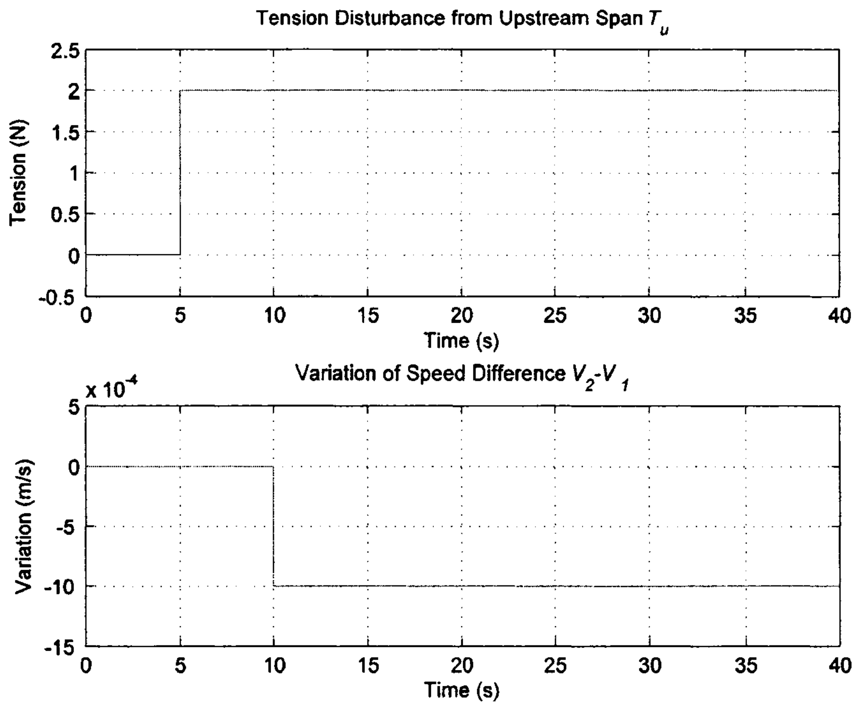

Figure 4.11 Disturbances.

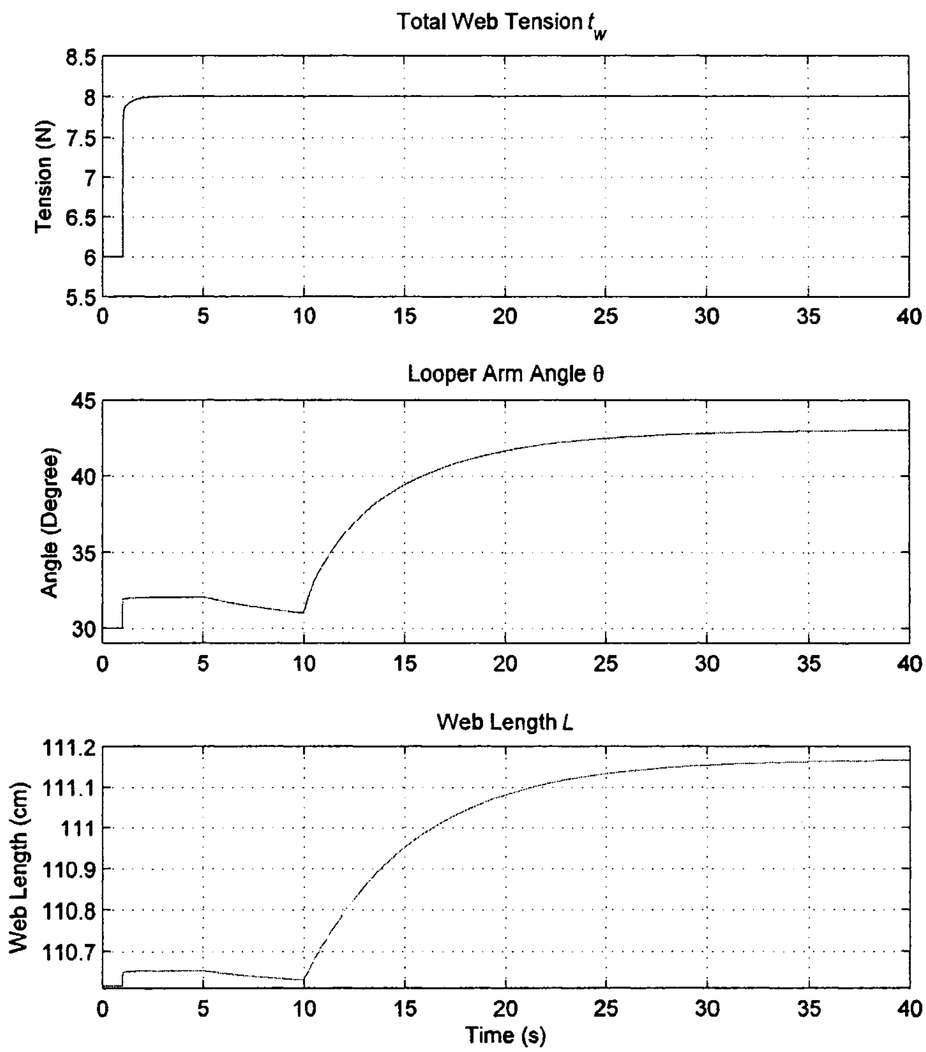

Figure 4.12 Response with disturbances.

The above figures demonstrate that the proposed looper-like actuator can effectively attenuate the tension fluctuations due to tension and speed disturbances. The angle of looper arm takes long to reach a steady state due to the integral effect between the disturbances and tension variation T_{w2}.

4.4 PID Control and Experimental Test

4.4.1 Experimental Setup

A winding process, instead of the previously discussed intermediate web span is used here for the experimental demonstration. One of the advantages of using a winding process is that tension variation can be easily simulated such that the effect of the proposed inactive tension control can be demonstrated.

For an intermediate web span, if the tangential speed difference between two driven rollers is controlled to be zero and the upstream tension disturbance is also zero, the tension change will be zero, according to equation (4.1).

However, the situation will be different for a winding process. Consider again the tension equation (3.1) in a winding process model

$$L\dot{t}_w = -v_w t_w + v_u t_{wo} + aE(v_w - v_u). \tag{4.19}$$

Although the wound-out tension of a web roll t_{wo} is usually small compared to the operating tension value and neglected in most winding process control applications, it is taken into consideration here. Taking Laplace transform for both sides of (4.19), we get

$$t_w(s) = \frac{t_{wo}v_u(s) + aE\left[v_w(s) - v_u(s)\right] + t_w(0)}{Ls + v_w(s)}. \tag{4.20}$$

where $t_w(0)$ denotes the initial state of web tension t_w.

When speed difference $(v_w - v_u)$ is controlled to be zero, equation (4.20) becomes

$$t_w(s) = \frac{t_{wo}v_u(s) + t_w(0)}{Ls + v_w(s)}. \tag{4.21}$$

Assume that the web line speed is also well controlled, i.e. v_w and v_u are equal constants. The time domain tension expression can be derived by taking inverse Laplace transform to (4.21). It yields

$$t_w(t) = \frac{t_{wo}v_u + t_w(0)}{L} e^{-\frac{v_w}{L}t} \tag{4.22}$$

The equation (4.22) means that although a winding process is controlled in terms of its line speed and tangential speed difference between winding and unwinding rolls, the web tension will exponentially drop down during the process. This effect can be equivalently regarded as a speed difference disturbance applied to an intermediate web span, as illustrated in the simulation test. The control effect of inactive actuator can then be easily observed.

Figure 4.13 shows the experimental setup used to test the proposed inactive control strategy.

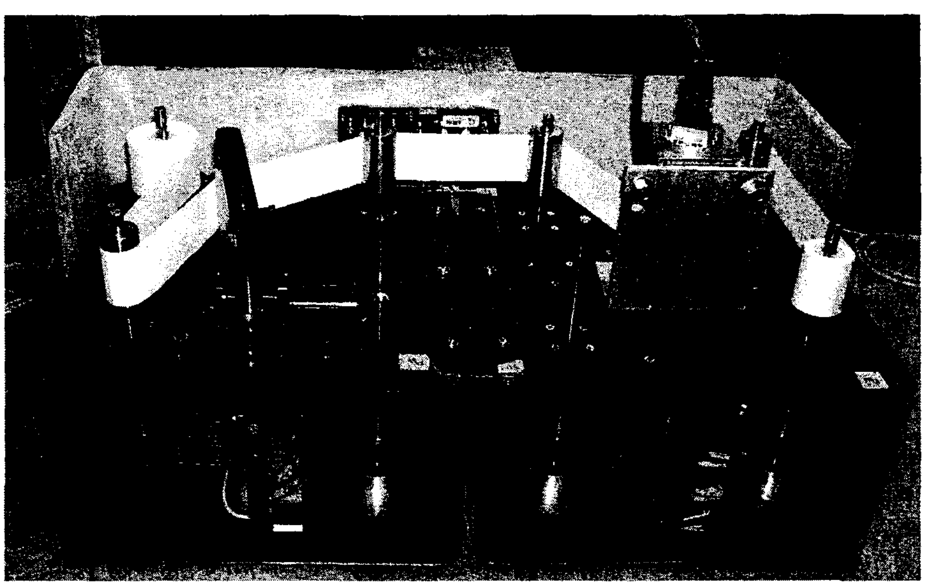

Figure 4.13 The experimental setup for inactive control.

4.4.2 Experimental Test

The control performance is first illustrated by **Figure 4.14**, which shows a time span during a winding process. As we discussed above, tension drops down continuously before the looper actuator starts to control at around the 9th second. The tension decrease with time is eliminated and the desired tension level (8*N*) is maintained by the PID controlled actuator. Changes to the looper arm angle are continuously made to compensate the tension loss.

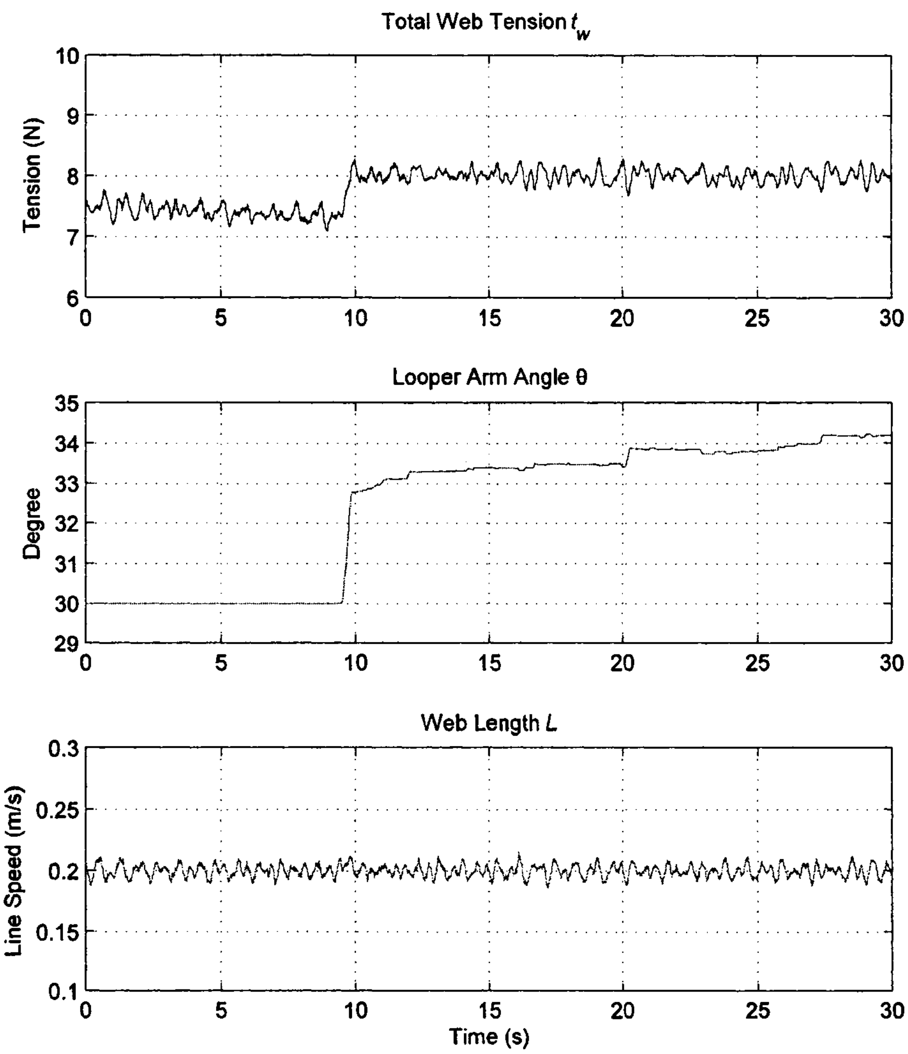

Figure 4.14 The effect of looper tension control.

Figure 4.15 shows the step response of the inactively controlled system when the web is moving in a line speed of 0.1m/s.

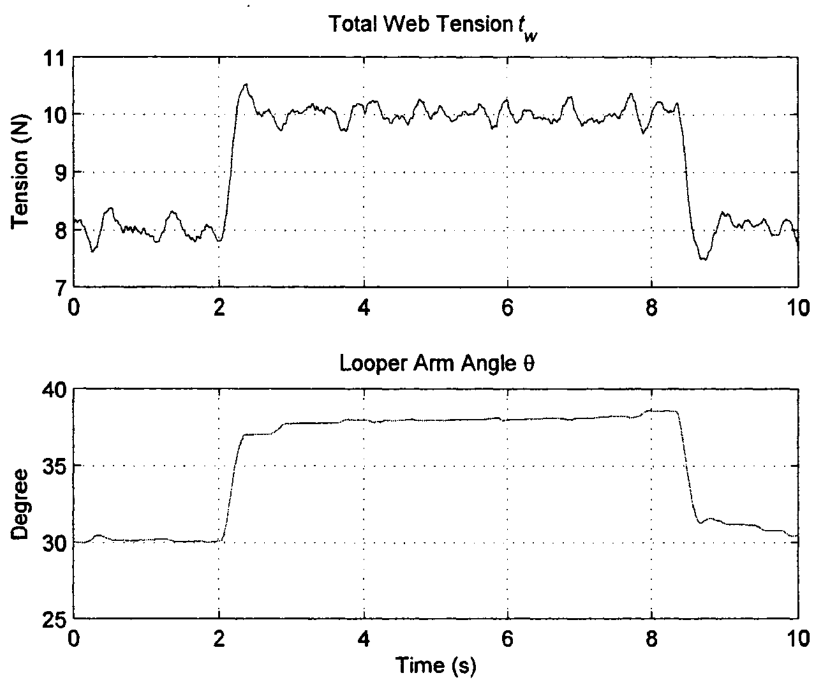

Figure 4.15 Step response in an operating state.

It can be observed that compared to the performance of robust tension control in Chapter 2, the tension fluctuation is larger when the web system is controlled by the inactive tension control actuator. One of the reasons could be demonstrated by **Figure 4.11** and **Figure 4.12.** Even a slight variation in tangential speed difference will cause a considerable tension change, because the value of Young's modulus E in tension equation (4.1) and (4.19) is very large. However, accurate speed difference control is subject to many factors, such as the eccentricity of idler rolls, which were not precisely fabricated. Another reason could be the response time of the structure. It could not be as fast as an actively controlled DC motor due to the adopted gear transmission. The speed variations can not be quickly compensated by the control motion of the actuator. This problem could be part of the future work.

4.5 Conclusion

An inactive tension control strategy is proposed to effectively eliminate 'tension transfer' phenomenon in a multi-stage web handling system. A looper-like structure is fabricated and controlled by a PID controller to implement the proposed control strategy. This is the first application in literature of looper actuator in thin web tension control. Simulation and experimental tests demonstrated the effect of the proposed inactive tension control. With the designed inactive actuator, tension control is no longer performed by controlling web driving motors and is separated from line speed control, so tension variation within a single web span will not be propagated to following spans.

Chapter 5 Summary and Future Work

This thesis concerned itself with tension and speed control strategies for a multi-stage web handling system. Both intermediate web span control and winding process control were investigated according to the functionality of considered web sections; both active strategy and inactive strategy were developed based on different actuating modes of tension control. A robust H_∞ controller was proposed for active intermediate span control and winding process control. To implement inactive tension control, a looper-like structure was designed and fabricated to adjust the tension level within a web span.

Control performance tests (simulation and experiment) and numerical robustness property analysis were combined to fulfill the evaluation of developed controllers.

5.1 Summary of the Main Results

Centralized MIMO control design, represented by H_∞ and LQR control in this thesis, is more insensitive to the coupling effect between web tension and speed than decentralized PID web system control. Web tension is more robust to the fluctuations in web transportation speed when the system is controlled by H_∞ or LQR controller. Although a feedforward loop can improve the transient performance in tension control, theoretically, it is difficult to achieve in real implementations because of the noisy tension measurement signal.

Web tension control system is unavoidably subject to external disturbances, parameter variation and plant uncertainty. Robustness property of the closed-loop system is thus a concern in developing a control strategy. Comprehensive robustness analysis was adopted as an evaluation tool in this thesis. Of the two robustness analysis methods, singular value test is proved to be more conservative than μ-analysis especially for roust stability analysis, when structured model uncertainties are considered.

The proposed robust H_∞ controller for intermediate web span control applications demonstrates its superiority to the other two controllers: LQR and decentralized PI, through robustness analysis, simulation test and experimental test. The H_∞ controller also presents a better rejection to disturbance and noise. However, one disadvantage of an MIMO control strategy is that high order transfer functions are usually involved such that higher computation capability is required for the hardware system. Furthermore, the performance of H_∞ or LQR control is also subject to the selection of weighting functions or matrices.

The variations of different parameters have different impacts on the closed-loop system's robustness property. For a web system, the web length, cross-sectional area, and Young's modulus are found in this thesis to carry the most significant influence on robust stability of the closed-loop system. This result provides a valuable reference for the robust stability acquisition in a multistage web system.

The three control strategies, H_∞, LQR and PI, were also applied to a winding process study. Again, H_∞ and LQR were verified to be superior to the decentralized PI control in terms of interaction attenuation between web tension and line speed. H_∞ control is slightly better than LQR, considering only control performance.

Robustness tests show that no controller achieves robust stability over the whole winding process, even though the radius of web roll is as small as the one in this work (31.75*cm*). The operating point at which the winding and unwinding rolls are both dimensionally half loaded is adopted for nominal controllers design. Due to the time varying parameters, the transient performance of tension control deteriorates when the system is operating away from the nominal controller design point. Therefore, certain gain scheduling scheme is required in order to maintain a steady performance over the operating range.

A dc gain analysis-based study provides a simple but efficient gain scheduling technique to deal with the time varying parameters. Verified by both simulation and experimental tests, the gain scheduling scheme improves the robustness of tension output to line speed variations at operating stages out of the control design region, such as the starting stage and end stage.

Tension transfer is a distinct phenomenon with a multi-stage web system. Active tension control systems cannot prevent tension fluctuation within a certain web span being propagated to the following web spans. Another concern in applying an active tension control is that it is usually not suitable to be integrated with an existing control system. An inactive tension control strategy is thus proposed in this work to tackle these two problems. A looper-like structure is designed and fabricated to implement the proposed control strategy. The actuator is driven by a DC motor and controlled by a PID controller. Simulation and experimental tests demonstrated the effect and validity of the proposed inactive tension control. With the designed inactive actuator, tension control is no longer performed by controlling web driving motors and is separated from line speed control, so tension variation within a single web span will not be propagated to following spans.

5.2 Open Problems and Future Work

As a mode-based control strategy, the performance of the proposed robust H_∞ controller is significantly affected by the accuracy of the adopted mathematical model. A recursive least square estimation was used for plant identification in this work. Model identification could be refined to have the model parameters closer to the ones of the real plant by using a more advanced control strategy for data generation.

A robust controller designed through μ synthesis can be developed as a comparison with the H_∞ controller in future. The control synthesis will be programmed in Matlab based on a solution by *D-K* iterations. Considering the order of μ control is high, certain order reduction technique should be adopted in order to implement the controller in an experimental setup.

More sophisticated adaptive control strategies can be investigated in future to deal with the time varying parameters in a winding process control. Online self-tuning strategies, such as neuro-fuzzy control, would be a more suitable solution than model-based adaptive techniques, considering the model approximation by linearization.

The testing apparatus could be used to test more complicated web system control, such as a two-span system for a more complicated MIMO control strategy, if more supplementary components are fabricated. The fabricated looper actuator for inactive tension control can also be refined to improve the control performance. Some advanced control strategies need to be developed for inactive tension control except the PID controller adopted in this thesis work.

References

[1]. D.P. Cambell, Process Dynamics. Wiley, 1958.

[2]. W. Wang, F. Golnaraghi, and F. Ismail. Condition monitoring of a multistage printing press. Journal of Sound and Vibration 2004; 270(5-6):755-766.

[3]. K.H. Shin. Tension Control. TAPPI Press; 2000.

[4]. S.H. Song and S.K. Sul. A new tension controller for continuous strip processing line. IEEE Transactions on Industry Applications 2000; 36(2):633-639.

[5]. C.L. Chen, K.M. Chang, and C.M. Chen. Modeling and control of a web-fed machine. Applied Mathematical Modeling 2004; 28(10):863-876.

[6]. M.F. Yeung, A.H. Falkner, and S. Gergely. The control of tension in textile filament winding. Mechatronics 1995; 5(2-3):117-131.

[7]. Tetsuzo Sakamoto and Yasunobu Izumihara. Decentralized control strategies for web tension control system. IEEE Industrial Electronics, ISIE'97. Proceedings of the IEEE International Symposium; Vol. 1.3: 1086 - 1089.

[8]. H. Koc, D. Knittel, M. de Mathelin, and G. Abba. Modeling and robust control of winding systems for elastic webs. IEEE Transactions on Control Systems Technology 2002; 10(2):197-208.

[9]. K. Park, H. Kim, and J.H. Hwang. Design of an adaptive tension/velocity controller for winding processes. IEEE Industrial Electronics, ISIE'2001. Proceedings of the IEEE International Symposium; Vol.1: 67 - 72.

[10]. Chintae Choi and Tsu-Chin Tsao. Control of linear motor machine tool feed drives for end milling: Robust MIMO approach. Mechatronics 2005; 15(10):1207-1224.

[11]. M.D. Baumgart and L.Y. Pao. Robust control of nonlinear tape transport systems with and without tension sensors. Journal of Dynamic Systems, Measurement and Control 2007; 129(1):41-55.

[12]. D. Knittel, E. Laroche, D. Gigan, and H. Koc. Tension control for winding systems with two-degrees-of-freedom H-infinity controllers. IEEE Transactions on Industry Applications 2003; 39(1):113-120.

[13]. S. Boyd and C. Barrantt. Linear controller design. New York: Prentice Hall; 1991.

[14]. E. Laroche and D. Knittel. An improved linear fractional model for robustness analysis of a winding system. Control Engineering Practice 2005; 13(5):659-666.

[15]. J.C. Doyle, A. Packard and K. Zhou. Review of LFTs, LMIs and Mu. In: Proceedings of the 30th Conference on Decision and Control, Brighton, England, 1991; p. 1227-1232.

[16]. K. Zhou and J.C. Doyle. Essentials of Robust Control. Prentice Hall; 1998.

[17]. R.W. Beaven, M.T. Wright, and D.R. Seaward. Weighting function selection in the design process. Control Engineering Practice 1996; 4(5):625-633.

[18]. J. Hu, Ch. Bohn, and H.R. Wu. Systematic H_∞ weighting function selection and its application to the real time control of a vertical take-off aircraft. Control Engineering Practice 2000; 8(2000), 241-252.

[19]. J.C. Doyle, K. Glover, P.P. Khargonekar, and B.A. Francis. State-Space solutions to standard H-2 and H-infinity control problems. IEEE Transactions on Automatic Control 1989; 34(8):831-847.

[20]. K. Glover and J.C. Doyle. State-space formulae for all stabilizing controllers that satisfy an H_∞-norm bound and relations to risk sensitivity. Systems & Control Letters 11 (1988); 167-172.

[21]. M.G. Safonov, D.J.N. Limebeer, and R.Y. Chiang. Simplifying the H-infinity theory via loop shifting, matrix pencil and descriptor concepts. Int. J. Control 1989; 50(6):2467–2488.

[22]. K.J. Astrom and B. Wittenmark. Adaptive Control. Addison-Wesley Longman, Boston, 1994.

[23]. P. Mathur, D. Priyadarshee and W.C. Messner. Controller development for a prototype high-speed low-tension tape transport. IEEE Transactions on Control Systems Technology 1998; 6(4), 534-542.

[24]. K.C. Lin. Observer-based tension feedback control with friction and inertia compensation. IEEE Transactions on Control Systems Technology 2003; 11(1), 109-118.

[25]. S. Toffner-Clausen. System identification and robust control. Springer; 1996.

[26]. Y. Cheng and L.R. de Moor. Robustness analysis and control system design for a hydraulic servo system. IEEE Transactions on Control Systems Technology 1994; 2(3), 183-197.

[27]. R.V. Dwivedula, Y. Zhu, and P.R. Pagilla, Characteristics of active and passive dancers: A comparative study, Control Engineering Practice 2006; 14, 409–423.

[28]. P.R. Pagilla, R.V. Dwivedula, Y. Zhu, and L.P. Perera, Periodic Tension Disturbance Attenuation in Web Process Lines Using Active Dancers, Journal of Dynamic Systems, Measurement, and Control 2003; 125, 361-371.

[29]. N.A. Ebler, R. Arnason, G. Michaelis, and N. D'Sa, Tension Control: Dancer Rolls or Load Cells, IEEE Transactions on Industry Applications 1993; 29(4), 727-739.

[30]. T. Hesketh, Y.A. Jiang, D.J. Clements, D.H. Butler, and R.V. der Laan, Controller Design for Hot Strip Finishing Mills, IEEE Transactions on Control Systems Technology 1998; 6(2), 208-219.

[31]. I.S. Choi, J.A. Rossiter, and P.J. Fleming. Looper and tension control in hot rolling mills: A survey. Journal of Process Control 2007; 17(6):509-521.

[32]. X. Liu. Linear Control Theory. Lecture notes, Lakehead University 2006.